Density Structure of Globules (Isolated Dense Cores) and Its Implications for Star Formation

Ryo KANDORI

Doctor of Science

Department of Astronomical Science,
School of Physical Science,
The Graduate University for Advanced Studies

2004

Acknowledgment

I would like to express my gratitude to my supervisor, Ken'ichi Tatematsu. I am grateful for his thoughtful guidance and encouragement in the progress of my study. He has spent a great amount of time working with me and has helped me to improve the contents of this dessertion. I also appreciated Motohide Tamura, who gave me invaluable advice on the infrared astronomy and guided my study to the right direction.

Thanks are due to Yasushi Nakajima in NAOJ and Takahiro Naoi in the University of Tokyo for their instructions on the near-infrared observations, data reductions, and publications. I am indebted to Masao Saito in NAOJ, who instructed me in the radio astronomy and gave me kind suggestions in various aspects. My gratitude is also to Yuri Aikawa and Koji Tomisaka for their stimulating suggestions from the theoretical point of view. Helpful discussion with Koji Sugitani in Nagoya City University, Tetsuya Nagata in Kyoto University, and Shuji Sato in Nagoya University are greatly acknowledged. I am obliged to the staff at the South African Astronomical Observatory, Nobeyama Radio Observatory, and Kiso Observatory for their kind support during the observations for this study. I am very grateful to all the people in ALMA-Japan Project Office, in particular Tetsuo Hasegawa, Ryohei Kawabe, Sachiko Okumura, Masao Saito, Satoru Iguchi, Tomohiko Sekiguchi, Nobuyuki Yamaguchi, Takahiro Hayakawa, and Masahiro Sugimoto, for their continuing encouragements.

This work is mainly based on data obtained using the IRSF 1.4 m telescope and the SIRIUS camera. The IRSF/SIRIUS project was initiated and supported by Nagoya University, National Astronomical Observatory of Japan, and University of Tokyo in collaboration with South African Astronomical Observatory under a financial support of Grant-in-Aid for Scientific Research on Priority Area (A) No. 10147207 and No. 10147214, and Grant-in-Aid No. 133573001 of the Ministry of Education, Culture, Sports, Science, and Technology of Japan.

Abstract

Stars are thought to be formed in dense molecular cloud cores. It, however, still remains unclear how and when the star formation process takes place. In order to understand the (low-mass) star formation process, I have studied the density structure, stability, and evolution of globules (isolated dense cores) on the basis of dust extinction measurements. Dust extinction measured at near-infrared wavelengths provides a robust measure of the column density. On the basis of near-infrared imaging observations, I derived extinction distributions toward ten globules, and investigeted their radial density structure by using the Bonnor-Ebert sphere model. The Bonnor-Ebert model describes a pressure-confined self-gravitating isothermal gas sphere in hydrostatic equilibrium. Using the data of my ten globules and four globules in the literature (three star-forming and eleven starless globules), I investigated the stability of globules on the basis of $\xi_{\rm max}$, which characterizes the Bonnor-Ebert sphere as well as the stability of the equilibrium state against the gravitational collapse. I found that more than half of the starless globules are located near the critical state of the Bonnor-Ebert sphere ($\xi_{\rm max} = 6.5 \pm 2$). Thus, I suggest that a nearly critical Bonnor-Ebert sphere characterizes the typical density structure of starless globules, and it approximates the initial condition of gratitational collapse. Remaining starless globules show clearly unstable states ($\xi_{\rm max} \gg 6.5$). Since unstable equilibrium states are not long sustainable, I expect that these globules are on the way to gravitational collapse or that they are stabilized by non-thermal support. It was also found that all the star-forming globules show unstable solutions of $\xi_{\rm max} > 10$, which is consistent with the fact that they have started gravitational collapse. I investigated the evolution of a collapsing gas sphere whose initial condition is a nearly critical Bonnor-Ebert sphere. I found that the column density profiles of the collapsing sphere mimic those of the static Bonnor-Ebert spheres in unstable equilibrium. Since the evolutionary timescale increases with decreasing density, the collapsing gas sphere resembles marginally unstable Bonnor-Ebert spheres for a long time. I found that the frequency distribution of $\xi_{\rm max}$ for the observed starless

globules is consistent with that from model calculations of the collapsing sphere. In addition to the near-infrared observations, I carried out radio molecular line observations ($C^{18}O$ and N_2H^+) toward the same ten globules. I confirmed that most of the globules are dominated by thermal support. The line width of each globule was used to estimate the cloud temperature including the contribution from turbulence, with which I estimated the distance to the globules from the Bonnor-Ebert model fitting.

Contents

1 Introduction **9**

1.1 Historical Overview 9

1.2 Physical Properties of Young Stellar Objects (YSOs) 11

1.3 Initial Conditions of Isolated Star Formation 12

1.3.1 Lifetime of Dense Cores 13

1.3.2 Density Structure of Dense Cores 13

1.3.3 Velocity Structure of Dense Cores 16

1.4 Thesis Work 18

2 Near Infrared Imaging Survey of Bok Globules: Density Structure **27**

2.1 Introduction 28

2.2 Observations and Data Reduction 30

2.2.1 Source Selection 30

2.2.2 Near-Infrared Data 32

2.2.3 Molecular Line Data 34

2.3 Derivation of A_V and Molecular Line Parameters 35

2.3.1 Star Count 35

2.3.2 Near-Infrared Color Excess 37

2.3.3 Molecular Line Parameters 37

2.4 Density Structure 38

2.4.1 Bonnor-Ebert Sphere Model 38
2.4.2 Bonnor-Ebert Model Fitting of Bok Globules 40
2.5 Discussion: Stability and Evolution of Globules 43
2.5.1 Physical Properties of Globules 43
2.5.2 On the Selection Bias of the Globule Samples 46
2.5.3 Implications for the Stability of Globules 46
2.5.4 Slow Collapse of A Nearly Critical Bonnor-Ebert Sphere 49
2.6 Summary 51

3 Grain Growth in the Dark Cloud L1251 **73**
3.1 Introduction 74
3.2 Observations and Data Reduction 75
3.3 Distribution of Extinction 77
3.4 Distribution of Color Excess 79
3.5 Derivation of R_V Distribution and Evidence for Grain Growth 81
3.6 Summary 84

4 Conclusion **93**

A Development of Software for the Virtual Observatory Prototype in ALMA-Japan **97**
A.1 Introduction 97
A.2 Science Requirements 99
A.3 Science Cases 99
A.4 ALMA-Japan VO Prototype System 100
A.4.1 Overview of the System Design 100
A.4.2 Query and User Interface 101
A.4.3 Radio Data Pipeline 101

A.4.4 Near-infrared Data Pipeline 102
A.4.5 Data Analysis Tools 102
A.5 Summary 103

Chapter 1

Introduction

1.1 Historical Overview

Stars are the most fundamental component of the universe, and are thought to be formed in the interstellar molecular clouds. In the past decades, observations at radio and infrared wavelengths revealed that cold and dense condensations within molecular clouds are closely related to the formation of stars. These condensations, "dense molecular cloud core", eventually form stars through gravitational collapse. Fruitful information on the origin of stars can be obtained from the information about physical evolution of dense cores including the onset of gravitational collapse. It, however, still remains unclear what is the initial condition for the gravitational collapse, when the collapse takes place, and how the collapse proceeds. This is mainly due to observational difficulties to probe physical properties of dense cores, because they are highly opaque objects, in particular at optical wavelengths. To understand the star formation process, it is crutial to probe internal structure of dense cores, their stability against self-gravity, and their evolution toward star formation.

Historically, molecular clouds and dense cores were firstly recognized as "dark markings", which absorb the light from background stars, on the optical photographic plates (Barnard 1919). Molecular clouds consist of molecular gas (99 % in mass) and dust (1 % in mass).

The dust significantly contributes to absorption and scattering of star light. Thus, molecular clouds in the solar neighborhood can be seen as "dark clouds" against background stellar fields. By using extinction, general catalogs of dark clouds have been made by, for example, Barnard (1927), Lynds (1962), Feitzinger & Stuwe (1984), and Clemens & Barvainis (1988). Bok & Reilly (1947) firstly drew attention to small, round, dense dark clouds, and suggested a possibility of star formation there. They proposed to call such condensations "globules". An isolated geometry from neighboring clouds is another important characteric of globules. Physical properties of globules, such as size, mass, and density, are similar to those of dense molecular cloud cores, suggesting that globules are the isolated counterpart of dense cores. Since the strength of dust extinction toward dark clouds is directly proportional to the total amount of dust along the line of sight, extinction maps of dark clouds and/or globules provide important imformation on their size, morphology, mass, and density (e.g., Dickman 1978).

After the discoveries of molecular lines from dark clouds in a few decades from the 1960's (e.g., OH line: Weinreb et al. 1963), "molecular clouds" became alternative term to describe dark clouds. Since the main component of molecular gas, molecular hydrogen H_2, is not directly observable under the physical condition in molecular clouds, the next most abundant molecule, CO, and the other less abundant molecules, such as CS, NH_3, plays important roles in tracing molecular gas distributions and in probing the kinematics and chemical composition of molecular clouds. In the past a few decades, extensive survey of molecular clouds and/or dense cores by using radio telescopes have been carried out by, for instance, Scoville & Solomon (1975), Blitz (1980), Dame et al. (1987), and Benson & Myers (1989). Physical properties of molecular clouds, e.g., density, mass, and size, have large dynamic ranges as summarized in Table 1.1 (adapted from Cernicharo 1991 and van Dishoek et al. 1993). Cold, dark molecular clouds and giant molecular clouds (GMCs) are important objects to study star formation process. It is known that hierarchical structure is commonly observed in molecular cloud complexes; for instance, CO observations of the Cygnus OB7 complex (Falgarone et al. 1992) revealed that hierarchy exists in all observable scales, from entire cloud complex (tens of parsecs) down to

0.1-pc size structure (Fig. 1.1). Molecular cloud complexes have substructure: e.g., massive (star-forming) clumps, which may form cluster of stars, and dense (pre)protostellar cores, which may form single star or multiple systems (see, e.g., Williams et al. 2000).

In recent years, it was suggested to distinguish between isolated star formation (see, e.g., Ward-Thompson 2002) and cluster star formation (see, e.g., Pudritz 2002). It is known that low-mass stars are formed in both isolated and clustered mode of star formation, while high-mass star formation occurs exclusively in cluster-forming massive clumps in GMCs. Thus, it is most likely that different physical processes dominate in isolated and clustered star forming regions. Since most of stars are thought to be formed as member of clusters in GMCs (e.g., Lada 1999), less massive molecular clouds as well as isolated dense cores (i.e., globules) do not significantly contribute to the star formation activity in the Galaxy. Small and isolated molecular clouds have been paid great attention because they are ideal sites to study physical process in star formation; their simple shape and isolated geometry from neighboring clouds enable us to model their internal structure. I review low-mass star formation process in isolated dense cores in the following sections.

1.2 Physical Properties of Young Stellar Objects (YSOs)

Low-mass star formation begins with gravitational collapse of dense cores having a density of $\sim 10^4$ cm^{-3} and a size of order 0.1 pc. The infalling material forms an embryonic star in the core, and surrounding circumstellar material accretes onto the forming star. YSO in this phase is called protostar. Stars acquire most of their final mass through accretion in this phase. Since protostars are highly obscured by dusty envelope, they are invisible at optical wavelengths for the most of this phase. Jets and molecular outflows are commonly associated with protostars. After most of surrounding material accretes onto forming stars and/or is swept away by outflows, stars become visible at optical wavelengths. YSO in this phase is called pre-main-sequence star or T Tauri star (TTS). TTSs are in the process of the quasi-

static contraction. They turn into main sequence stars at the onset of hydrogen burning at the centar.

YSOs refer to variety of objects, from the earliest main mass acccretion phase (protostar) to the more evolved pre-main-sequence phase. Various types of YSOs can be classified on the basis of their spectral enegy distributions (SED) as shown in Figure 1.2. It is popular to classify YSOs into three classes (Class I, II, III) using the slope, $\alpha = d\log\lambda F_\lambda / d\log\lambda$, of SEDs at infrared wavelengths (Lada & Wilking 1984; Adams et al. 1987; Lada 1991). Deeply embedded young protostars show positive α values ($\alpha > 0$) because strong infrared excess emission comes from their circumstellar/envelope material in addition to the photospheric blackbody emission. They are classified as Class I source. The lifetime of Class I sources is estimated to be $\sim 10^5$ yr (e.g., Wilking, Lada, & Young 1989). The value of α decreases with decreasing circumstellar material surrounding YSOs. Class II ($-1.5 < \alpha < 0$, age of $\sim 10^6$ yr) and Class III ($\alpha < -1.5$, age of $\sim 10^7$ yr) correspond to the pre-main-sequence star, in particular classical T Tauri star and weak-line T Tauri star, respectively.

André, Ward-Thompson & Barsony (1993) introduced an additional class, Class 0, which is the youngest protostar phase. Class 0 sources are characterized by (1) no detection of central stars at near to mid infrared wavelengths (< 10 μm), (2) a high ratio of the submillimeter to bolometric luminosity, (3) a SED resembling cold blackbody of less than ~ 30 K. Class 0 sources are thought to extremely young protostars in the midst of main mass accretion. The lifetime of Class 0 sources are estimated to be $\sim 10^4$ yr on the basis of the ratio of the observed number of Class 0 sources to the number of Class I sources (e.g., André & Montmerle 1994).

1.3 Initial Conditions of Isolated Star Formation

Dense cores can be divided into two groups: one is the starless dense core and another is the star-forming dense core that is associated with YSOs. The comparison study of both starless and star-forming dense cores is important to provide essential information on the evolution of

density, velocity, and chemical structure of dense cores as well as their relative lifetime.

1.3.1 Lifetime of Dense Cores

The Infrared Astronomical Satellite, IRAS, provided extensive data to identify deeply embedded YSOs, i.e., protostars, in dense molecular clouds and to investigate association of protostars with dense cores (e.g., Beichman et al. 1986). The ratio of the number of cores with protostars to the number of starless cores provides an important constraint on the lifetime of starless cores, because typical timescale of YSOs observed as embedded protostars is known ($\sim 10^5$ yr). Several observational studies suggest that the typical lifetime of starless dense core is several times of 10^5 yr (e.g., Visser et al. 2002; Lee & Myers 1999; Onishi et al. 2002), which is several times larger than the free-fall time of gas at a density of $\sim 10^4$ cm^{-3}. These studies were mostly based on the IRAS point source catalog to identify protostars. Since low-luminosity protostars may escape from detection in the IRAS catalog (see, e.g., Young et al. 2004), the estimated lifetime of starless dense cores serves as the upper limit.

1.3.2 Density Structure of Dense Cores

One of the most straightforward ways to probe density structure of dense cores is to observe dust. It is established that gas-to-dust ratio in molecular clouds is fairly uniform (e.g., Bohlin, Savage, & Drake 1978; Ryter 1996). Molecular line observations, on the other hand, are highly affected by chemical abundance and excitation conditions of molecules. It is known that molecular depletion is serious for some species, e.g., CO, CCS, and CS, in cold starless dense cores (e.g., Caselli et al. 1999; Aikawa et al. 2001), which may cause misleading interpretations of observations.

Dust Emission Observations

Important findings on density structure of dense cores were provided by observing thermal dust emission at millimeter and submillimeter wavelengths using bolometer cameras on single-dish radio telescopes. Since dust emission traces gas column density, i.e., $N(H_2)$, radial density profile of dense cores can be derived by assuming spherical symmetry in core's shape. It was found that starless dense cores show similar shapes of density profile (Ward-Thompson et al. 1994, 1999; André et al. 1996), which consist of flat inner region ($\rho \sim$ constant) steepening toward outermost region ($\rho \propto r^{-2}$). More recently, Bacmann et al. (2000) studied density structure of starless cores on the basis of dust extinction measurements at mid infrared (~ 7 μm) wavelengths using the Infrared Space Observatory (ISO). They confirmed the existence of inner flat region in starless cores, and determined the shape of density profile at outermost low-density region that cannot be revealed from ground-based submillimeter observations. They found that typical column density profile of starless cores gets steeper than $N(H_2) \propto r^{-1}$ at radii greater than 5000-10000 AU, suggesting that reservoirs of mass for the future star formation in starless cores are finite, i.e., $\rho \propto r^{-p}$ with $p > 2$ at outer region. In other words, dense cores appear to be decoupled at some specific radii from their ambient medium. Similar result, i.e., existence of steep edge, has also been reported by Tomita et al. (1979) who studied density structure in and around the optical boundary of large globules based on extinction measurements at optical wavelengths. I note that if density distributions of dense cores are truncated at specific outer radii, observed steep edge, i.e., $N(H_2) \propto r^{-p}$ with $p > 1$, in column density profiles can naturally be explained.

For star-forming dense cores, it was found that they are well fitted by the single power-law density profile ($\rho \propto r^{-p}$) with $p \sim 1.8$ (e.g., Class 0 core: Shirley et al. 2002; Class I core: Young et al. 2003). These results confirm that star-forming dense cores show the higher degree of central condensation than that for starless cores. The presence of central star/disk system and surrounding envelope, however, makes it diffucult to model density structure based on

single-dish observations. The combination of both a single-dish telescope and higher resolution observations with interferometer is needed to reveal density structure of star-forming cores from the center to the outermost region.

Recently dust temperature gradient in cold dense starless cores has been reported (e.g., Evans et al. 2001; Ward-Thompson, André, & Kirk 2002). Since the intensity of thermal dust emission is proportional to the sum of the product of dust temperature and density along the line of sight, the temperature gradient systematically affects the column density distributions which are derived by assuming a constant dust temperature. I note that extinction measurements from the mid-infrared imaging (e.g., Bacmann et al. 2000) can also be affected by dust temperature distributions, because both absorption and emission from the line-of-sight medium should be taken into account at these wavelengths.

Dust Extinction Observations

Observations of dust extinction (A_V) at optical to near-infrared wavelengths provide more reliable measure of column density than any other methods. Dust extinction is not affected by dust temperature distribution and can reliably trace column densities from the core center to low-density outer regions. There are two standard ways for extinction mapping; one is the star count method (e.g., Dickman 1978) based on the measurements of stellar density, and the other is the near-infrared color excess (NICE) method (Lada et al. 1994; Lada, Alves, & Lada 1999) based on the measurements of color excess, e.g., E_{H-K}, of background stars. Since extinction cross-section of dust grains decreases with increasing wavelengths (e.g., Cardelli et al. 1989), extinction measurements at near-infrared wavelengths can probe regions of large column density (typically $A_V < 50$ mag at H and K). At near-infrared wavelengths, the reddening/extinction law is less affected by dust properties, e.g., grain growth, than that at optical wavelengths (e.g., Cardelli et al. 1989). In other words, observations of extinction at optical wavelengths are sensitive to the change in dust optical properties (e.g., Whittet et al. 2001; Kandori et al. 2003). Such observations provide important information on dust grains itself (e.g., size and

composition).

On the basis of near-infrared observations, Alves et al. (2001) demonstrated that the Bonnor-Ebert sphere model (Bonnor 1956; Ebert 1955) fits observed radial column density profile of the dark globule Barnard 68 remarkably well (Fig. 1.3). The Bonnor-Ebert sphere is the simplest model to describe a pressure-confined self-gravitating isothermal gas sphere in hydrostatic equilibrium. The shape of the Bonnor-Ebert density profile consists of flat central region surrounded by a steeper outer region of $\rho \propto r^{-2}$, which resembles the typical density structure of starless dense cores obtained in previous (sub)millimeter dust emission observations. The best fit Bonnor-Ebert solution of Barnard 68 gives a density contrast (central-to-surface density ratio) of 16.5, which exceeds the critical value of 14 for stable equilibrium of the Bonnor-Ebert sphere. Such a condition, i.e., unstable equilibrium state, should not be long sustained, suggesting that the globule is on the way to gravitational collapse or that the globule is stabilized by other mechanisms, e.g., magnetic support and/or turbulence (see, e.g., multi-pressure polytrope model: McKee & Holliman 1999). It remains unclear which physical mechanism is actually important in Barnard 68. In order to understand initial conditions for star formation, it is crutial to know density structure of dense cores before and after the onset of gravitational collapse. Such studies require a number of dense core samples with well-determined physical properties. However, no statistical studies of density structure of dense cores based on near-infrared extinction measurements has been carried out.

1.3.3 Velocity Structure of Dense Cores

Molecular line observations provide important information on the gas motion in dense cores. The existence of non-thermal turbulence in molecular clouds is well known (e.g., Mac Low & Klessen 2004). The observed linewidths are in general larger than those expected from gas kinetic temperatures (typically $\sim$ 10 K); the origin of the excess in linewidths is attributed to the non-thermal turbulent motion of gas in molecular clouds. Thus, in addition to the

thermal pressure, turbulence is considered to contribute to the support of dense cores against self-gravity. It is well known that a correlation exists between observed linewidths and the size (and mass) of molecular clouds (linewidth-size relation: Larson 1981). The relationship that linewidth increases with increasing cloud size in a power-law fashion, holds even in dense cores (e.g., Fuller & Myers 1992). For dense cores in low-mass star forming regions, which are the smallest end of hierarchy of molecular cloud structure, the observed linewidths become close to the thermal line width (e.g., Myers 1983; Hotzel et al. 2002a; Tatematsu et al. 2004); the turbulent pressure appears to be smaller than or comparable to the thermal pressure in dense cores. The observations of velocity gradient in dense cores provide measure of rotational enegy, which can also contribute to the support of cores against self-gravity. Goodman et al. (1993) presented that the ratio of rotational to gravitational energy, β, is the order of 10^{-2}, suggesting that the rotation of dense cores is not important with respect to the support of cores. The result is confirmed by recent observations (e.g., Caselli et al. 2002).

One of the most important outcomes from molecular line observations is the kinematic evidence of infall gas motion in gravitationally collapsing clouds (see, e.g., Evans 1999). A schematic illustration in Figure 1.4 shows how the infalling gas motion in dense cores forms an asymmetric profile in optically thick line emission (e.g., CS $J = 2 \rightarrow 1$ line). A double-peaked asymmetric profile with a stronger blue-shifted portion (blue-skewed profile) provides evidence of infall motion. This asymmetry originates from an inward gas motion and an inwardly increasing excitation temperature, $T_{\rm ex}$, of molecular lines with high critical density; red-shifted emissions from higher $T_{\rm ex}$ regions can be absorbed by the lower $T_{\rm ex}$ gas, which makes the red-shifted peak weaker than the blue-shifted peak. Infall asymmetry line profiles were observed toward some Class 0 protostars (e.g., Walker et al. 1986; Zhou et al. 1993); recent observations of the IRAS 04191+1522 revealed detailed velocity structure of the envelope gas around the Class 0 source (Belloche et al. 2002).

Extensive surveys of infall asymmetry profile in starless dense cores have been carried out (Lee et al. 1999, 2001, 2003). Subsonic infall motions, typically around 0.05 km s^{-1}, were

detected in some infall candidate cores, which are $\sim 10-20$ % of the total number of observed starless dense cores. This result suggests that the gravitational collapse of dense cores begins before the formation of enbryonic central star. In their surveys, it was also found that infall asymmetry profiles widely distributed over core radii of $\sim$ 0.1 pc, which is too extended to be explained by the standard "inside-out" collapse scenario (Shu 1977). Though "run-away" dynamical collapse scenario (Larson 1969; Penston 1969) provides extended infall velocity distribution, the assumed initial density condition for collapse in the model, uniform density sphere, is inconsistent with typical density structure of starless dense cores, i.e., the Bonnor-Ebert like profile. It should be fruitful to investigate the gravitational collapse of a gas sphere whose initial density condition is close to the Bonnor-Ebert sphere (e.g., Foster & Chevalier 1993; Ogino, Tomisaka, & Nakamura 1999). If the initial condition is set to the nearly critical Bonnor-Ebert sphere with central density of $\sim 10^4$ cm^{-3} and temperature of 10 K (Aikawa et al. 2004), the time scale of the collapse is several times the free-fall time, which is comparable with the lifetime of starless dense cores derived from observations (e.g., Visser et al. 2002; Lee & Myers 1999; Onishi et al. 2002). The expected inward gas velocity remains subsonic (< 0.1 km s^{-1}) for the most of total collapse time, which is consistent with observed infall velocities in dense starless cores (e.g., Lee et al. 1999, 2001, 2003). Thus, the collapse of the Bonnor-Ebert sphere may provide a successful scenario to describe the process of gravitational collapse in dense cores.

1.4 Thesis Work

In my thesis, I mainly fucus on the density structure, stabitily, and evolution of globules (isolated dense cores) in order to understand low-mass star formation process (Chapter 2). On the basis of extinction (A_V) measurements of both starless and star-forming globules at the near-infrared wavelengths, I investigated density structure and stability of ten globules using the Bonnor-Ebert sphere model. I studied the evolution of the density structure of

starless globules by comparing observations with the theoretical calculation of a collapsing gas sphere whose initical condition is close to the Bonnor-Ebert sphere. In addition to the near-infrared observations, I carried out radio molecular line observations toward the globules to investigate the degree of turbulent motion in each object. The Bonnor-Ebert model fitting studies of globules based on near-infrared imaging observations have been reported for four sources: Barnard 68 (Alves et al. 2001), Barnard 335 (Harvey et al. 2001), Coalsack Globule II (Lada et al. 2004; Racca et al. 2001), and Lynds 694-2 (Harvey et al. 2003). With the limited number of globules with well-defined physical properties, statistical studies were impossible. By using the data of my ten globules and four globules in the literature, I have performed the first systematic study of the density structure of globules based on the near-infrared extinction measurements.

The reddening/extinction law is my particular interest, because dust optical properties are closely related to the size and composition of dust grains (e.g., Mathis, Rumpl, & Nodesieck 1977). I studied dust optical properties in the dark cloud Lynds 1251 based on optical imaging observations at multiple wavelengths, B, V, R, and I (Chapter 3). In addition to the extinction mapping of the cloud, I derived distributions of the ratio of total to selective extinction, $R_V = A_V/E_{B-V}$, in Lynds 1251 for the first time. The value of R_V is a measure of wavelentgh dependence of the interstellar extinction, representing the shape of the reddening/extinction curve (e.g., Cardelli et al. 1989). I investigated how much R_V can vary in a single dark cloud by comparing observations with the well established value of $R_V \sim 3.1$ for the diffuse interstellar medium (e.g., Whittet 1992). This is the first study to create R_V map of a dark cloud on the basis of the average color excess measurements, i.e., E_{B-V}, E_{V-R}, and E_{V-I} at multiple optical bands.

In Appendix A, I introduce the development of a virtual observatory (VO) prototype in the Japanese group of the Atacama Large Millimeter/submillimeter Array (ALMA-Japan). The VO prototype system consists of two data pipelines that can reduce raw observational data taken by the near-infrared and radio telescopes. I developed a near-infrared data reduction

pipeline, and implemented it into the VO system. The pipeline has additional functionarities to perform data analysis, stellar detection/photometry and extinction mapping of dark clouds, which enable us to reduce and analyze huge amount of near-infrared data automatically.

Table 1.1 Physical properties of interstellar molecular clouds

	Giant Molecular Cloud Complex	Molecular Cloud / Dark Cloud Complex	Star-Forming Clump	Dense Core (Pre/Protostellar)
Size (pc)	$10 - 60$	$2 - 20$	$0.1 - 2$	$\lesssim 0.1$
Density $[n(H_2)\ cm^{-3}]$	$100 - 500$	$10^2 - 10^4$	$10^3 - 10^5$	$> 10^5$
Mass $(M_\odot)$	$10^4 - 10^6$	$10^2 - 10^4$	$10 - 10^3$	$0.1 - 10$
Linewidth $(km\ s^{-1})$	$5 - 15$	$1 - 10$	$0.3 - 3$	$0.1 - 0.7$
Temperature (k)	$15 - 20$	$10 - 30$	$10 - 30$	$7 - 15$

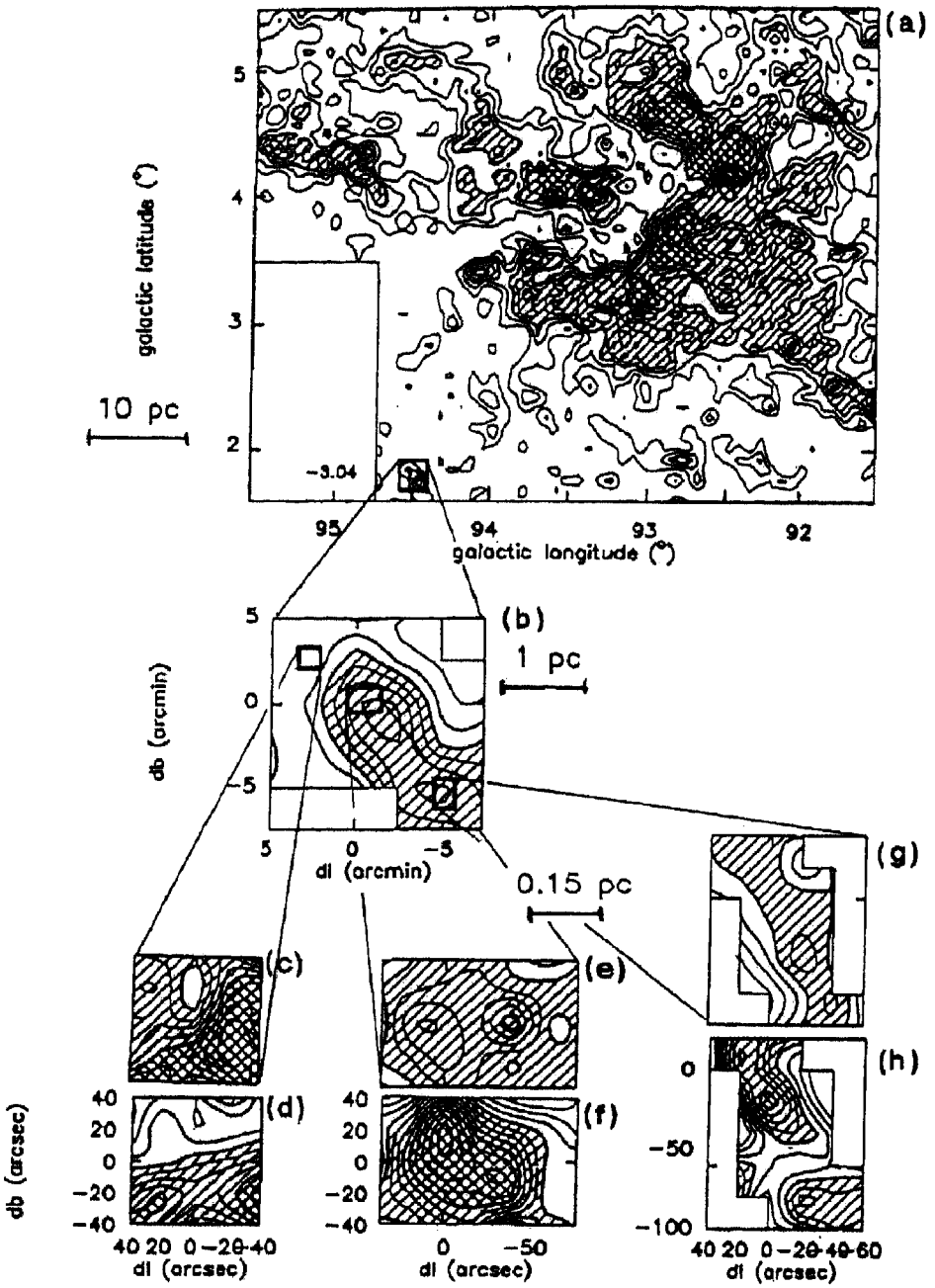

Figure 1.1 Maps of molecular gas distributions in the Cygnus OB7 complex (Falgarone et al. 1992). (a) Large scale map based on the ^{13}CO $J = 1 \rightarrow 0$ observations. (b) Map of a subregion with higher angular resolution using the same line. (c) ^{12}CO $J = 1 \rightarrow 0$, (d), (e), and (g) are based on the ^{13}CO $J = 1 \rightarrow 0$ observations. (f) and (h) are based on the ^{18}CO $J = 1 \rightarrow 0$ observations.

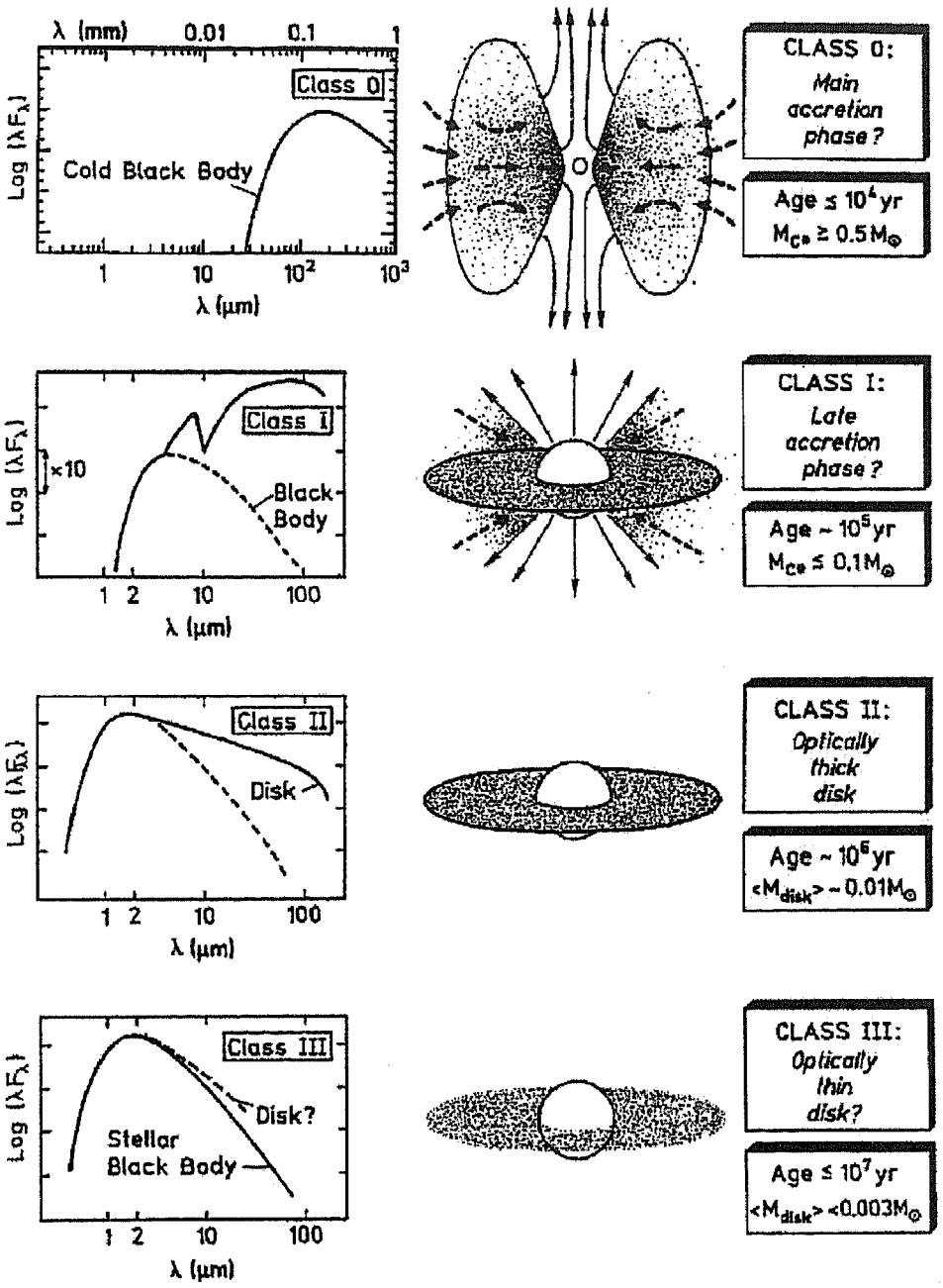

Figure 1.2 A schematic illustration of the classification of YSOs in different evolutionary stages based on the shape of SEDs (figure taken from Bachiller 1996).

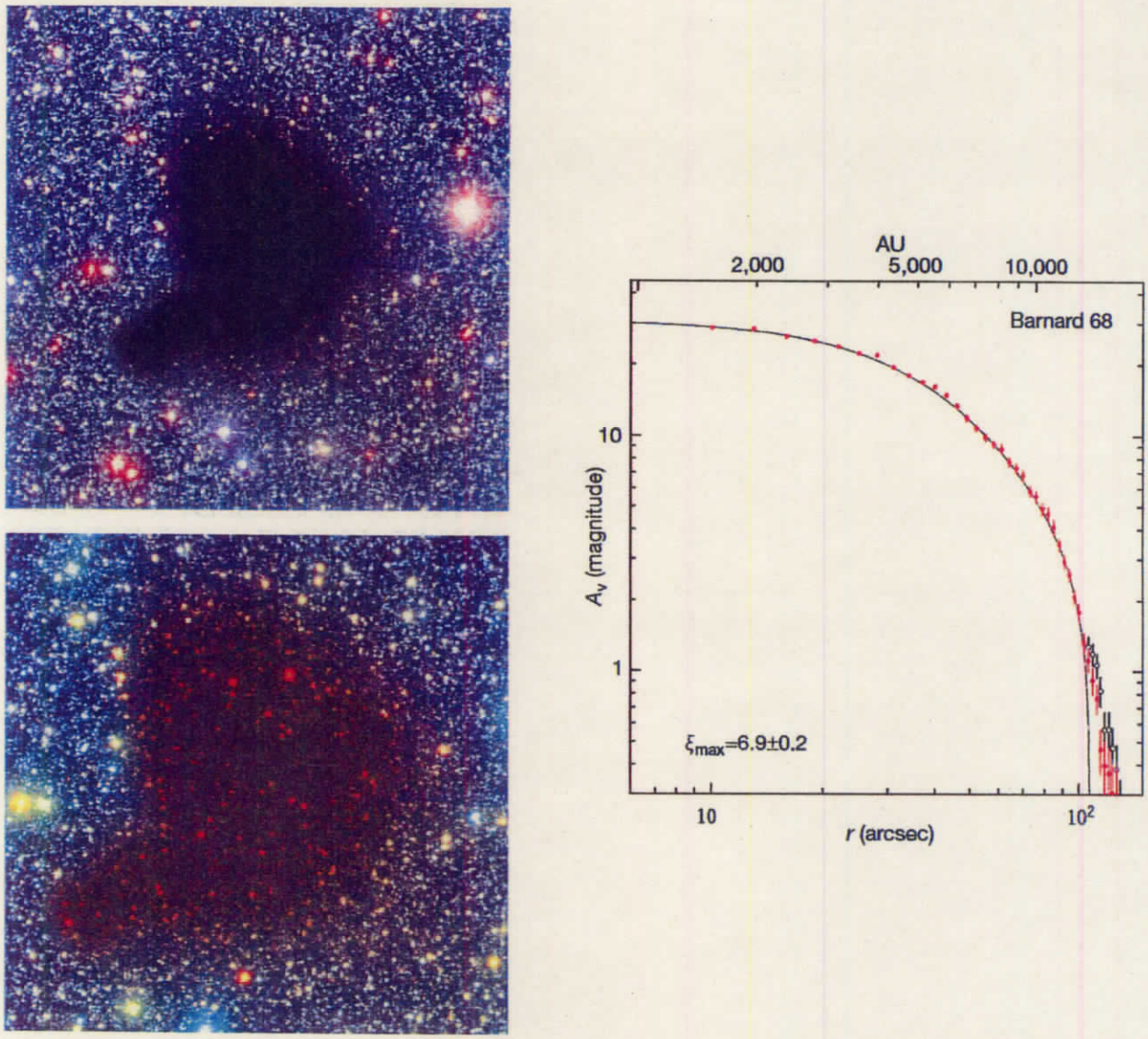

Figure 1.3 Optical and near-infrared images of the globule Barnard 68 (upper left: B, V, and I composite image, lower left: B, I, and K composite image), and the radial A_V profile of the cloud which is well fitted by the Bonnor-Ebert sphere (right). The dots and solid line represent the azimuthally averaged A_V and best-fit solution of the Bonnor-Ebert sphere, respectively. Figures are taken from Alves et al. (2001).

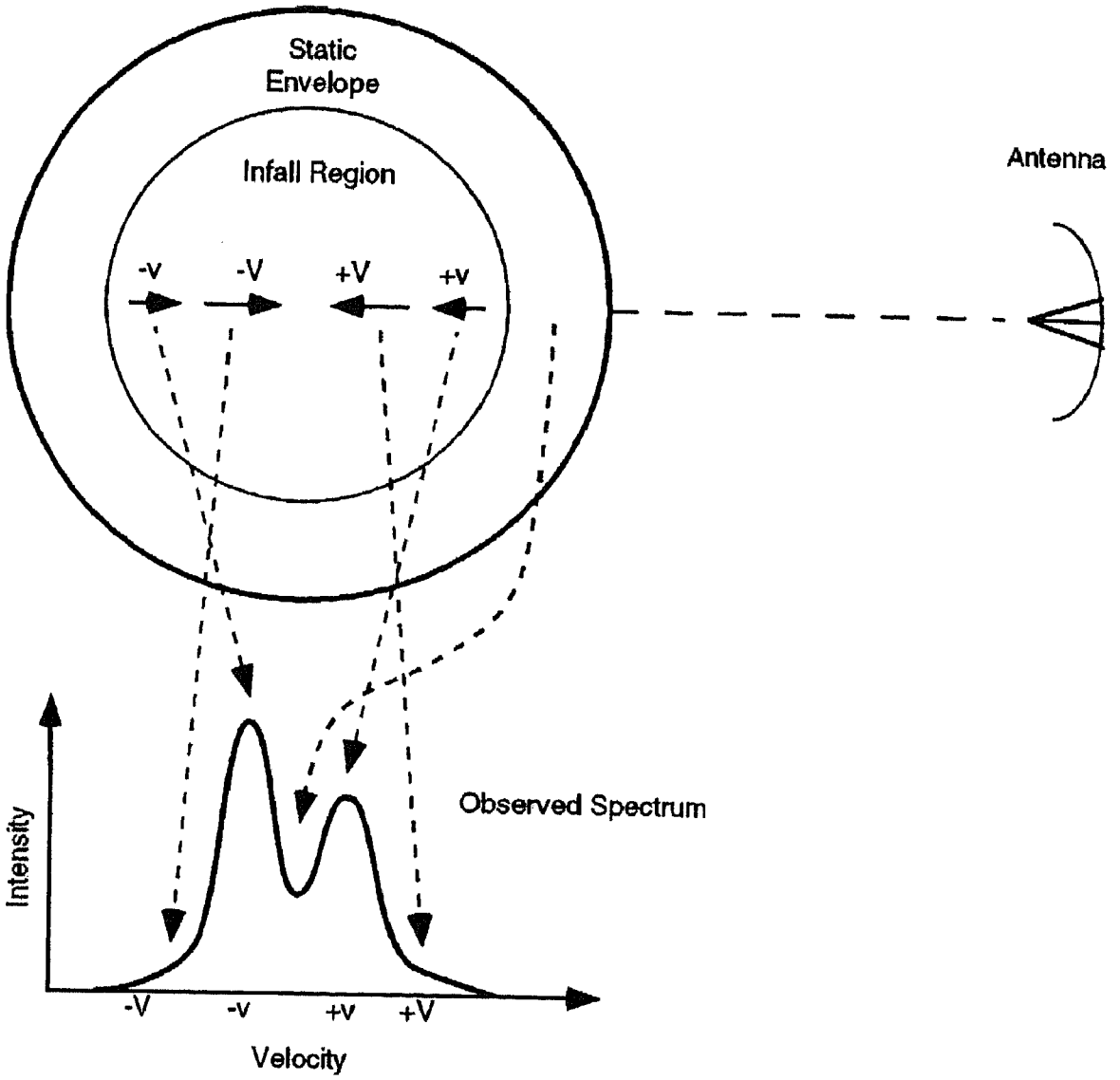

Figure 1.4 A schematic illustration of the asymmetric line profile to be observed from a gravitationally collapsing cloud (figure taken from Evans 1999).

Chapter 2

Near Infrared Imaging Survey of Bok Globules: Density Structure

Kandori, R., Nakajima, Y., Tamura, M., Tatematsu, K., Aikawa, Y., Naoi, T., Sugitani, K., Nakaya, H., Nagayama, T., Nagata, T., Kurita, M., Kato, D., Nagashima, C., and Sato, S., *The Astronomical Journal*, Submitted.

Abstract

On the basis of near-infrared imaging observations, we derived visual extinction (A_V) distribution toward ten Bok globules through measurements of both the color excess (E_{H-K}) and the stellar density at J, H, and K_s (star count). Radial column density profiles for each globule were analyzed with the Bonnor-Ebert sphere model. Using the data of our ten globules and four globules in the literature, we investigated the stability of globules on the basis of $\xi_{\rm max}$, which characterizes the Bonnor-Ebert sphere as well as the stability of the equilibrium state against the gravitational collapse. We found that more than half of starless globules are located near the critical state ($\xi_{\rm max} = 6.5 \pm 2$). Thus, we suggest that a nearly critical Bonnor-Ebert sphere characterizes the typical density structure of starless globules. Remaining starless glob-

ules show clearly unstable states ($\xi_{\rm max} > 10$). Since unstable equilibrium states are not long maintained, we expect that these globules are on the way to gravitational collapse or that they are stabilized by non-thermal support. It was also found that all the star-forming globules show unstable solutions of $\xi_{\rm max} > 10$, which is consistent with the fact that they have started gravitational collapse. We investigated the evolution of a collapsing gas sphere whose initial condition is a nearly critical Bonnor-Ebert sphere. We found that the column density profiles of the collapsing sphere mimic those of the static Bonnor-Ebert spheres in unstable equilibrium. Since the evolutionary timescale increases with decreasing density, the collapsing gas sphere resembles marginally unstable Bonnor-Ebert spheres for a long time. We found that the frequency distribution of $\xi_{\rm max}$ for the observed starless globules is consistent with that from model calculations of the collapsing sphere. In addition to the near-infrared observations, we carried out radio molecular line observations ($C^{18}O$ and N_2H^+) toward the same ten globules. We confirmed that most of the globules are dominated by thermal support. The line width of each globule was used to estimate the cloud temperature including the contribution from turbulence, with which we estimated the distance to the globules from the Bonnor-Ebert model fitting.

2.1 Introduction

Probing the physical evolution of dense cores toward the onset of star formation is of great importance in understanding the nature of the star formation process. The star formation process as well as the characteristics of forming stars are probably mostly determined by the properties of the nursing cores, such as size, mass, temperature, turbulence, and density structure, right before the gravitational collapse. In order to clarify the initial condition of star formation, it is important to provide a number of dense core samples with well defined physical properties.

Bok globules (i.e., isolated molecular cloud cores) are ideal sites for studying isolated star formation processes because of their simple shape and isolated geometry from neighboring

clouds. These characteristics of globules enable us to model their internal structure (e.g., density). For these reasons, detailed observations of some well-known globules have been done. Alves et al. (2001) reported a high-resolution dust-extinction (A_V) study of the starless globule Barnard 68, based on near-infrared observations. They presented a radial column density profile of the globule which is well fitted by the Bonnor-Ebert sphere model (Bonnor 1956; Ebert 1955). Because the density structure is well determined, molecular abundances in Barnard 68 have been studied by comparing dust extinction with molecular distribution (Bergin et al. 2002; Hotzel et al. 2002a, 2002b; Di Francesco et al. 2002; Lai et al. 2003).

An unbiased survey of both starless and star-forming globules is important to provide essential information on the evolution of density, velocity, and chemical structure of globules as well as their relative lifetime. Statistical studies of globules (dense cores) have been conducted based on the observations of thermal dust emission (e.g., Visser et al. 2001, 2002), dust extinction in the mid-infrared (Bacmann et al. 2000), molecular line emission (e.g., Launhardt et al. 1998; Caselli et al. 2002), and a combination of these (e.g., Tafalla et al. 2002; dust and molecular line emissions). However, no statistical studies of the density structure of globules based on the near-infrared extinction have been carried out. Recently, the dust temperature gradient in cold starless cores (e.g., Evans et al. 2001; Ward-Thompson, Andre, & Kirk 2002) has been pointed out, and this may systematically affect the column density distribution derived by assuming a constant dust temperature. The measurements of extinction in the mid-infrared surface photometry (e.g., Bacmann et al. 2000) can also be affected by dust temperature distributions, because both absorption and emission from the line-of-sight medium should be taken into account at these wavelengths. As a column density tracer, near-infrared extinction measurement is one of the most straightforward methods with no ambiguity caused by dust temperature distribution. Near-infrared extinction measurements can trace dust column densities at low-density outer regions of the globules, where (sub)millimeter dust emission cannot be detected.

The aim of our near-infrared (J, H, and K_s) imaging survey of Bok globules is to reveal

the evolution of radial density structures of globules from the starless to protostellar phases as well as to derive their fundamental physical parameters (e.g., size, temperature, mass, and external pressure) on the basis of the measurements of dust extinction. We investigated the radial A_V distribution for each globule using the Bonnor-Ebert sphere model. The solutions of the Bonnor-Ebert sphere can be characterized by the dimensionless radial parameter $\xi_{\rm max}$, which describes the stability of the gas sphere against gravitational collapse, and the critical state is achieved at $\xi_{\rm max}$=6.5. By combining our results for ten Bok globules with previous reports on four sources, we investigate the difference in physical properties, in particular the $\xi_{\rm max}$ value, between the globules in the starless phase and those in the star-forming (protostellar or gravitational collase) phase, which is likely to be related to the difference in evolutionary stages of the globules. In order to investigate the velocity structure of globules, we observed the same globules using the 45 m radio telescope of Nobeyama Radio Observatory with the $C^{18}O$ ($J = 1 \rightarrow 0$) and/or N_2H^+ ($J = 1 \rightarrow 0$) molecular lines.

The procedures of our observations and data reduction are described in § 2.2. The distribution of dust extinction (A_V) for each globule is obtained in order to derive the radial A_V profile and to fit it by the Bonnor-Ebert sphere model (§ 2.3 and 2.4). We investigate the difference in the physical properties between the starless and star-forming globules and discuss implications for the evolution of globules in § 2.5. Our conclusions are summarized in § 2.6.

2.2 Observations and Data Reduction

2.2.1 Source Selection

We observed ten Bok globules, CB 87, CB 110, CB 131, CB 134, CB 161, CB 184, CB 188, FeSt 1-457, Lynds 495, and Lynds 498. These were selected from a unified catalog of dark clouds (Dutra & Bica 2002; compilation of 21 dark cloud catalogs) with the following criteria: (1) globules whose angular sizes are less than $\sim$5′, (2) those having simple shapes (circular

or elliptical), (3) those well isolated from neighboring clouds, (4) those located in the solar neighborhood (distance of less than ~500 pc), and (5) those observable from both hemispheres. The properties of the observed globules are summarized in Table 2.1. Column 1 lists the name of the globule, Columns 2 and 3 list the equatorial coordinates (J2000) of the center of the target field. Column 4 gives the distance to the globule from the catalog (Dutra & Bica 2002). The distance to the nearby and compact globules is difficult to determine. The lack of foreground stars toward globules makes spectro-photometric distance measurements impossible, and the distance estimation from LSR velocity (kinematic distance) is not reliable for nearby clouds. Thus, the listed distances are only values assumed by associating observed globules with neighboring larger molecular clouds whose distance is known. Column 5 represents the association of IRAS point sources within the optical boundary of each globule. A Class I protostar (IRAS 19179+1129) is associated with CB 188 (Launhardt 1996; Yun & Clemens 1992), whereas no evidence of star formation is shown for the other nine globules. For CB 184, a Class II source (IRAS 19116+1623) is located near the globule (Launhardt 1996), but its physical association with the globule is not known. Since star-forming activity is not taking place around the center of CB 184, we will treat CB 184 as a starless globule in this paper. The Bonnor-Ebert model fitting studies of globules based on near-infrared extinction have been reported in four sources in the literature: Barnard 68 (Alves et al. 2001), Barnard 335 (Harvey et al. 2001), Coalsack Globule II (Lada et al. 2004; Racca et al. 2002), and Lynds 694-2 (Harvey et al. 2003). A Class 0 protostar (IRAS 19345+0727) is associated with Barnard 335. The other globules have no IRAS sources, while Lynds 694-2 shows strong evidence of gas inward motion (Lee, Myers, & Tafalla 1999, 2001; Lee, Myers, & Plume 2004). Thus, we will classify Lynds 694-2 as a star-forming globule in this paper. There are two recent reports on the density structure of Coalsack Globule II based on similar analyses. We mainly refer to the observations of Lada et al. (2004) because their near-infrared observations are more sensitive than those of Racca et al. (2002).

2.2.2 Near-Infrared Data

We carried out near-infrared (J, H, and K_s) imaging observations of Bok globules using the infrared camera SIRIUS (Simultaneous three-color InfraRed Imager for Unbiased Surveys; Nagayama et al. 2003; Nagashima et al. 1999) on the 1.4 m telescope, IRSF (InfraRed Survey Facility), at the South African Astronomical Observatory (SAAO). Observations were made over two periods from 2002 July 30 to August 12 and from 2003 June 24 to July 14. SIRIUS has three 1024×1024 pixel HgCdTe infrared detectors (HAWAII array), which enables us to take J, H, and K_s images simultaneously. IRSF/SIRIUS can image a large FOV of ∼7.′7×7.′7 with a scale of 0.″45/pixel, and the limiting magnitudes (S/N=10) for a typical 10-minute exposure time reach 18.9, 18.3, and 17.3 mag at J, H, and K_s, respectively. Thus, this survey is much deeper than previous extensive surveys (e.g., 2MASS, DENIS). For each globule, we performed a 15-minute integration with a set of dithered 20 s or 30 s exposures except CB 110 and FeSt 1-457, whose integration times are 45 and 60 minutes, respectively. The dithered spatial interval was 30″ or 40″. Since the apparent diameter of each target globule is less than 5′, we covered its entire extent at one time. The typical seeing during the observations was 0.″9−1.″4 (FWHM), corresponding to 2−3 pixels. To correct detector flatness and pixel-to-pixel variation, we obtained twilight flat and dark frames at the beginning and end of the nights. We observed some sets of near-infrared standard stars listed by Persson et al. (1998) during the observations for photometric calibration.

We processed the observed data in a standard way of near-infrared image reduction (i.e., dark subtraction, flat-field correction, and median sky subtraction) with the IRAF[1] (Image Reduction and Analysis Facility) and the IDL (Interactive Data Language, by Research Systems, Inc.) routines. After subtraction of averaged dark frame, each object frame was divided by normalized flat frames. For correcting thermal emission pattern and the fringe pattern from

[1] IRAF is distributed by the National Optical Astronomy Observatories, which are operated by the Association of Universities for Research in Astronomy, Inc., under cooperative agreement with the National Science Foundation.

the atomospheric OH emission, we constructed a median sky frame to be subtracted from the object frame. Since all the observed targets are located in the very crowded field of the Milky Way, we did not adopt the self-sky, with which the residual signal of (bright) stars cannot be excluded on the resulting self-sky frame. Therefore, we constructed the sky frame for each band by taking the median of dithered frames toward the different several (four to eight) objects observed in the same night, which resulted in a sky frame with no stellar residuals. This "average" median sky does not reflect the actual sky for each object because the median was taken across several object frames. We compared the "average" median sky frame with the self-sky frame for each object in order to correct their different sky levels, and the final (level-matched) median sky frames were made for each object. Though the thermal emission pattern is adequately corrected in the final median sky frames, the OH fringe pattern is time-averaged. We confirmed that the effect of the time-variation of the OH fringe pattern is within acceptable levels by checking the sky noise level of the final combined object frames. After the sky subtraction and frame-registration, we combined all the dithered images for each object with a 3σ clipping. We show three-color (JHK_s) composite images of globules in Figure 2.1.

For the source detection and photometry, we applied the IRAF/DAOPHOT package (Stetson 1987) to the images. We measured the instrumental magnitudes of the detected stars having a peak intensity greater than 4.0 σ noise level above the sky background by fitting a point-spread function (PSF) and subtracting it from the image. We iteratively performed stellar detections and psf-fitting photometries to the source-subtracted image in order to collect overlooked sources in the previous procedure. We manually checked the results of the photometries and removed some false detections by visual inspection. We summarize the results of stellar detection in Table 2.2. For calculating the plate solution, we matched the pixel coordinates of a number of detected stars with the celestial coordinates of their counterparts in the 2MASS point source catalog (Cutri et al. 2003) and obtained the transformation coefficient using the IRAF/IMCOORDS package, which resulted in an acceptable positional error of less than $0\farcs5$ (rms). All the stars detected in our observations were cataloged separately with respect to

the filters (JHK_s). These stars of single-band detections were used to generate an extinction map at each band with a star count method. We applied the following equations for the color conversion from the IRSF to the standard CTIO/CIT photometric system:

$$(J-H)_{\rm CIT} = 0.980\times(J-H)_{\rm IRSF} + 0.029 \quad \text{for } (J-H)_{\rm IRSF} \geq 0.35, \tag{2.2.1}$$

$$(J-H)_{\rm CIT} = 1.047\times(J-H)_{\rm IRSF} \quad \text{for } (J-H)_{\rm IRSF} < 0.35, \tag{2.2.2}$$

$$(H-K)_{\rm CIT} = 0.912\times(H-K_S)_{\rm IRSF} \tag{2.2.3}$$

These were derived from measurements of red standard stars (see, Nakajima et al. 2004 for details).

2.2.3 Molecular Line Data

We have carried out molecular line observations toward ten globules using the 45 m radio telescope of Nobeyama Radio Observatory over four observing periods (2003 March 10-19, 2003 April 8-10, 2004 January 9-12, and 2004 February 3-10). The observed objects are the same as those observed by IRSF/SIRIUS. The receiver employed was the 25-element focal-plane array receiver BEARS consisting of double-sideband SIS mixers (Sunada et al. 2000). All the target globules in Table 2.1 are mapped in position-switching mode in $C^{18}O$ ($J = 1 \rightarrow 0$) at 109.782173 GHz (JPL catalog; see, http://spec.jpl.nasa.gov/) and/or N_2H^+ ($J = 1 \rightarrow 0$) at 93.1737767 GHz (Caselli, Myers & Thaddeus 1995) on a 13.″7 grid spacing. The half-power beamwidth for each element beam was estimated to be ∼17.″8 at 93 GHz and ∼15.″1 at 109 GHz. The map coverage (∼4′×4′) is sufficiently large compared with the extinction feature of globules. As a back end, we used a digital autocorrelator with a 37.8 kHz frequency resolution (∼0.12 $\rm kms^{-1}$ at 93 GHz, and ∼0.10 $\rm kms^{-1}$ at 109 GHz). The intensity was calibrated using the standard chopper-wheel method, and is expressed in terms of the corrected antenna temperature T_A^*. To correct for the sideband ratio, we calibrated T_A^* using the intensity obtained with the single-sideband receiver S100. The scaling factor from T_A^* of BEARS to that of S100 for N_2H^+

($J = 1 \rightarrow 0$) was measured by ourselves, and that for $C^{18}O$ ($J = 1 \rightarrow 0$) was provided by the observatory. A typical value of the scaling factor for each BEARS element was ~ 1.5. We estimated the main beam efficiency of S100 at 93 and 109 GHz to be 0.515 and 0.442, respectively, by interpolating values at 86, 100, and 115 GHz provided by the observatory. The pointing accuracy was typically better than $7''$ by observing SiO maser sources at 43 GHz every 1-1.5 hours during the observations.

2.3 Derivation of A_V and Molecular Line Parameters

A_V measurement is one of the most straightforward ways to probe the density structure of dark clouds. There are two standard ways to do extinction mapping; one is the star count method (e.g., Dickman 1978; Cambrésy 1999; Dobashi et al. 2004) based on the measurements of the stellar density, and the other is the near-infrared color excess (NICE) method (Lada et al. 1994) based on measurements of the stellar color excess (e.g., E_{H-K}). By considering the stellar density in H and K_s at the densest region of globules, we decided which method is better for each target globule. We analyzed CB 131, CB 134 and CB 188 with the star count method and analyzed the other globules with the NICE method.

2.3.1 Star Count

On the basis of the stars detected in the J, H, and K_s bands, we derived extinction maps (A_J, A_H, and A_{K_s}) for CB 131, CB 134, and CB 188 using the star count method (see, e.g., Kandori et al. 2003). A logarithmic cumulative stellar density $\log N$ measured at the magnitude $m_{\lambda,0}$ can be converted to extinction A_λ as

$$A_\lambda\left(\Delta\alpha, \Delta\delta, m_{\lambda,0}\right) = m_{\lambda,0} - f^{-1}\left[\log N(\Delta\alpha, \Delta\delta, m_{\lambda,0})\right] \tag{2.3.1}$$

where $\Delta\alpha$ and $\Delta\delta$ are the offset positions from the equatorial coordinate of image center, and f^{-1} is the inverse function of $f = \log N_{\rm ref}(m_\lambda)$, which is the logarithmic cumulative luminosity function (i.e., Wolf diagram; Wolf 1923) constructed in the extinction-free reference field (see Fig. 2.2). Though f is often assumed to be linear as $f = a + bm_\lambda$, we fitted it with a 4th-order polynomial because the function shows a slightly curved shape.

To measure stellar density distribution, $\log N(\Delta\alpha, \Delta\delta, m_{\lambda,0})$, we arranged circular cells (typically $\sim$30″ in diameter) separated by 9″ intervals on each observed field ($\sim$7′×7′ area), and counted the number of stars falling in the cells up to the threshold magnitude $m_{\lambda,0}$ (see Table 2.2 for the definition) which is well above the limiting magnitudes. The diameter of circular cells depends on the stellar density in each cloud field. We smoothed the stellar density map with a Gaussian filter (FWHM=13.″5) to reduce noise. In order to derive A_J, A_H, and A_{K_s}, we numerically calculated f^{-1} in equation (2.3.1) after substituting the actually measured stellar density $\log N(\Delta\alpha, \Delta\delta, m_{\lambda,0})$ into f^{-1}. In the resulting extinction maps, A_J tends to be saturated at the densest region of the cloud, but sufficiently reveals the diffuse extinction feature around the cloud, and A_{K_s} has the opposite tendency. In order to relieve saturation, we made a composite A_V map by combining the A_J, A_H, and A_{K_s} data with the following equation:

$$A_V = \alpha R_{K_sV} A_{K_s} + (1-\alpha) R_{HV} A_H \quad \text{for } A_H \geq A_H^{\rm max}/2 \tag{2.3.2}$$

$$A_V = \beta R_{HV} A_H + (1-\beta) R_{JV} A_J \quad \text{for } A_H < A_H^{\rm max}/2 \tag{2.3.3}$$

where α and β are the weighting parameters defined as $A_H/A_H^{\rm max}$ and $A_H/(A_H^{\rm max}/2)$ where $A_H^{\rm max}$ denotes the maximum value of A_H in each analyzing field. The $R_{\lambda V}$ denotes the standard conversion factor from A_λ to A_V in Rieke & Lebofsky (1985), which is 3.55 and 5.71 for J and H, respectively. For K_s, we assumed $A_V = 9.44A_{K_s}$ on the basis of equation (2.2.3) and the conversion factors in Rieke & Lebofsky (1985). These conversion factors depend on the assumption of dust optical properties, in particular R_V. We discuss systematic uncertainties in the derivation of A_V in the Appendix. The resulting A_V maps for CB 131, CB 134, and CB

188 are shown in Figure 2.2. Typical uncertainty of A_V in the reference field ($A_V \sim 0$ mag) is estimated to be ~0.9 mag.

2.3.2 Near-Infrared Color Excess

On the basis of the stars detected both in the H, and K_s bands, we derived extinction (A_V) maps for CB 87, CB 110, CB 161, CB 184, FeSt 1-457, Lynds 495, and Lynds 498 using the NICE method. If we assume that the population of stars toward the observed field is invariable, the mean stellar color in the reference field $< H - K >_{\rm ref}$ can be used as the zero point of color excess. The color excess distribution toward globules can be derived by subtracting $< H - K >_{\rm ref}$ from the observed $H - K$ of stars. Since the extent of each analyzed field is relatively small ($\sim 7' \times 7'$), our assumption on invariant stellar population seems plausible. To measure color excess distribution, we arranged circular cells (~30″ diameter) spaced at 9″ (the same alignment as used in the star count analysis) on each observed field. We calculated the mean stellar color in each cell and derived their color excess as

$$E_{H-K}\left(\Delta\alpha, \Delta\delta\right) = \left[\sum_{i=1}^{N} \frac{(H-K)_i}{N}\right]\left(\Delta\alpha, \Delta\delta\right) - \langle H-K\rangle_{\rm ref}, \qquad (2.3.4)$$

where $(H - K)_i$ is the color index of the i-th star in a cell, and N is the number of stars falling in a cell. $\langle H - K\rangle_{\rm ref}$ is the mean color of stars in the reference field (see, Fig. 2.2). We converted the $H - K$ color excess to A_V using the reddening law of Rieke & Lebofsky (1985) as $A_V = 15.9 \times E_{H-K}$. We then smoothed the resulting A_V map in the same manner as used in the star count analysis. The resulting A_V maps are shown in Figure 2.2. Typical uncertainty of A_V in the reference field ($A_V \sim 0$ mag) is estimated to be ~0.6 mag.

2.3.3 Molecular Line Parameters

We derived the observed molecular line parameters, LSR velocity, peak temperature, line width, and effective sound speed, for each globule. We observed N_2H^+ ($J = 1 \rightarrow 0$) for FeSt 1-457

and $C^{18}O$ ($J = 1 \rightarrow 0$) for the other globules. We show the spectrum observed at the center of each globule in Figure 2.3. For the N_2H^+ spectrum fitting we took into account their hyperfine structure and line optical depth effect (using the same procedure as described in Tatematsu et al. 2004). The intrinsic relative intensity and rest frequency of hyperfine components are taken from Tiné et al. (2000) and Caselli et al. (1995), respectively.

We derived the total line width $\Delta V_{\rm tot}$ and non-thermal line width $\Delta V_{\rm NT}$ for the spectrum by assuming that a gas kinetic temperature $T_{\rm k}$ is equal to 10 K. $\Delta V_{\rm tot}$ and $\Delta V_{\rm NT}$ can be obtained from $\Delta V_{\rm NT}^2 = \Delta V_{\rm obs}^2 - (8{\rm ln}2)kT_{\rm k}/m_{\rm obs}$, and $\Delta V_{\rm tot}^2 = \Delta V_{\rm NT}^2 + (8{\rm ln}2)kT_{\rm k}/m$, where m and $m_{\rm obs}$ is the mean molecular weight (2.33 amu) and the mass of the observed molecule. The thermal line width $\Delta V_{\rm T}(= (8{\rm ln}2)kT_{\rm k}/m)$ for $m = 2.33$ amu and $T_{\rm k} = 10$ K, is 0.443 km s^{-1}. Derived line widths are listed in Table 2.3. We found that thermal line width is larger than non-thermal line width for most of the observed globules. Thus, it is likely that observed globules are dominated by thermal support with a small contribution from the non-thermal turbulence. The thermal and non-thermal components of the line width can be characterized by a temperature as $T_{\rm k} = \Delta V_{\rm T}^2 m/k8{\rm ln}2$ and $T_{\rm NT} = \Delta V_{\rm NT}^2 m/k8{\rm ln}2$, respectively. We derived $T_{\rm eff} = T_k + T_{\rm NT}$ for each globule in Table 2.3 as a cloud-supporting temperature which includes non-thermal contribution. In order to estimate the distance to the globules, we will use $T_{\rm eff}$ in combination with the Bonnor-Ebert model fitting of globules in §2.4.2. In this paper, we only use the information on molecular line width. Detailed studies such as comparison between dust extinction and molecular distribution will be reported in a subsequent paper.

2.4 Density Structure

2.4.1 Bonnor-Ebert Sphere Model

In order to model the internal density structure of Bok globules, we used the Bonnor-Ebert sphere model (Bonnor 1956; Ebert 1955), which is a modified Lane-Emden equation describing a

pressure-confined self-gravitating isothermal gas sphere in hydrostatic equilibrium. The density structure of a Bonnor-Ebert sphere can be obtained by solving the following equation:

$$\frac{1}{\xi^2}\frac{d}{d\xi}\left(\xi^2\frac{d\phi}{d\xi}\right) = e^{-\phi} \tag{2.4.1}$$

where ϕ is the logarithmic density contrast, $\phi(\xi) = -\ln(\rho/\rho_c)$; ρ and ρ_c are the volume density and central volume density, respectively. ξ is the dimensionless radial parameter, $\xi = (r/C_s)\sqrt{4\pi G\rho_c}$; r, G, and C_s are the radius, gravitational constant, and isothermal sound speed, $C_s = (kT/m)^{1/2}$, where k, T, and m are the Boltzmann constant, kinetic temperature, and mean mass of the molecule (2.33 amu), respectively. Under the standard boundary conditions, $\phi(0) = 0$ (i.e., $\rho = \rho_c$ at $r = 0$) and $d\phi(0)/d\xi = 0$ (i.e., $d\rho/dr = 0$ at $r = 0$), equation (2.4.1) can be solved with numerical integration. If the gas sphere is confined by external pressure P_{ext} at the core boundary radius R, the solutions of the Bonnor-Ebert sphere can be characterized by the dimensionless radius $\xi_{max} = \xi(r = R)$ as

$$\xi_{max} = \frac{R}{C_s}\sqrt{4\pi G\rho_c}. \tag{2.4.2}$$

ξ_{max} is a stability measure of the gas sphere against the gravitational collapse (Bonnor 1956; Ebert 1955). Critical state is achieved at $\xi_{max} = 6.5$ corresponding to the density contrast of $\rho_c/\rho_R = 14$. For a solution with $\xi_{max} > 6.5$, the equilibrium state is unstable to the gravitational collapse. The Bonnor-Ebert sphere mass M and the external pressure P_{ext} are calculated as

$$M = 4\pi\alpha^3\rho_c\xi_{max}^2\left(\frac{d\phi}{d\xi}\right)_{\xi=\xi_{max}} \tag{2.4.3}$$

$$P_{ext} = C_s{}^2\rho_c e^{-\phi(\xi_{max})} \tag{2.4.4}$$

where $\alpha = C_s/(4\pi G\rho_c)^{1/2}$.

2.4.2 Bonnor-Ebert Model Fitting of Bok Globules

Derivation of Column Density Profile

For a comparison of observational data (i.e., A_V) with a theoretical Bonnor-Ebert density distribution, radial A_V profiles for each globule were constructed. We set annuli spaced at $9''$ around the center of the core that is the A_V intensity peak (see Table 2.4), and calculated averaged A_V values at each annulus (see Figure 2.4). For apparently elliptical globules (CB 87, CB 161, and CB 184) we performed ellipse fitting to the A_V distribution, and "equivalent" radius, $r = \sqrt{ab}$, was substituted for radius where a and b are the respective semi-minor and semi-major axes of the ellipse for the cores. Fitted ellipticity and position angle for the globules are listed in Table 2.4. It is possible that the observed globules with circular projected shapes are actually pole-on prolate ellipsoids. In this case, the shape of the observed A_V profile should be steeper than that for the intrinsic shape. Since there is no effective method for estimating how ellongated a globule is along the line of sight, we assumed that the line of sight length of globules is the same as the projected diameter.

We manually masked extinction features likely to be unrelated to the globules (e.g., the other clouds on the same image, diffuse streaming feature; see Fig. 2.2), and masked regions were omitted in the circularly averaging procedure. Furthermore we recalibrated the relative zero point of extinction for the analyzed globules by subtracting background extinction (i.e., A_V offset value). The A_V offsets have been derived from averaging A_V within the annulus of $150''$ to $200''$ radius, which is sufficiently larger than the primary extinction feature of globules. Actually, the subtracted values as A_V offset are small (typically $\sim$ 0.5 mag), and it solely depends on where we set the reference fields in the star count or color excess analysis. In order to convert A_V to the H_2 column density, we used the relationship between the optical color excess E_{B-V} and the hydrogen column density, $N(\mathrm{HI} + \mathrm{H_2})/E_{B-V} = 5.8 \times 10^{21}$ cm^{-2} mag^{-1} (Bohlin, Savage, & Drake 1978), where $N(HI + H_2) = N(\mathrm{HI}) + 2N(\mathrm{H_2})$. This relationship is based on the UV absorption line measurements toward the stars of slightly obscured lines of

sight ($E_{B-V} \lesssim 0.5$ mag). By assuming that (1) all hydrogen in the cloud is in a molecular form and that (2) the ratio of total-to-selective extinction $R_V (\equiv A_V/E_{B-V})$ is equal to the standard ISM value of 3.1 (e.g., Whittet 1992), we obtained $N(\mathrm{H_2})/A_V = 9.4 \times 10^{20}$ cm^{-2} mag^{-1}, and used it to derive the H_2 column density. The resulting column density profiles are shown in Figure 2.4.

Derivation of Model Parameters

Since the particular solution of the Bonnor-Ebert sphere is characterized by the parameter $\xi_{\max}$ (Eq. [2.4.2]), we set radius R, temperature T, and central density ρ_c of the sphere as free parameters in the fitting procedure of the Bonnor-Ebert sphere. In order to construct a model density profile, we performed numerical integration to the two first order equations as divisions of equation (2.4.1). Resulting ξ and ϕ are scaled to derive the radius and density in a model density profile. For the different values of R, T, and ρ_c, the corresponding model density profile changes accordingly. We integrated the model profile at each impact parameter to calculate the column density. In order to match the resolution between the model and the actual column density data, the model column density projected onto the $\Delta\alpha$-$\Delta\delta$ plane was convolved with the same beam as used in the star count or color excess analysis (cylinder-shaped beam convolved with the Gaussian), and we constructed a column density profile for a Bonnor-Ebert sphere. We made calculations of the resolution-matched Bonnor-Ebert column density profile for various free parameters, and evaluated the fit for resulting density distributions by calculating a reduced χ^2. In Figure 2.4, we show the result of the Bonnor-Ebert fit to the radial column density profile of the globules. The dots and error bars represent the average $N(\mathrm{H_2})$ values at each annulus of 9″ intervals and the rms values of data points in each annulus, respectively. The solid line denotes the radial column density profile of the best-fit Bonnor-Ebert sphere which is convolved with the same beam as used in the A_V measurements. The dashed line denotes the Bonnor-Ebert model profile before the convolution. In Tables 2.4 and 2.5, we list the derived Bonnor-Ebert parameters for globules including previous reports on

four sources (Barnard 68, Barnard 335, Coalsack Globule II, and Lynds 694-2).

In the χ^2-procedure, coverage of the fitting part in the radial profile ranges from the minimum radius (center) to the radius where the observed A_V value reaches $\sim$1 mag (detection limit). In some cores (Lynds 495 and Lynds 498), deviation of observed profiles from the Bonnor-Ebert sphere appeared at diffuse outskirts ($A_V \lesssim 1$ mag), for which we reset the fitting part to avoid the apparent deviation. The Bonnor-Ebert fitting parameters were actually well constrained from the data within the "shoulder" of the density distribution; the χ^2-fitting results are not sensitive to the selection of fitting part unless there is no significant kink in the column density profile. In Figure 2.5 we show the example of χ^2 distribution for CB 161 on the $\rho_c - R$, $\rho_c - T$, and $R - T$ plane. We estimated the uncertainty in the best-fit parameter by taking the second derivative of χ^2 with respect to each parameter b_j at the region of the χ^2 minimum as $\sigma_j^2 = 2(\partial^2\chi^2/\partial b_j^2)^{-1}$ (e.g., Bevington & Robinson 1992), where σ_j is the one-sigma uncertainty for each parameter, in our case, δR, $\delta\rho_c$, and δT. We discuss possible systematic uncertainties in the derivation of $\xi_{\max}$ in the Appendix.

Distance to the Globules

Since there are no effective methods for accurately measuring distance to the starless, compact, and nearby ($d \lesssim 300$ pc) globules except for the limited case (e.g., interaction with HII region of known distance, existence of foreground stars toward them), the distances listed in Table 1 are only values assumed in consideration of the known distance to neighboring dark clouds. Recently, Hotzel et al. (2002b) and Lai et al. (2003) presented detailed discussion on the relation between the physical parameters of a Bonnor-Ebert sphere. On the basis of the column density measurements and the radial profile fitting with the Bonnor-Ebert sphere, the dimensionless radius $\xi_{\max}$, angular radius θ_R, and central column density N_c can be determined from observations. Substituting the relations of $R = \theta_R D \propto D$ and $\rho_c \propto N_c\theta_R^{-1}D^{-1} \propto D^{-1}$ into equation (2.4.2), we can obtain $D^{-1}T$ =constant (Lai et al. 2003). If the temperature T is accurately determined from observations, the distance to the globules can be constrained.

Theoretically, supporting force in a Bonnor-Ebert sphere is purely thermal pressure, but actual clouds also have non-thermal support, e.g., turbulence and magnetic fields, which are widely observed in molecular clouds (see, e.g., Larson 2003). We assume that non-thermal support can be included in the model by replacing the isothermal sound speed $C_s = (kT_k/m)^{1/2}$ in equation (2.4.2) with the effective sound speed $C_{eff} = (kT_{eff}/m)^{1/2}$, where $T_{eff} = T_k + T_{NT}$ (see §2.3.3). On the basis of T_{eff} from our molecular line observations, we corrected the initially assumed distance to the globules d_{ini} (see Table 2.1) as $d = (T_{eff}/T_{BE})d_{ini}$ where T_{BE} is the best-fit temperature of a Bonnor-Ebert sphere under an assumed distance of d_{ini}, and d is the corrected distance. Finally we derived all the distance-dependent parameters of best-fit Bonnor-Ebert spheres (e.g., radius, central density, and mass) as listed in Table 2.5. We note that the corrected distance to the starless globule FeSt 1-457 is estimated to be $\sim$ 70 pc, which makes this globule one of the nearest dark clouds.

2.5 Discussion: Stability and Evolution of Globules

In this section, we discuss the internal structure and stability of globules by using the data of the ten globules from our observations and four from the literature.

2.5.1 Physical Properties of Globules

Though we have estimated physical properties of globules by assuming the Bonnor-Ebert model, there are actually other theoretical models (e.g., Shu 1977; Larson 1969; Penston 1969; McLaughlin & Pudritz 1997; Plummer 1911). Bacmann et al. (2000) presented that a Bonnor-Ebert-like model (a finite size sphere with inner uniform density region and $\rho \propto r^{-2}$ outer envelope) fits well with the column density profile of globules obtained from mid-infrared 7 μm absorption measurements, but that a singular-isothermal-sphere (SIS) or singular logotrope sphere cannot reproduce the observed profile well. By considering the resolution of our extinction maps ($\sim$30″) and possible geometric error of globules (e.g., deviation from spherical

symmetry), it is not possible to make meaningful comparisons between the Bonnor-Ebert model and other Bonnor-Ebert-like models (see, e.g., Figure 2 in Harvey et al. 2003, which compares the Bonnor-Ebert model with a Plummer-like model). Here, we simply assume the Bonnor-Ebert model.

As described in the previous section, the dimensionless radial parameter $\xi_{\rm max}$ determines the shape of a Bonnor-Ebert density profile as well as the stability of the equilibrium state against the gravitational collapse. We plot globules on the $\xi_{\rm max}$ versus density contrast diagram in the upper panel of Figure 2.6. Since $\xi_{\rm max}$ has one-to-one correspondence with density contrast, all the Bonnor-Ebert spheres are distributed along the solid curved line. We found that more than half of starless globules (7 out of 11 sources) are located near the critical state, $\xi_{\rm max} = 6.5 \pm 2$. Thus, we suggest that a nearly critical Bonnor-Ebert sphere characterizes the typical density structure of starless globules. The remaining starless globules show clearly unstable states ($\xi_{\rm max} > 10$). When we divide starless globules into two groups with respect to the critical line ($\xi_{\rm max} = 6.5$), there are three stable starless globules and eight unstable starless globules. The majority of starless globules is located in the unstable states ($\xi_{\rm max} > 6.5$) if the uncertainties in $\xi_{\rm max}$ are not taken into account. We also found that all the star-forming globules have larger $\xi_{\rm max}$ values (> 10) than that of the critical Bonnor-Ebert equilibrium state, which is consistent with the fact that they have started gravitational collapse. In the lower panel of Figure 2.6, we show the fitting error in $\xi_{\rm max}$ for each globule. Filled gray circles denote the fitting results for some globules with considerable features of ambient extinction if the masked region on the A_V map (see Fig 2.2) is included in the derivation of the column density profile. In addition to the $\xi_{\rm max}$ diagram in Figure 2.6, we made histograms of logarithmic density contrast for starless and star-forming globules (Figure 2.7). Similar characteristics as descrived above can also be seen in the histograms.

To see the relationships between derived physical properties of globules in Tables 2.4 and 2.5, we made correlation diagrams between density contrast and the other physical parameters of globules in Figure 2.8. We consider that the horizontal axis (density contrast) represents

the evolutionary states of globules, because globules should evolve toward higher central condensation to form stars. We can see from panels (e) and (f) in the figure that temperature $T_{\rm eff}$ and external pressure $P_{\rm ext}$ of globules appear roughly constant regardless of the density contrast. If we assume constant $T_{\rm eff}$ and $P_{\rm ext}$, the Bonnor-Ebert model parameters for each density contrast value can be constrained. The broken line in each panel is the relationship for the Bonnor-Ebert spheres with a constant $T_{\rm eff}$ of 13.2 K and $P_{\rm ext}$ of 5.3×10^4 K cm^{-3}, which are the median values for the globule samples. The median value of $P_{\rm ext}$ is slightly larger than the previously reported ISM pressure in the solar vicinity of $\sim 2.8 \times 10^4$ K cm^{-3} (McKee 1999).

The overall trend in the data point distributions in Figure 2.8 can be approximated by Bonnor-Ebert spheres with a constant "effective" temperature and a constant external pressure. The relations for the radius and mass (panels [c] and [d]) remain roughly constant against the density contrast, suggesting that these quantities are not sensitive to the evolutionary states of globules. This result agrees with the N_2H^+ observations of molecular cloud cores in Taurus (Tatematsu et al. 2004), in which there is no remarkable difference in core radius and mass between starless cores and cores with stars. Since the density at core boundary is derived from $P_{\rm ext}/T_{\rm eff}$, the density at core center $n_{\rm c}$ is directly obtained for each density contrast value and shows a proportional relationship against the density contrast as shown in panel (b). Accordingly, the density contrast and A_V show positive correlation. The data points in panel (a) are located slightly lower than the broken line because of a beam dilution effect in the A_V measurements with $\sim 30''$ resolution. For molecular cloud cores located in regions of higher pressure (e.g., dark cloud complex) than in the solar vicinity, the Bonnor-Ebert relationship in panels (a) and (b) should be shifted upward corresponding to the larger value of $P_{\rm ext}/T_{\rm eff}$. We can see from panel (a) that the density contrast value is simply estimated from the A_V (column density) measurements under the assumption of the Bonnor-Ebert sphere with a constant $T_{\rm eff}$ and $P_{\rm ext}$.

2.5.2 On the Selection Bias of the Globule Samples

Here we briefly consider the selection bias in our globule samples. The peak A_V values for our observed globules range from $\sim$ 6.5 to 41 mag. We selected globules that were opaque at optical wavelengths, i.e., with few stars in the background of the cloud on the Digitized Sky Survey image. These sources are expected to have A_V greater than at least 5 mag, and expected to be sites of future star formation, i.e., so-called "dense cores". The lower limit of the peak A_V for the globules may be determined by the criterion in our target selection. Thus, it is possible that the diffuse cores of low column densities are not included in our globule sample as in the case of previous studies on dense cores (e.g., Visser et al. 2002; Lee & Myers 1999; Jijina et al. 1999).

2.5.3 Implications for the Stability of Globules

It is interesting that there are starless globules showing larger density contrast than that of the maximum value ($\sim$14) for stable Bonnor-Ebert spheres (see § 2.5.1), because unstable equilibrium states should not last long without any extra stabilizing force such as magnetic pressure and/or turbulent pressure (e.g., McKee & Holliman 1999). Since unstable equilibrium states cannot last long, the globules of large density contrast should not exactly be the Bonnor-Ebert sphere even if they mimic the Bonnor-Ebert density profile. Similar results have also been reported from the mid-infrared extinction study of starless dense cores (density contrasts are generally $\sim$10$-$80; see Table 3 of Bacmann et al. 2000). If we consider a simple case in which the non-thermal pressure components have the same radial dependence as the thermal pressure, the theoretical Bonnor-Ebert model can be modified by replacing its kinetic temperature term with $T_{\rm eff}$ as described in § 2.4.2. In this case, the shape of the Bonnor-Ebert density profile as well as the stability criteria (i.e., the value of $\xi_{\rm max}$ or maximum density contrast) hold unchanged compared with the purely thermally supported case. This modification cannot provide a realistic explanation for the stability of the large density contrast globules, suggesting

either that they are already collapsing toward higher central condensation as discussed in § 2.5.4, or that the stabilizing mechanisms accounting for their large density contrast are more complex. The Bonnor-Ebert assumption for the globules is not valid in these cases. We note that our result is in marked contrast to one in which most of the clumps observed at 850 μm dust emission in the Orion B molecular cloud complex are in stable equilibrium based on the Bonnor-Ebert analysis (Johnstone et al. 2001).

A non-isentropic multi-pressure polytrope model (McKee & Holliman 1999) may provide successful interpretation allowing larger density contrast than that of the critical Bonnor-Ebert sphere. Curry & McKee (2000) developed a composite polytrope model which also allows large density contrast. These two models provide a stable equilibrium solution of arbitrarily large density contrast by adjusting the contributions from the non-thermal pressure components, i.e., turbulent and magnetic pressure. Galli et al. (2002) studied the effects of the interstellar radiation field (ISRF) on the cloud stability. They reported that a cloud's maximum density contrast increases with increasing intensity of the ISRF if the stabilizing effect of external heating of the cloud as well as produced temperature gradient are considered. These models are possible alternatives to the Bonnor-Ebert sphere providing larger value of maximum density contrast (> 14). The shape of their density profiles have characteristics similar to those of the Bonnor-Ebert sphere (see, Fig. 3 and 4 in Galli et al. 2002, Fig. 10 in McKee & Holliman 1999), that is a flat inner region surrounded by steeper envelope decreasing with power-law, in particular $\rho \propto r^{-\alpha}$ where $\alpha \sim 2$. It seems difficult to distinguish them only from the observed shape of the density profile. In other words, each model should provide similar density profiles and corresponding density contrast values for the same observational dataset. Detailed observations of velocity and temperature structure of dense cores are needed to determine the most realistic model.

Major differences among the models discussed above are the supporting mechanisms of the cloud and the stability criterion, i.e. the value of the critical density contrast. The actual density contrast value for globules can be obtained through the Bonnor-Ebert fit (see Table

2.4), but its critical value is not always known (i.e., model dependent). Molecular cloud cores will evolve toward higher central condensation and start collapsing when their density contrast exceeds a certain critical value. Based on this argument, initial density structure of globules right before the collapse can be determined if we constrain the value of its critical density contrast. Initial density conditions for star formation will provide a good starting point for the theoretical calculations. For example, given initial density profile of a globule, time evolution of mass accretion rate can be calculated (e.g. Whitworth & Ward-Thompson, 2001), which is a key parameter for constraining the mass of a newly formed star.

In order to estimate the value of critical density contrast from observations, it should be worth investigating the frequency distribution of density contrast for a number of starless globules. Since unstable equilibrium states should not be long sustainable, we expect that the detection probability for stable globules is much higher than that for unstable ones. Thus, it is likely that the frequency distribution of density contrast shows a sharp decrease toward larger density contrasts at a certain bin, which should correspond to the density contrast critical for collapse. Though the number of our samples (11 sources) is not large, we present the histogram of density contrast for the starless globules in Figure 2.7. The density contrast of the starless globules is mostly populated near the critical Bonnor-Ebert sphere and decreases toward the larger density contrast, suggesting that the actual critical density contrast of globules is not very different from that for the Bonnor-Ebert sphere. We note that the decrease toward a smaller density contrast may be caused by the detection limit (see, § 2.5.2) and/or the formation mechanism of globules. A statistical study with a larger number of samples is our future plan.

In Table 2.4, three of fourteen globules are fitted as a stable equilibrium state of the Bonnor-Ebert sphere. These stable globules might increase their density contrast quasi-statically toward the onset of dynamical collapse with gradually increasing external pressure and/or with decreasing internal turbulent pressure (Nakano 1998). For the case of rapid increase of external pressure, core collapse triggered by a compression wave should be taken into account (e.g., Hennebelle et al. 2003, 2004; Motoyama et al. 2004).

2.5.4 Slow Collapse of A Nearly Critical Bonnor-Ebert Sphere

After gravitational collapse begins, globules evolve toward higher central condensation. If we assume an extreme case in which all the globules fitted as unstable Bonnor-Ebert equilibrium states are already collapsing, the difference in $\xi_{\rm max}$ is attributed to different evolutionary stages of globules. Since the Bonnor-Ebert spheres provide a good fit to starless globules, it is meaningful to consider the gravitational collapse of the Bonnor-Ebert sphere (e.g., Foster & Chevalier 1993; Ogino, Tomisaka, & Nakamura 1999). We expect that the critical Bonnor-Ebert sphere can approximate the initial condition of collapse, because a large fraction of the starless globules are located near the critical state, $\xi_{\rm max} = 6.5 \pm 2$, as shown in § 2.5.1.

In order to make quantitative comparisons of the density structures between our observations and a collapsing gas sphere starting from a nearly critical Bonnor-Ebert sphere, we used the result of theoretical calculations from Aikawa et al. (2004). In their calculation, the central density $n_{\rm c}$(H) and kinetic temperature T of the critical Bonnor-Ebert sphere were set as $n_{\rm c}({\rm H}) = 2 \times 10^4$ cm^{-3} and $T = 10$ K, respectively. No cloud rotation, magnetic fields, or non-thermal turbulence were considered, and a fixed boundary condition of zero velocity was adopted at the outermost radius of $R = 0.2$ pc, which is slightly larger than the critical radius of an equilibrium sphere (see, Aikawa et al. 2004). We note that the initial condition parameters of $n_{\rm c}$(H), T, and R, are consistent with the observed physical properties of globules around $\xi_{\rm max} = 6.5$ (see, Tables 2.4 and 2.5). The initial density distribution was multiplied by a constant factor α of 1.1 in order to initiate collapse. The slight density enhancement of $\alpha = 1.1$ is preferable to approximate the collapse from a nearly critical Bonnor-Ebert sphere. The time scale of the collapse is several times the free-fall time, $\sim 1.2 \times 10^6$ yr ($\sim 4 \times t_{\rm ff}$), which is comparable with the observational lifetime of starless dense cores ($\sim 10^6$ yr; e.g., Visser et al. 2002; Lee & Myers 1999).

Figure 2.9 shows the evolution of a radial column density profile of the collapsing sphere for the case of $\alpha = 1.1$ described above. The gray solid line denotes initial column density

profile (t = 0 yr), and the black solid, dotted, and broken lines denote density profile at specific times of 4.4×10^5, 4.4×10^5, and 1×10^6 yr, respectively. We found that the column density profiles of the collapsing sphere are well fitted with the static Bonnor-Ebert spheres (equilibrium solutions) in the range of $\xi_{\rm max} < 25$ within the relative density difference of 2%. The plus symbols show the best-fitting result for each collapsing profile with the Bonnor-Ebert sphere, which are labeled with corresponding $\xi_{\rm max}$ values; for example, the density profile of the collapsing sphere at 4.4×10^5 yr mimics the unstable Bonnor-Ebert sphere of $\xi_{\rm max} = 7.6$. This result suggests that observed starless globules with large density contrasts are gravitationally collapsing objects. Figure 2.10 shows the relationship between $\xi_{\rm max}$ versus density contrast. The solid line is for the Bonnor-Ebert sphere, and the dotted line is for the collapsing sphere which plots the best-fitting $\xi_{\rm max}$ values against the density contrast of the collapsing sphere. The plus symbols denote the elapsed time of the collapsing sphere at 10% intervals of the total collapse time. Since the free-fall time scale increases with decreasing density, a collapsing gas sphere starting from a nearly critical Bonnor-Ebert sphere should mimic marginally unstable Bonnor-Ebert spheres for a long time. Thus, this is qualitatively consistent with the fact that the $\xi_{\rm max}$ for the starless globules is mostly populated near the critical state (7 out of 11 sources) and the remaining starless globules show clearly unstable states ($\xi_{\rm max} > 10$; 4 out of 11 sources) as shown in § 2.5.1. From the model prediction, we note that 50% of collapsing globules should be located in $\xi_{\rm max} = 6.5 - 8.5$, and the rest of the globules should have $\xi_{\rm max}$ larger than ~8.5. The fraction is consistent with our result that half of the starless globules with $\xi_{\rm max} > 6.5$ are located in $\xi_{\rm max} = 6.5 - 8.5$ (4 out of 8 sources, see Fig. 2.6).

As discussed above, the density structure of the observed globules can be explained in terms of the slow collapse of a nearly critical Bonnor-Ebert sphere. The anticipated inward velocity from the model calculation remains subsonic[2] for a long time; the peak inward velocity is less

[2] In § 2.4.2, we have estimated distance to the globules using $T_{\rm eff}$ from radio molecular line observations as shown in Table 2.3. A collapsing motion in the globules should contribute to the derivation of $T_{\rm eff}$ if the motion is large enough compared with the observed molecular line width. Since predicted inward velocity from the model is small, it is likely that the contribution of collapsing motion to the derived distance is negligible.

than ~ 0.1 km s^{-1} for $\sim 10^6$ yr, which is $\sim 80\%$ of the total collapse time (see, Fig. 1 of Aikawa et al. 2004). Previous reports on the observations of CS ($J = 2 - 1$) (blue) asymmetry profile, indicative of gravitational collapse in dense cores, provided infall candidates in $\sim$10–20 % of the starless core samples (Lee, Myers, & Tafalla 1999, 2001; Lee, Myers & Plume 2004). It is possible that the rest of the starless cores have a slow collapse motion which is hard to detect. Radio molecular line observations of infall asymmetry profiles with sufficiently high velocity resolution (e.g. $\sim$ 0.01 km s^{-1}) are necessary to confirm the scenario of slowly collapsing globules. Among the starless globules in Figure 2.6, the gas inward velocity for Lynds 694-2 ($\xi_{\rm max} = 25 \pm 3$) was measured as $0.05 - 0.07$ km s^{-1} (Lee, Myers, & Tafalla 2001; Lee, Myers & Plume 2004), which is consistent with the prediction from the collapse model ($\alpha = 1.1$).

2.6 Summary

We have carried out a near-infrared (J, H, and K_s) imaging survey of ten Bok globules using the infrared camera SIRIUS on the IRSF 1.4 m telescope in South Africa. A_V distributions for the ten globules were derived through measurements of the $H - K$ color excess or the stellar density at J, H, and K_s (star count). The radial column density profile for each globule was analyzed using the Bonnor-Ebert sphere model, which well fits the profile within observational uncertainties, and physical properties of globules, e.g., size, central density, temperature, mass, external pressure, and center-to-edge density contrast, were derived. The dimensionless radial parameter $\xi_{\rm max}$ determines the shape of a Bonnor-Ebert density profile as well as the stability of the equilibrium state, e.g., the solution of $\xi_{\rm max} > 6.5$ is unstable to the gravitational collapse. We investigated the stability of globules on the basis of $\xi_{\rm max}$ for ten globules from our observations and four globules in the literature. In addition to the near-infrared imaging, we have carried out radio molecular line observations toward the same ten Bok globules using the 25-element focal-plane SIS receiver BEARS on the 45 m telescope of Nobeyama Radio Observatory (NRO). We measured line width of the globules for independent measurements of the

"effective" temperature including the contribution of turbulence. It was confirmed that most of the globules are dominated by thermal support. Since the distance-dependent parameters of the Bonnor-Ebert sphere were derived using the initially assumed distance to the globules, derived best-fitting temperature was affected by the distance assumption. We constrained the distance to the globules by comparing the temperature from the molecular line width with the temperature from the Bonnor-Ebert fitting, and rescaled distance-dependent physical quantities of globules.

(1) We found that more than half of the starless globules (7 out of 11 sources) are located near the critical state, $\xi_{\rm max} = 6.5 \pm 2$. Thus, we suggest that a nearly critical Bonnor-Ebert sphere characterizes the typical density structure of starless globules, and it approximates the initial condition of gravitational collapse.

(2) We found that four out of eleven starless globules show clearly unstable states ($\xi_{\rm max} > 10$). Since unstable equilibrium states should not be long sustained, we expect that they are already collapsing toward higher central condensation or that extra force (e.g., magnetic and/or turbulent pressure) accounting for large $\xi_{\rm max}$ stabilizes the globules. It was also found that all three star-forming globules have unstable solutions of $\xi_{\rm max} > 10$, which is consistent with the fact that they have started gravitational collapse.

(3) We investigated the collapse of the Bonnor-Ebert sphere from a nearly critical state using the model calculation of Aikawa et al. (2004), and found that the column density profiles of the collapsing sphere mimic those of static Bonnor-Ebert spheres (unstable equilibrium solutions). By relating $\xi_{\rm max}$ to the collapsing sphere at a specific time, the evolutionary state of globules can be interpreted, and the detection probability of each $\xi_{\rm max}$ value can be predicted from the model calculation. Since the evolutionary timescale decreases with increasing density, the collapsing sphere resembles a marginally unstable Bonnor-Ebert sphere for a long time. It was found that the frequency distribution of $\xi_{\rm max}$ for the observed starless globules is consistent with that from model calculations of the collapsing sphere.

Acknowledgment

We are very grateful to M. Saito and K. Tomisaka for their helpful comments and suggestions. Thanks are due to the staff at SAAO and NRO for their kind support during the observations. The IRSF/SIRIUS project was initiated and supported by Nagoya University, National Astronomical Observatory of Japan, and University of Tokyo in collaboration with South African Astronomical Observatory under a financial support of Grant-in-Aid for Scientific Research on Priority Area (A) No. 10147207 and No. 10147214, and Grant-in-Aid No. 13573001 of the Ministry of Education, Culture, Sports, Science, and Technology of Japan. M. T. acknowledges support by the Grant-in-Aid (No. 12309010, 16340061, 16077204). Y. A. is supported by Grant-in-Aid for Scientific Research (No. 14740130, 16036205) and "The 21st Century COE Program of Origin and Evolution of Planetary Systems" of the Ministry of Education, Culture, Sports, Science and Technology of Japan (MEXT).

Appendix 2.A

Possible Systematic Uncertainties in $\xi_{\rm max}$

Here we discuss the ambiguity of derived column density (A_V), which leads to the systematic uncertainties in $\xi_{\rm max}$. In order to evaluate the dependence of the conversion factor, A_V/E_{H-K} and A_V/A_λ ($\lambda = J$, H, and K), on the ratio of total-to-selective extinction R_V, we used the R_V-dependent extinction law empirically derived by Cardelli et al. (1989). Though it is well established that R_V has a uniform value of ~3.1 in the ISM (e.g., Whittet 1992), there are some observational reports on higher R_V values up to $\sim$ 6 in dense molecular clouds (e.g., Kandori et al. 2003, and references therein). The empirical extinction law for $R_V = 6$ gives the conversion factors smaller $\sim$ 20 % than those for the case of $R_V = 3.1$, which we adopted in the analysis (§2.3.1 and §2.3.2). Note that the extinction law gives slightly different conversion

factors compared with Rieke & Lebofsky (1985) as shown in Table 3 of Cardelli et al. (1989). This possible systematic uncertainty as well as the uncertainty of the gas-to-dust ratio can be included in the derivation of $N(H_2)$. We have converted A_V to H_2 column density using the relationship $N(H_2)/A_V = 9.4 \times 10^{20}$ cm^{-2} mag^{-1} derived from Bohlin, Savage, & Drake (1978). Similar relationships were obtained from the X-ray absorption studies toward SNRs with high dynamic range ($A_V \lesssim 30$ mag) as $N_H/A_V = 1.8 - 2.2 \times 10^{21}$cm^{-2}mag^{-1} (Gorenstein 1975; Ryter et al. 1975; Ryter 1996; Predehl & Schmitt 1995). Thus, the conversion coefficient is likely to be determined within $\sim$ 20 % error. It can be seen from the panel (a) of Figure 2.8 that A_V is roughly correlated with about 1/2th power of density contrast for the Bonnor-Ebert spheres. Thus, for the case that A_V is systematically changed by a factor β, the value of density contrast varies by $\beta^{1.5}$ accordingly. Since ξ_{max} is proportional to $\sqrt{\rho_c}$, corresponding ξ_{max} value is expected to vary by $\beta^{0.75}$. If we assume that derived A_V for each globule is overestimated by 20 %, ξ_{max} is overestimated by $\sim$ 15 %. This is comparable to the uncertainty in ξ_{max} derived from the χ^2 fitting, and this modification should not significantly change our conclusions on the density structure of globules.

Table 2.1 Source list

Name	R.A. (J2000)[a] (^{h} ^{m} ^{s})	Dec. (J2000)[a] ($^\circ$ $'$ $''$)	Distance (pc)	IRAS[b]	Other name	Reference[c]
CB 87	17 25 05	−24 07 19	160	No	Barnard 74, Lynds 81	1,2
CB 110	18 05 55	−18 25 10	180	No	Lynds 307	1,3,4
CB 131	19 17 00	−18 01 52	180	No	Barnard 93, Lynds 328	1,3,4
CB 134	18 22 45	−01 42 40	260	No		1,5,A
CB 161	18 53 56	−07 26 29	400	No	Barnard 118, Lynds 509	1,6
CB 184	19 31 52	+16 27 14	300	No[d]	Lynds 709	1,3,4
CB 188	19 20 16	+11 36 15	300	Yes[e]	Lynds 673-1	1,3,4
FeSt 1-457	17 35 45	−25 33 11	160	No		1,3,4,B
Lynds 495	18 38 58	−06 44 00	200	No		1,7,C
Lynds 498	18 40 11	−06 40 45	200	No		1,7,C

[a]Position of field center for each near-infrared image.

[b]Existence of IRAS point sources within optical boundary of each core.

[c](1) Dutra & Bica (2002), (2) Huard, Sandell & Weintraub (1999), (3) Launhardt & Henning (1997), (4) Dame, Ungerechts, Cohen, De Geuss, Grenier, May, Murphy, Nyman, & Thaddeus (1987), (5) Straizys, Cernis, & Bartasiute (1996), (6) Leung, Kutner, & Mead (1982), (7) Schneider, & Elmegreen (1979), (A) Assumed to have the same distance as Serpens molecular cloud., (B) Assumed to have the same distance as Barnard 83., (C) Assumed to have the same distance as GF 5 dark cloud filament.

[d]IRAS 19116+1623 (Class II located near core boundary): Launhardt (1996)

[e]IRAS 19179+1129 (Class I with outflow): Launhardt (1996), Yun, & Clemens (1992)

Table 2.2 Results of stellar detection

Field	Limiting mag.[a]			Threshold mag.[b]			Detected number of stars[c]			
	J	H	K_s	J	H	K_s	J	H	K_s	H and K_s
CB 87	18.9	18.4	17.5	18.5	17.8	17.1	8107	10588	6510	7609
CB 110	18.8	17.9	17.1	18.1	17.2	16.4	12471	14220	12340	12119
CB 131	19.1	18.6	17.5	18.1	17.4	16.8	6678	10760	111868	9890
CB 134	19.5	19.2	17.9	18.9	18.5	17.5	5631	7530	4530	5510
CB 161	18.5	18.3	17.3	18.0	17.7	16.9	6431	8406	5330	6044
CB 184	18.8	18.1	17.3	18.3	17.8	17.1	5235	6056	4241	4673
CB 188	18.9	18.3	17.4	18.4	17.6	17.0	6743	8963	7372	7669
FeSt 1-457	19.0	18.2	17.4	18.6	17.2	16.8	9261	10614	10444	9240
Lynds 495	19.1	18.0	16.6	18.4	17.2	15.9	10764	13404	10510	10760
Lynds 498	18.7	17.6	16.7	17.7	16.8	16.0	13826	13696	12064	11673

[a]Limiting magnitude is defined by the magnitudes whose photometric error is equal to 0.1 mag.

[b]Threshold magnitude is defined by the peak value of the histogram distribution of magnitudes for detected stars whose magnitude errors are less than 0.1 mag.

[c]The first three columns show the number of stars detected on the J, H, or K_s images (single band detection) whose photometric error is less than threshold magnitudes. The last column shows the number of stars detected both on the H and K_s images whose photometric errors, $\sqrt{\delta H^2 + \delta K_S^2}$, are less than 0.15 mag.

Table 2.3 Molecular line parameters of globules

Name	$V_{\rm LSR}$ (km s^{-1})	ΔV[a] (km s^{-1})	$\Delta V_{\rm tot}$[b] (km s^{-1})	$\Delta V_{\rm NT}$[c] (km s^{-1})	$T_{\rm eff}$[d] (K)	τ[e]	$T_{\rm ex}$[f] (K)	Molecular Line
CB 87[g]	4.84±0.02	0.21±0.04	0.47±0.02	0.17±0.05	11.4±0.8	0.55±0.12	10	$C^{18}O$ ($J=1-0$)
	4.85±0.01	0.25±0.02	0.49±0.01	0.22±0.03	12.4±0.6	0.38±0.04	10	
CB 110	6.06±0.02	0.50±0.04	0.65±0.03	0.48±0.04	21.8±2.2	0.62±0.06	10	$C^{18}O$ ($J=1-0$)
	6.03±0.01	0.45±0.02	0.62±0.02	0.43±0.02	19.3±1.0	0.47±0.02	10	
CB 131	6.77±0.01	0.56±0.02	0.70±0.02	0.55±0.02	25.1±1.3	0.58±0.03	10	$C^{18}O$ ($J=1-0$)
	6.77±0.01	0.57±0.02	0.71±0.02	0.56±0.02	25.8±1.1	0.56±0.02	10	
CB 134	8.67±0.01	0.28±0.02	0.51±0.01	0.25±0.02	13.2±0.6	0.94±0.10	10	$C^{18}O$ ($J=1-0$)
	8.676±0.004	0.24±0.01	0.487±0.004	0.20±0.01	12.1±0.2	0.81±0.04	10	
CB 161	12.60±0.01	0.25±0.02	0.50±0.01	0.22±0.02	12.5±0.6	0.61±0.06	10	$C^{18}O$ ($J=1-0$)
	12.58±0.01	0.27±0.01	0.50±0.01	0.24±0.02	13.0±0.4	0.44±0.02	10	
CB 184	6.22±0.01	0.35±0.02	0.55±0.01	0.33±0.02	15.5±0.6	1.01±0.08	10	$C^{18}O$ ($J=1-0$)
	6.210±0.005	0.35±0.01	0.55±0.01	0.33±0.01	15.5±0.4	0.88±0.04	10	
CB 188	7.09±0.01	0.44±0.03	0.61±0.02	0.42±0.03	19.0±1.3	0.54±0.04	10	$C^{18}O$ ($J=1-0$)
	7.04±0.01	0.52±0.02	0.67±0.02	0.50±0.02	22.9±1.2	0.37±0.02	10	
FeSt 1-457	5.920±0.003	0.182±0.006	0.462±0.002	0.132±0.009	10.9±0.1	9.56±1.29	6.25±0.21	N_2H^+ ($J=1-0$)
	5.924±0.002	0.175±0.004	0.460±0.001	0.122±0.005	10.8±0.1	11.48±0.86	5.80±0.09	
Lynds 495	12.29±0.10	0.26±0.02	0.50±0.01	0.22±0.02	12.6±0.6	0.60±0.06	10	$C^{18}O$ ($J=1-0$)
	12.29±0.01	0.26±0.01	0.50±0.01	0.23±0.02	12.7±0.4	0.54±0.03	10	
Lynds 498	12.62±0.01	0.18±0.03	0.46±0.01	0.14±0.04	11.0±0.6	0.41±0.07	10	$C^{18}O$ ($J=1-0$)
	12.60±0.01	0.29±0.02	0.52±0.01	0.27±0.03	13.6±0.7	0.31±0.02	10	

[a] Observed FWHM line width.

[b] Total line width. We assumed thermal line width $\Delta V_{\rm T}$ is equal to 0.443 km s^{-1} ($T_{\rm k}=10$ K).

[c] Non-thermal line width.

[d] Temperature including non-thermal (turbulent) contribution ($T_{\rm eff}=T_{\rm k}+T_{\rm NT}$).

[e] Peak optical depth. The value for FeSt 1-457 is the sum of optical depths of the seven hyperfine components.

[f] We assumed the excitation temperature for the $C^{18}O$ spectra to be 10 K.

[g] The first row refers to the values from the spectrum towards the center of each globule, and the second row refers to the values from the composite spectrum of the central nine positions. The error represents 1σ error in the line profile fitting.

Table 2.4 Physical properties of globules I

Name	R.A. (J2000)[a] (^{h} ^{m} ^{s})	Dec. (J2000)[a] ($^\circ$ $'$ $''$)	θ_R ($''$)	ξ_{max}	n_c/n_{edge}[b]	A_V[c] (mag)	e[d]	P.A.[d] ($^\circ$)	r_{fit}[e] ($''$)	χ^2	Stability[f]	Reference[g]
CB 87	17 24 58.0	−24 06 45.0	87.5±2.6	5.1±0.4	8.1	6.6	0.52	120	<110	3.19	Stable	A
CB 110	18 05 55.0	−18 25 00.0	61.1±3.1	14.0±3.0	94.3	19.7	—	—	<70	1.17	Unstable	A
CB 131	18 17 00.0	−18 02 00.0	103±7.4	16.3±5.1	139	32.9	—	—	<150	3.22	Unstable	A
CB 134	18 22 46.0	−01 42 45.0	59.6±4.3	18.5±4.9	187	26.8	—	—	<55	0.44	Unstable	A
CB 161	18 53 56.0	−07 26 05.0	62.5±6.9	8.1±1.4	25.1	13.0	0.72	125	<50	0.11	Unstable	A
CB 184	19 13 52.5	+16 27 30.0	112±20	8.1±1.6	24.9	11.2	0.68	0	<75	0.15	Unstable	A
CB 188	19 20 15.0	+11 36 10.0	127±19	16.0±2.9	132	27.2	—	—	<100	5.17	Unstable	A
FeSt 1-457	17 35 47.0	−25 33 00.0	144±11	12.6±2.0	74.5	41.0	—	—	<140	1.41	Unstable	A
Lynds 495	18 38 58.0	−06 44 00.0	75.0±7.8	7.2±1.4	18.6	12.7	—	—	<65	0.14	Unstable	A
Lynds 498	18 40 11.0	−06 40 45.0	75.0±3.0	4.7±0.4	6.63	10.9	—	—	<70	0.84	Stable	A
Barnard 68	——	——	100	6.9±0.2	16.6	—	—	—	—	—	Unstable	B
Barnard 335	19 37 00.9	+07 34 10.0	125	12.5±2.6	73.1	—	—	—	<100	2.93	Unstable	C
Coalsack	12 31 38.6	−63 43 42.5	290	5.8	10.9	11.5	—	—	55−400	—	Stable	D
	——	——	140	7.0±0.3	17.2	23.0	—	—	—	—	Unstable	E
Lynds 694-2	19 41 04.4	+10 57 00.9	54	25±3	364	—	—	—	<83	1.12	Unstable	F

[a]Position of core center (centroid of A_V distribution).

[b]Center-to-edge density contrast determined from ξ_{max} value.

[c]A_V at core center.

[d]Fitted ellipticity and position angle.

[e]Profile fitting region in the Bonnor-Ebert fit.

[f]Stability of equilibrium state of the Bonnor-Ebert sphere.

[g] (A) This work, (B) Alves et al. (2001), (C) Harvey et al. (2001), (D) Lada et al. (2004), (E) Racca et al. (2002), (F) Harvey et al. (2003)

Table 2.5 Physical properties of globules II

Name	T^a (K)	D^b (pc)	R^c (AU)	$n_c{}^c$ (cm^{-3})	M^c ($M_\odot$)	$P_{ext}{}^c$ (K cm^{-3})	Reference[d]
CB87	6.0±0.4	160	$(1.40\pm0.04)\times10^4$	$(3.2\pm0.4)\times10^4$	0.76±0.07	$(2.9\pm0.4)\times10^4$	A
	11.4	304	$(2.66\pm0.08)\times10^4$	$(1.7\pm0.2)\times10^4$	2.73±0.24	$(2.9\pm0.4)\times10^4$	A
CB 110	7.0±0.4	180	$(1.10\pm0.06)\times10^4$	$(4.5\pm1.7)\times10^5$	0.74±0.17	$(4.0\pm0.9)\times10^4$	A
	21.8	561	$(3.43\pm0.18)\times10^4$	$(1.5\pm0.6)\times10^5$	7.21±1.64	$(4.0\pm0.9)\times10^4$	A
CB 131	14.0±0.8	180	$(1.85\pm0.13)\times10^4$	$(4.4\pm2.3)\times10^5$	2.43±0.73	$(5.3\pm1.5)\times10^4$	A
	25.1	323	$(3.32\pm0.24)\times10^4$	$(2.5\pm1.3)\times10^5$	7.83±2.35	$(5.3\pm1.5)\times10^4$	A
CB 134	13.0±0.8	260	$(1.55\pm0.11)\times10^4$	$(7.6\pm3.4)\times10^5$	1.85±0.50	$(6.3\pm1.7)\times10^4$	A
	13.2	264	$(1.57\pm0.11)\times10^4$	$(7.5\pm3.3)\times10^5$	1.91±0.52	$(6.3\pm1.7)\times10^4$	A
CB 161	14.0±1.1	400	$(2.50\pm0.28)\times10^4$	$(6.1\pm1.4)\times10^4$	3.51±0.90	$(4.0\pm1.5)\times10^4$	A
	12.5	357	$(2.23\pm0.25)\times10^4$	$(7.0\pm1.6)\times10^4$	2.79±0.72	$(4.0\pm1.5)\times10^4$	A
CB 184	14.0±1.0	300	$(3.35\pm0.61)\times10^4$	$(3.4\pm0.5)\times10^4$	4.70±1.76	$(2.2\pm1.6)\times10^4$	A
	15.5	332	$(3.71\pm0.67)\times10^4$	$(3.0\pm0.4)\times10^4$	5.76±2.17	$(2.2\pm1.6)\times10^4$	A
CB 188	18.0±1.1	300	$(3.80\pm0.57)\times10^4$	$(1.3\pm0.3)\times10^5$	6.45±2.05	$(2.1\pm1.1)\times10^4$	A
	19.0	317	$(4.01\pm0.60)\times10^4$	$(1.2\pm0.2)\times10^5$	7.19±2.28	$(2.1\pm1.1)\times10^4$	A
FeSt 1-457	24.0±1.7	160	$(2.30\pm0.18)\times10^4$	$(2.9\pm0.8)\times10^5$	5.41±1.13	$(1.1\pm0.3)\times10^5$	A
	10.9	73	$(1.04\pm0.08)\times10^4$	$(6.5\pm1.7)\times10^5$	1.12±0.23	$(1.1\pm0.3)\times10^5$	A
Lynds 495	8.0±0.7	200	$(1.50\pm0.16)\times10^4$	$(7.6\pm2.1)\times10^4$	1.19±0.31	$(3.9\pm1.4)\times10^4$	A
	12.6	315	$(2.36\pm0.25)\times10^4$	$(4.8\pm1.4)\times10^4$	2.95±0.77	$(3.9\pm1.4)\times10^4$	A
Lynds 498	11.0±0.9	200	$(1.50\pm0.06)\times10^4$	$(4.3\pm0.5)\times10^4$	1.42±0.16	$(8.5\pm1.7)\times10^4$	A
	11.0	200	$(1.50\pm0.06)\times10^4$	$(4.3\pm0.5)\times10^4$	1.42±0.16	$(8.5\pm1.7)\times10^4$	A
Barnard 68	16	125	1.25×10^4	——	2.10	1.8×10^5	B
	10±1.2	85	0.85×10^4	——	0.90	1.7×10^5	G
Barnard 335	——	250	3.125×10^4	3.0×10^4	14.0	——	C
Coalsack	19	150	4.35×10^4	1.8×10^4	6.1±0.5	——	D
	15	180	2.52×10^4	5.4×10^4	4.50	6.5×10^4	E
Lynds 694-2	——	250	1.35×10^4	3.1×10^5	3.00	1.1×10^5	F

[a] First row: value from the Bonnor-Ebert fit using assumed distance to the globules (see Table 1), Second row: value from molecular line observations (T_{eff}; see Table 3).

[b] First row: save value as listed in Table 1, Second row: calibrated value by using T_{eff} to scale the fitted Bonnor-Ebert model parameters.

[c] The values in the first and second rows are derived using the distances listed in the third column.

[d] (A) This work, (B)-(F) Same references as those in Table 4, (G) Hotzel et al. (2002).

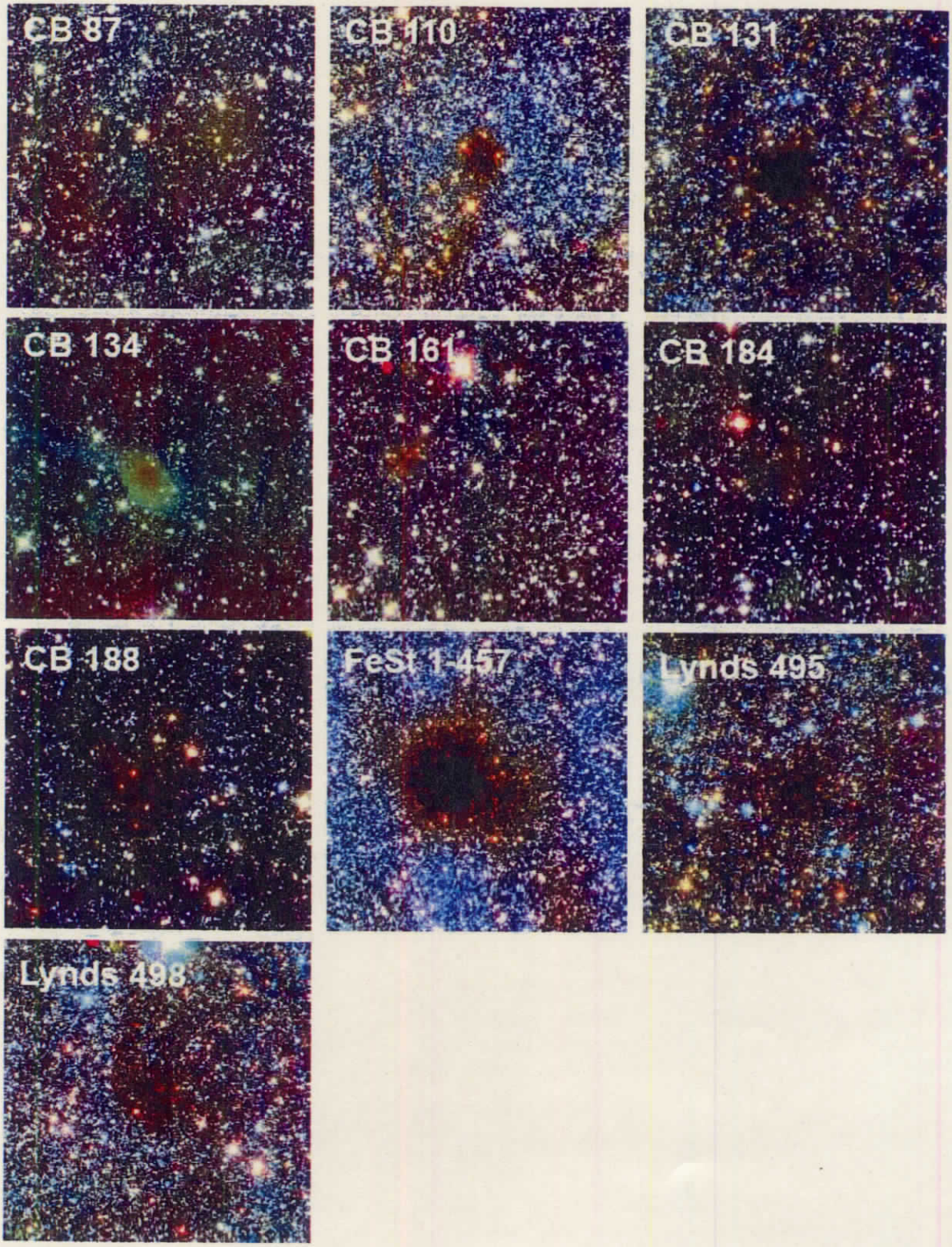

Figure 2.1 J, H, and K_s three-color composite images for ten Bok globules (J: blue, H: green, K_s: red). Each image size is 930×930 pixel (~7 arcminutes). North is up, and east is toward the left.

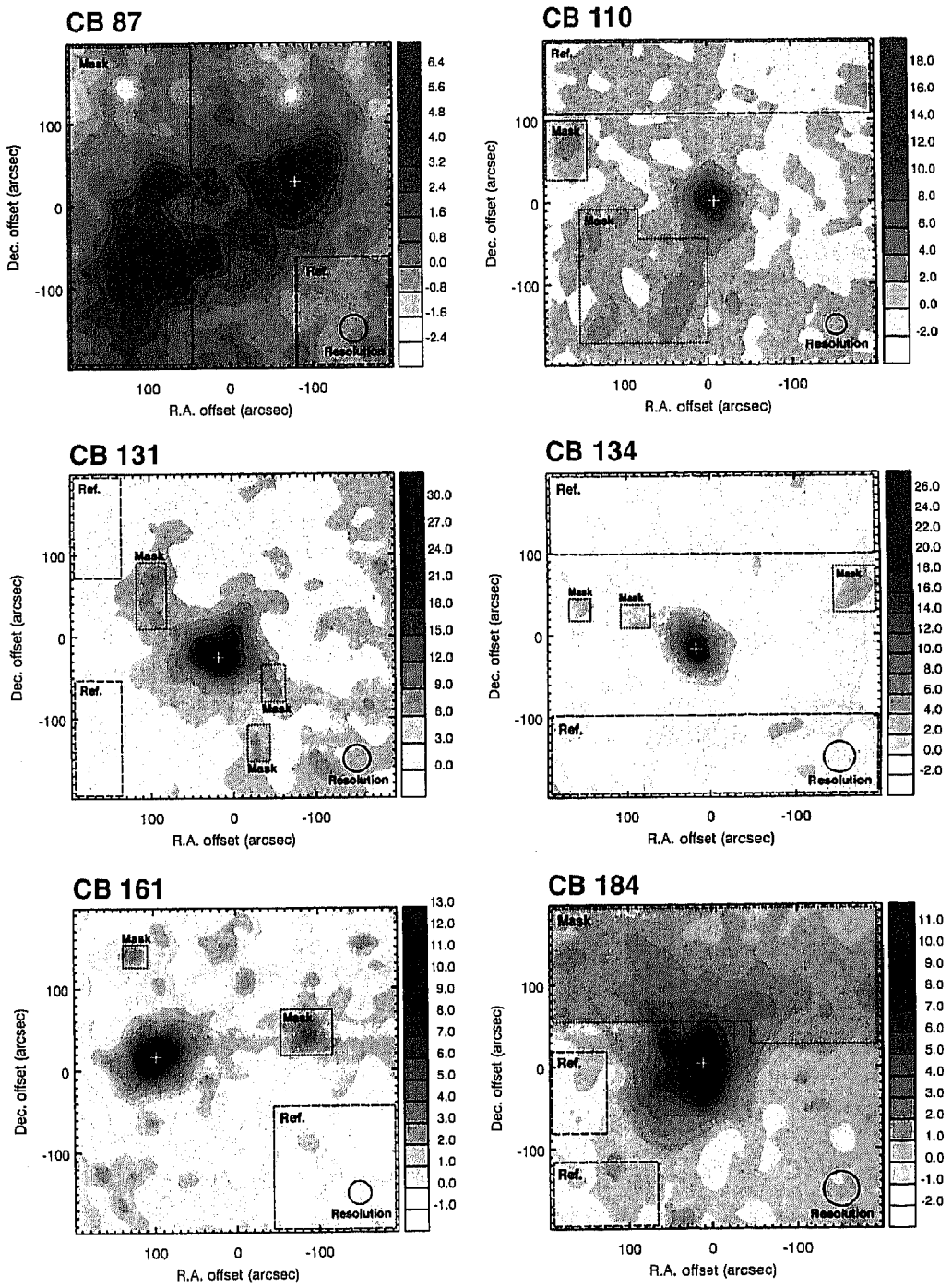

Figure 2.2 A_V distribution for Bok globules. The area enclosed by the broken line is the reference field expected to be free from dust extinction, and the area enclosed by the dotted line is the masked region which is excluded in the derivation of the radial A_V profile.

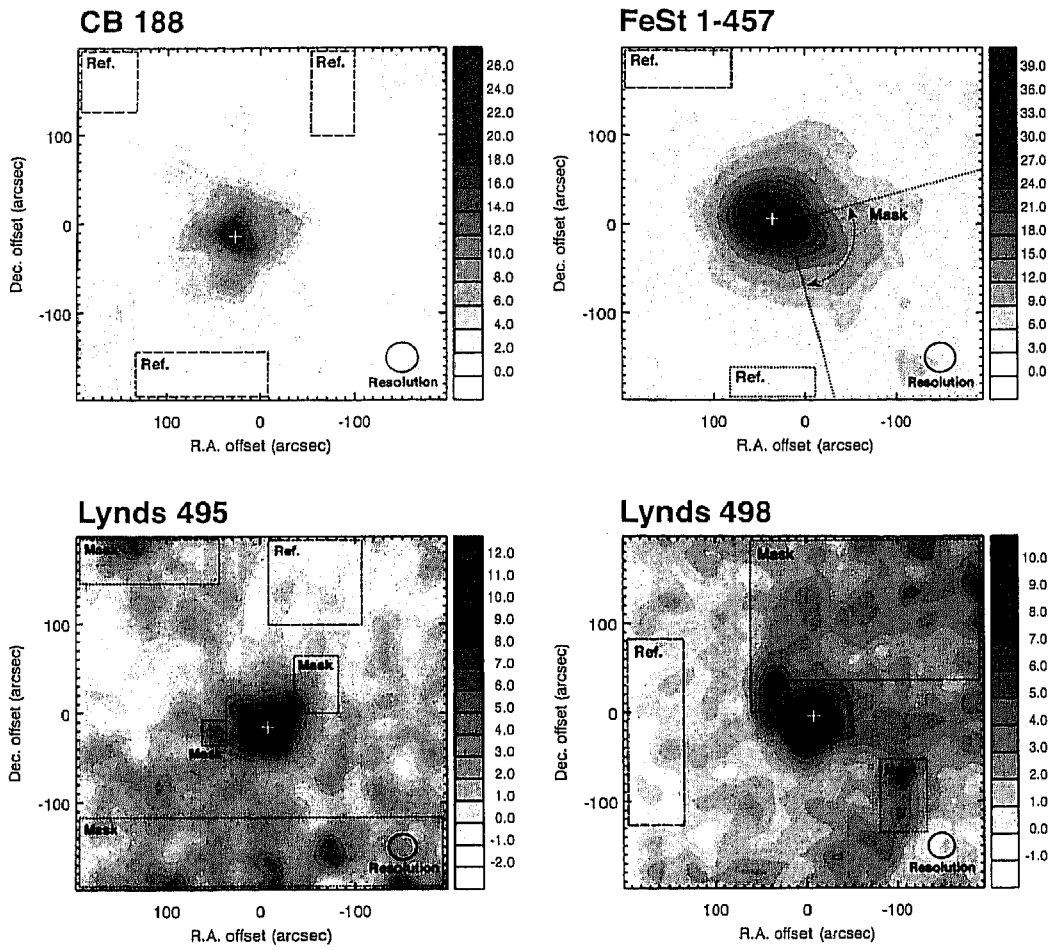

Figure 2.2 *continued.*

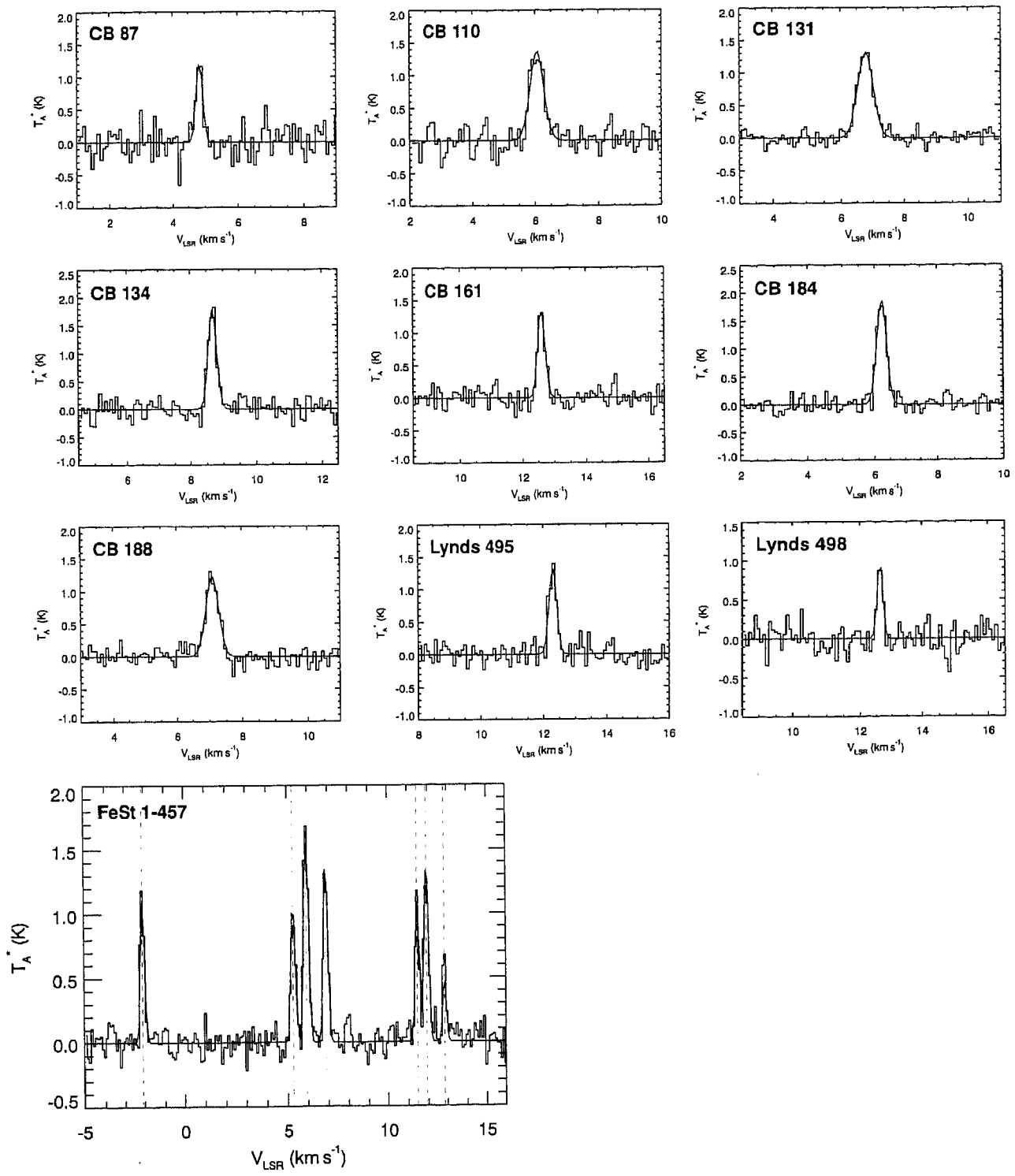

Figure 2.3 Line profiles toward the center of ten globules (N_2H^+ for FeSt 1-457, $C^{18}O$ for the other cores). The gray solid line denotes fitting result of each spectrum.

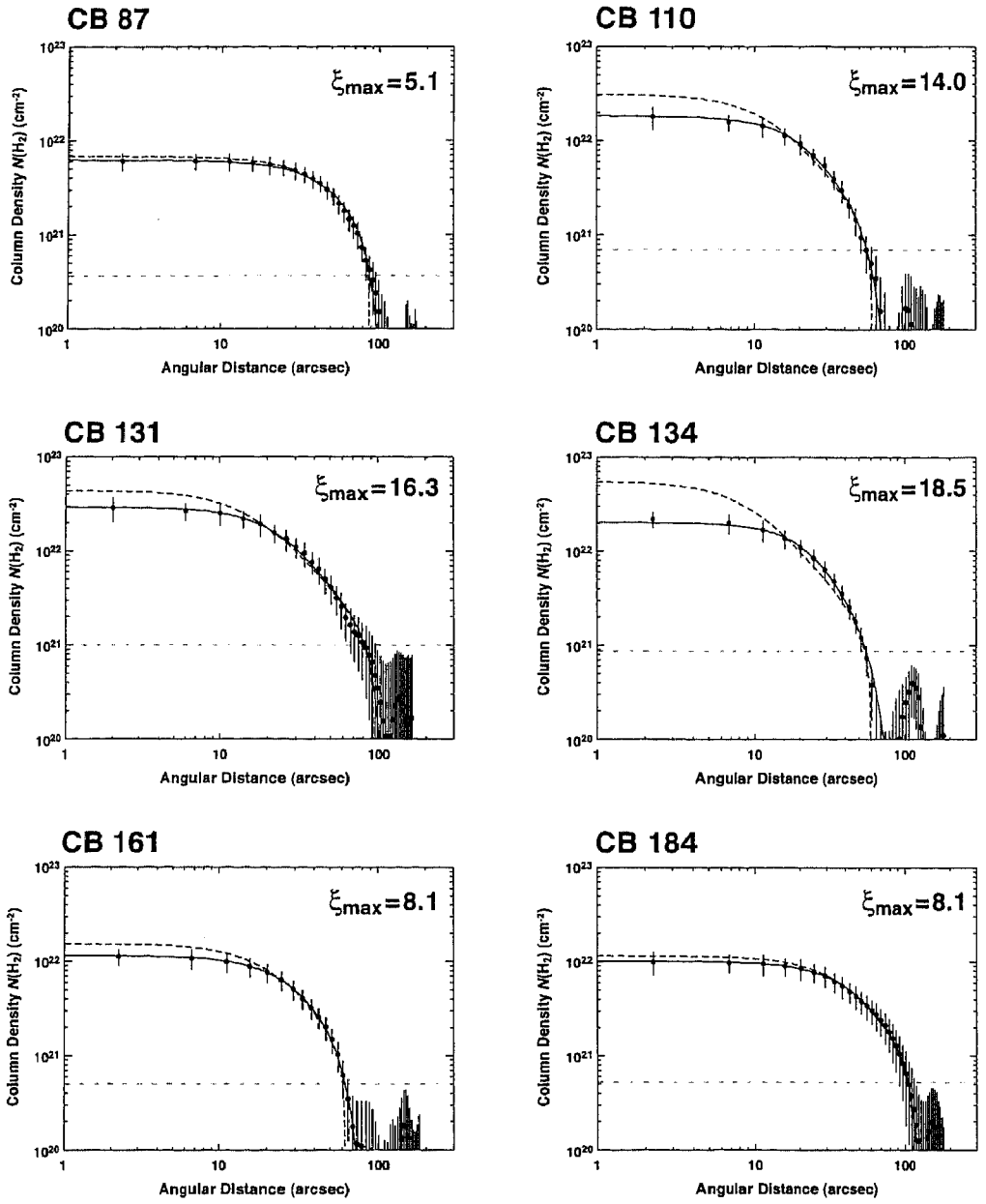

Figure 2.4 Radial column density profile and the Bonnor-Ebert model fit for the ten Bok globules. The dots and error bars represent the average $N(\mathrm{H_2})$ values at each annulus arranged at intervals of 9″ and the rms dispersion of data points in each annulus, respectively. The solid line denotes the best-fit Bonnor-Ebert profile which is convolved to the observing resolution (typically ~30″) with the same beam as used in the A_V measurements. The dashed line denotes the Bonnor-Ebert profile before the convolution. The gray dot-dashed line denotes the 1 σ deviation of the column density measured in the reference field.

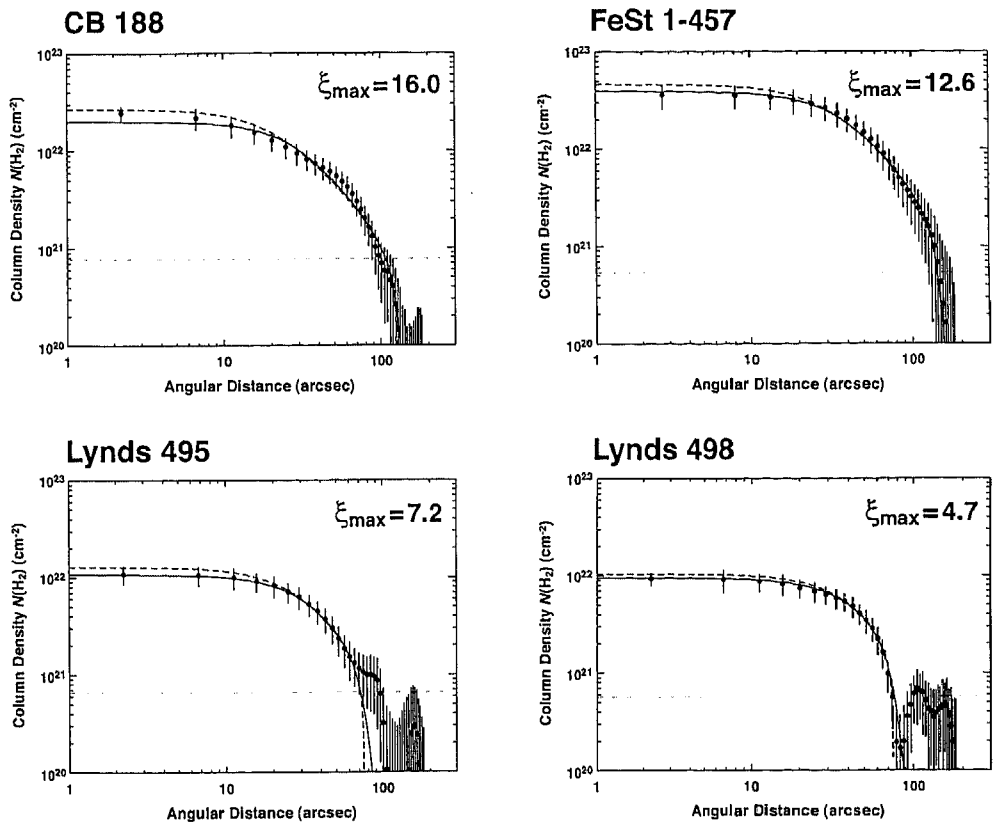

Figure 2.4 *continued.*

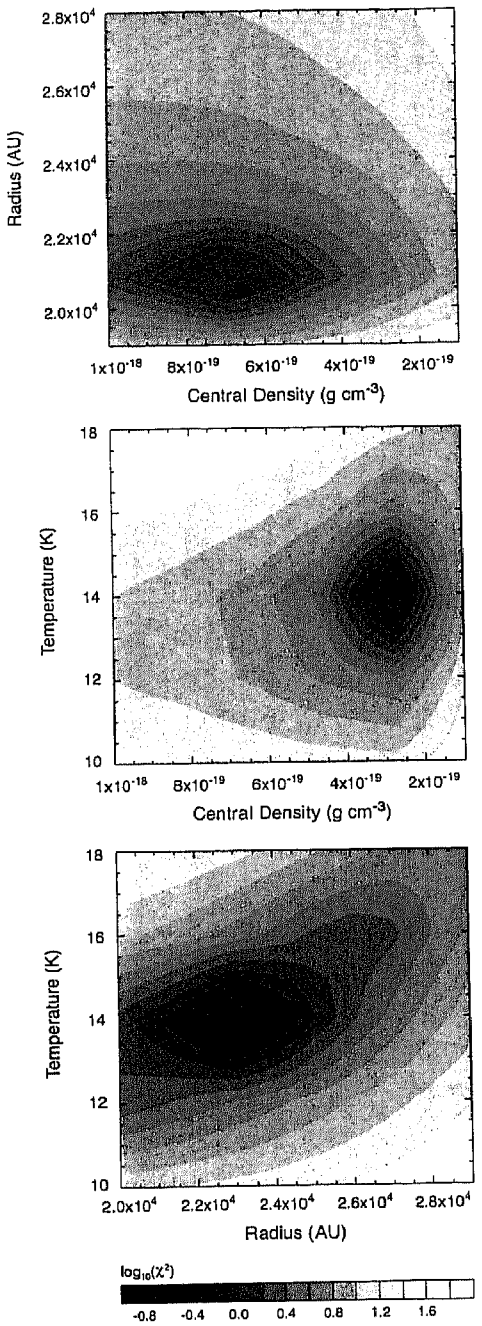

Figure 2.5 χ^2 distribution for CB 161. Upper, middle, and lower panels represent χ^2 distribution on the planes of $\rho_c - R$, $\rho_c - T$, and $R - T$, respectively.

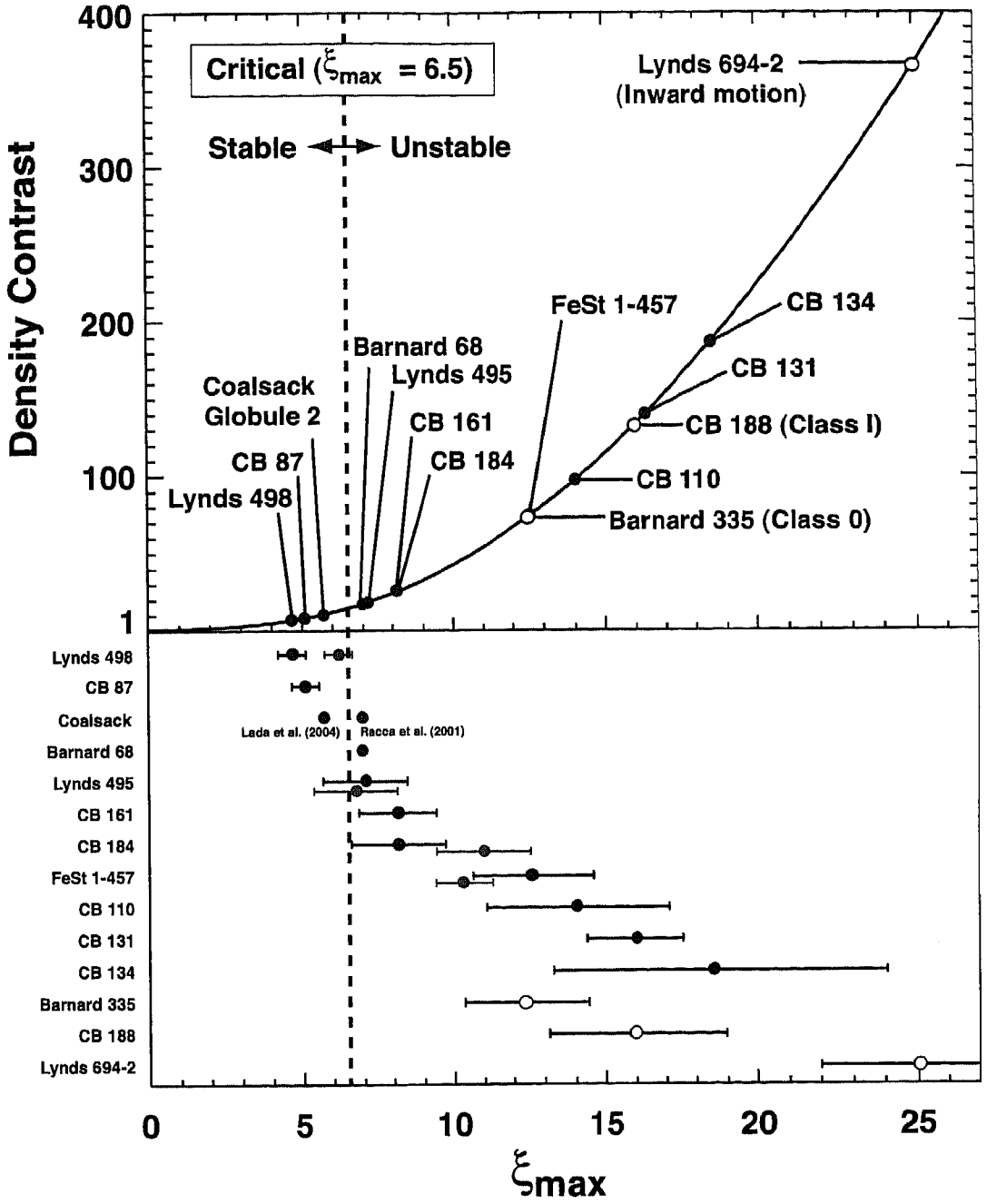

Figure 2.6 The solid line shows the relation between ξ_{max} and density contrast (center-to-edge density ratio). The location of our 10 globules and previously reported 4 globules (Barnard 335, Harvey et al. 2001; Barnard 68, Alves et al. 2001; Coalsack Globule II, Racca et al. 2002, Lada et al. 2004; Lynds 694-2, Harvey et al. 2003) are shown in the figure. Filled and open black circles denote starless and star-forming globules, respectively. Filled gray circles denote the fitting results when the masked region on the A_V map (see Fig. 2) is included in the derivation of the column density profile. The vertical dashed line denotes critical state of ξ_{max}= 6.5

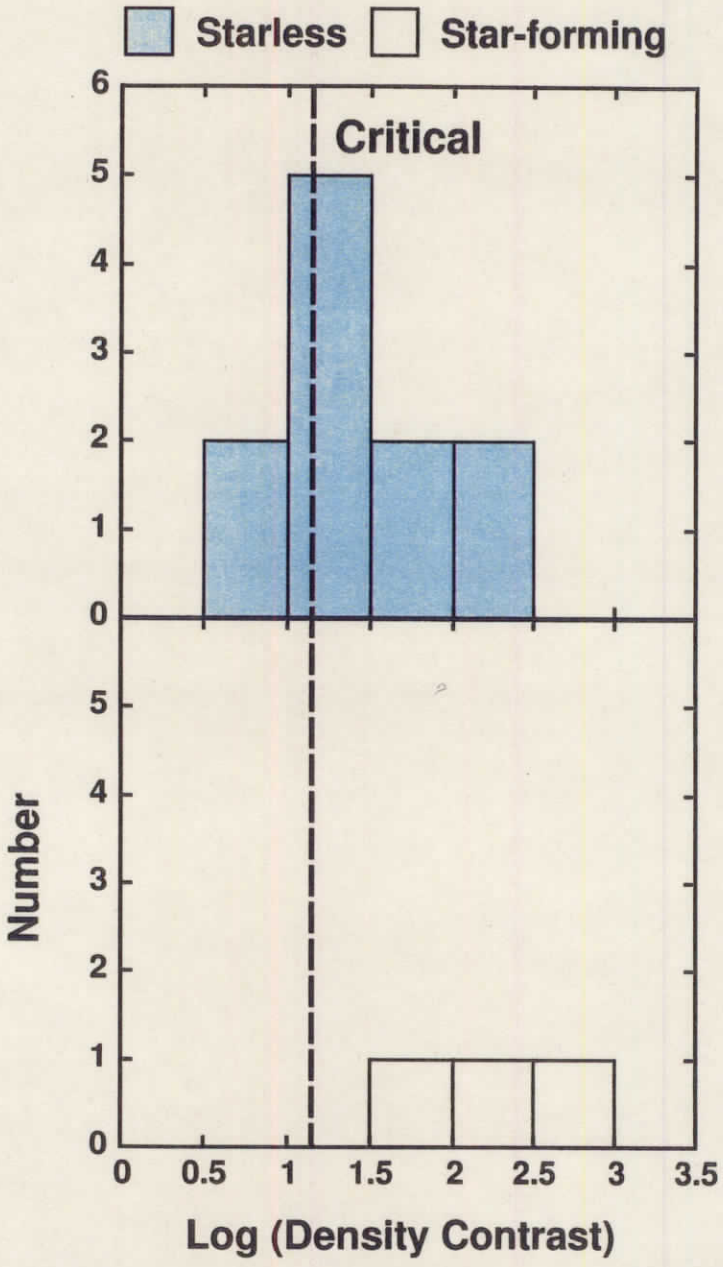

Figure 2.7 Histograms of logarithmic density contrast for starless and star-forming globules. The vertical broken line denotes the density contrast of the critical Bonnor-Ebert sphere.

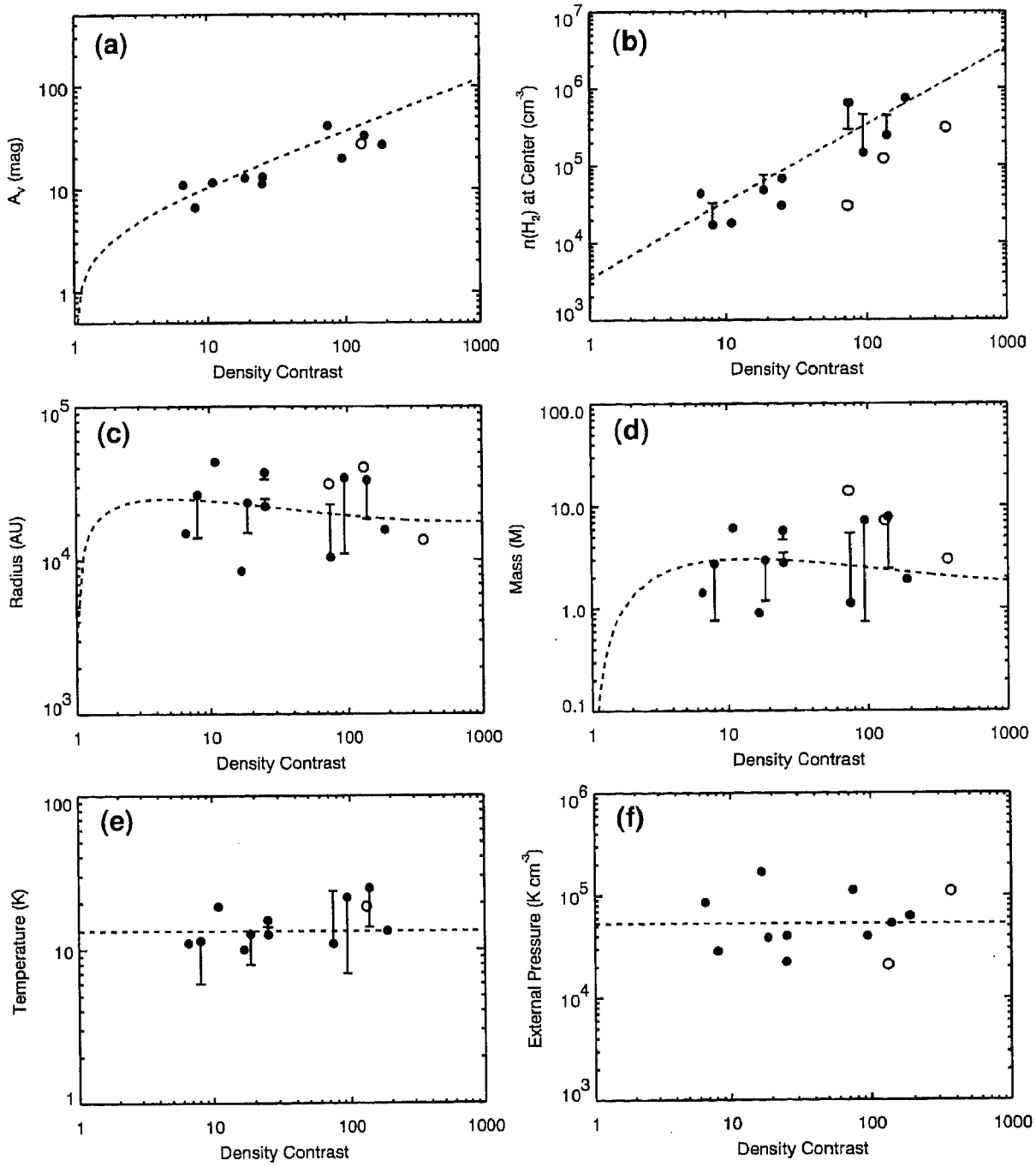

Figure 2.8 Correlations between density contrast and the other physical parameters. The panels of (a) to (f) show the correlation diagrams for A_V, central density, radius, mass, temperature, and external pressure, respectively. Filled and open circles denote starless and star-forming globules, respectively. The plotted data points are the physical quantities after distance-correction (see, §4.2.3, Table 5). The physical quantities without distance-correction are shown as the symbol "—" in each panel. The broken lines represent the relationships for the Bonnor-Ebert spheres with a constant temperature $T_{\rm eff}$ of 13.2 K and $P_{\rm ext}$ of 5.3×10^4 K cm^{-3}.

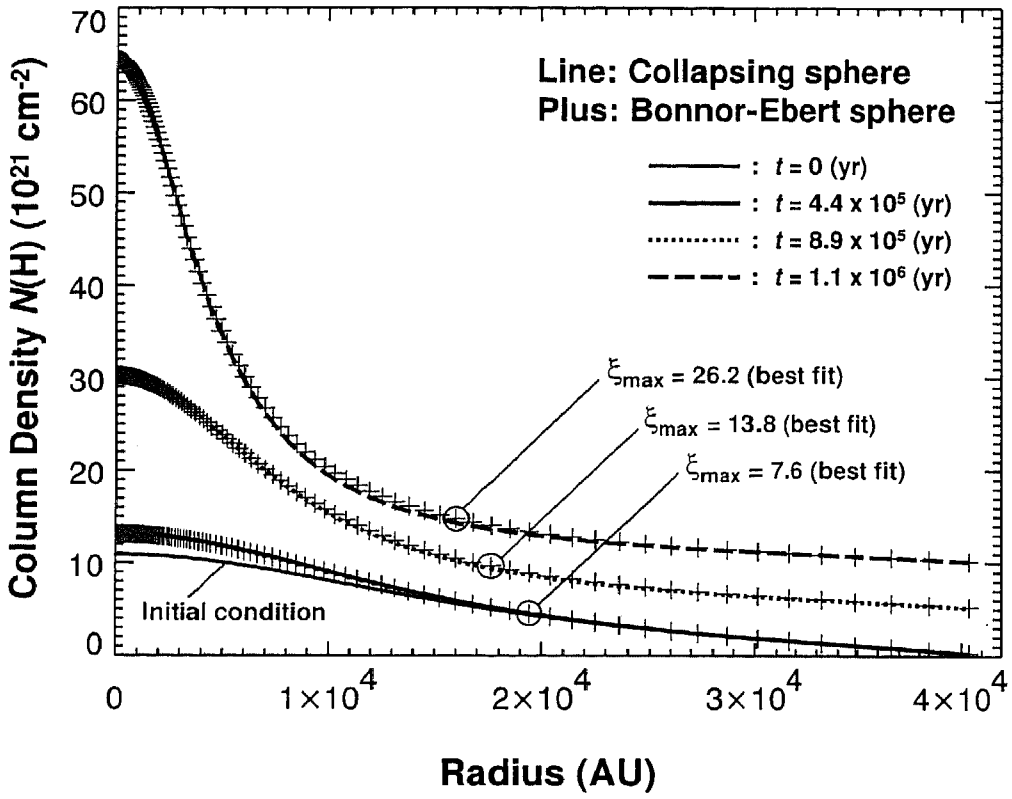

Figure 2.9 Radial column density distribution of a collapsing gas sphere at some specific times (black solid, dotted, and broken line) started from the initial condition of a nearly critical Bonnor-Ebert density structure (gray solid line). Dotted and broken lines are shifted by 5 and 10 (10^{21} cm^{-2}) in the figure, respectively. Best-fit solution of the Bonnor-Ebert sphere for each line is also plotted as plus symbol.

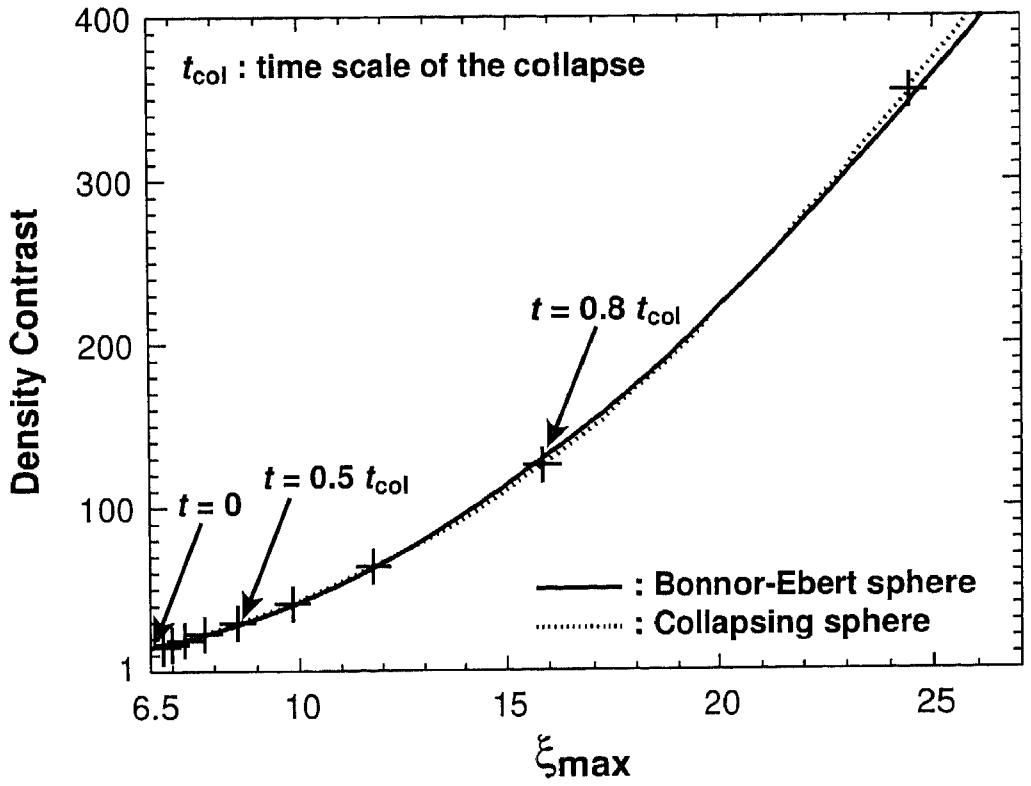

Figure 2.10 The solid line shows the relation between ξ_{max} and density contrast for the Bonnor-Ebert sphere (same as Fig. 6). The dotted line denotes the similar relation for a collapsing sphere starting from a nearly critical Bonnor-Ebert sphere ($\alpha = 1.1$ model; Aikawa et al. 2004); the column density profiles of the collapsing sphere were fitted with static Bonnor-Ebert sphere solutions, and the best-fit ξ_{max} values are plotted against the density contrast values of the collapsing sphere. The plus symbols denote the elapsed times from the onset of collapse at 10% intervals of the total collapse time (t_{col}).

Chapter 3

Grain Growth in the Dark Cloud L1251

Kandori, R., Dobashi, K., Uehara, H., Sato, F., & Yanagisawa, K., 2003, *The Astronomical Journal*, 126, 1888

Abstract

We have performed optical imaging observations of the dark cloud L1251 at multiple wavelengths, B, V, R, and I, using the 105 cm Schmidt telescope at the Kiso Observatory, Japan. The cloud has a cometary shape with a dense "head" showing star formation activity and a relatively diffuse "tail" without any signs of star formation. We derived extinction maps of A_B and A_V with a star count method, and also revealed the color excess (E_{B-V}, E_{V-R}, and E_{V-I}) distributions. On the basis of the color excess measurements we derived the distribution of the ratio of total to selective extinction R_V over the cloud using an empirical relation between R_V and A_λ/A_V reported by Cardelli et al. In the tail of the cloud, R_V has a uniform value of $\sim$3.2, close to that often found in the diffuse interstellar medium ($\sim$3.1), while higher values of R_V=4$-$6 are found in the dense head. Since R_V is closely related to the size of dust grains, the high R_V-values are most likely to represent the growth of dust grains in the dense star-forming head of the cloud.

3.1 Introduction

The ratio of total to selective extinction, $R_V = A_V/E_{B-V}$, is a measure of wavelength dependence of the interstellar extinction, representing the shape of the extinction curve. R_V is an important parameter to characterize dust properties at optical wavelengths because it is closely related to the size and composition of dust grains (e.g., Mathis, Rumpl, & Nordsieck 1977; Hong & Greenberg 1978; Kim, Martin, & Hendry 1994). It is well established that R_V has a uniform value of $\sim$3.1 in the diffuse interstellar medium (e.g., Whittet 1992), but it tends to be much higher in dense molecular clouds (R_V=4–6; e.g., Vrba, Coyne, & Tapia 1993; Strafella et al. 2001). Many theoretical predictions attribute the higher R_V in the dense cloud interior to a significant change of dust properties, particularly in size (e.g., Mathis 1990; Ossenkopf & Henning 1994). Since the timescale of grain growth due to coagulation of smaller grains and/or accretion of molecules in the gas phase onto the larger grain surface depends greatly on density (e.g., Tielens 1989), the higher R_V-values observed in dense molecular clouds are most likely to represent the growth of dust grains.

There have been a number of observational reports on R_V measurements to date (e.g., Larson et al. 2000; Whittet et al. 2001). However, they are mostly based on the spectrophotometry of a limited number of stars lying in the background of the clouds, and the R_V-values have been measured only toward the selected stars. A large-scale distribution of R_V over an entire cloud, as well as its local variation inside, are therefore still poorly known.

In order to investigate how much R_V can vary in a single cloud, we have carried out imaging observations of L1251 at multiple wavelengths, B, V, R, and I, using the 105 cm Schmidt telescope at the Kiso Observatory, Japan. This cloud is located in the Cepheus Flare ($\alpha\sim22^h35^m$, $\delta\sim75°00'$; J2000.0) and has an elongated shape. Since L1251 is an isolated dark cloud located at a relatively high Galactic latitude ($\sim$15°), it is expected that the cloud is free from contamination due to unrelated clouds in the same line of sight. Kun & Prusti (1993) estimated its distance to be 300±50 pc with a color excess measurement and spectral classification of stars.

They also found 12 H_α emission-line stars at the eastern part of the cloud, five of which are detected as *IRAS* point sources. Global molecular distribution of the cloud was first revealed by Sato & Fukui (1989) and Sato et al. (1994) through ^{13}CO and $C^{18}O$ (J=1−0) observations carried out with the 4 m radio telescope at the Nagoya University (HPBW=2.′7). Their observations clearly revealed the cometary "head-tail" morphology of L1251. They also found that two of the *IRAS* point sources located in the eastern "head" part of the cloud are associated with molecular outflows, while no sign of ongoing star formation was found in the western "tail." These characteristics of L1251 make this cloud a suitable site to investigate the possible difference in the dust properties (e.g., R_V) between star-forming and non-star-forming regions in a single cloud.

In this paper, we report results of the *BVRI* observations toward L1251. The observational procedures are described in § 3.2. The distribution of extinction (A_B and A_V) and color excess at each band (E_{B-V}, E_{V-R}, E_{V-I}) are derived from the obtained data, which reveal the global dust distribution of the cloud. These are shown in § 3.3 and 3.4. We also derive R_V distribution over the cloud on the basis of color excess measurements and an empirical relation between R_V and A_λ/A_V (Cardelli, Clayton, & Mathis 1989). A significant difference has been found in R_V distribution between the dense head and the relatively diffuse tail of the cloud, suggesting a larger dust size in the dense head than in the tail. We introduce our procedure to create R_V map and compare the obtained R_V distribution with the other data in § 3.5. Our conclusions are summarized in § 3.6.

3.2 Observations and Data Reduction

We carried out imaging observations of L1251 from 2000 November 27 to December 2 using the 105 cm Schmidt telescope equipped with the 2kCCD camera at the Kiso Observatory. The camera has a backside-illuminated 2048 × 2048 pixel chip covering a wide field of view of ∼50′×50′ with a scale of 1.″5 pixel^{-1} at the focal plane of the telescope. Using the camera,

we mapped L1251 with the B, V, R, and I filters at a 40′ grid spacing along the equatorial coordinates, so that adjacent frames could have an overlap of ∼10′ on the sky. We performed integrations of 200, 100, 100, and 50 s for the images obtained with the B, V, R, and I filters, respectively. The typical seeing was 3.″0−4.″5 during the observations. In total, we obtained 10 frames per filter, covering the entire extent of the cloud.

To calibrate the images, we obtained dome flat frames in the beginning of the observations and frequently obtained bias frames during the observations. In addition, we observed some sets of standard stars listed by Landolt (1992) to correct the atmospheric extinction and calibration.

We processed the calibrated images in a standard way using the IRAF packages.[1] After replacing values at the defected pixels in the detector (i.e., dead pixels) by those interpolated using surrounding pixels, we applied the stellar photometry package DAOPHOT (Stetson 1987) to the images to detect stars and then to make photometric measurements. To improve the photometry we further measured the instrumental magnitudes of the detected stars by fitting a point-spread function (PSF) and then calibrated them for the atmospheric extinction. Among all of the detected stars we selected the ones having an intensity greater than 4.0 σ noise level of the sky background. Some false detection, however, could not be completely ruled out, which we later removed by eye inspection. For calculating the plate solution, we compared the pixel coordinates of a number of the detected stars with the celestial coordinates of their counterparts in the Digitized Sky Survey (DSS), which resulted in a positional error of less than 1″ (rms). All of the stars detected in our observations were summarized separately with respect to the filters we used ($BVRI$), which we will adopt to generate an extinction map using a star count method. The limiting magnitudes are 20.0, 19.7, 19.0, and 18.3 mag for the B, V, R, and I bands, respectively. Among all of the identified stars ∼33,000 were detected in all of the four bands. These stars are useful for probing the distribution of the color excess in the cloud. We converted the instrumental magnitudes of these stars into the magnitudes in the

[1] IRAF is distributed by the National Astronomy Observatory, which is operated by the Association of Universities for Research in Astronomy, Inc., under coorperative agreement with the National Science Foundation.

standard Johnson-Cousins photometric system (Johnson & Morgan 1953; Cousins 1976), and we also measured their colors ($B-V$, $V-R$, and $V-I$). For the color excess measurements, we constructed a $BVRI$-matched star list for ~30,600 stars whose photometric errors in the color measurements, $\sigma_{V-\lambda}$, are less than 0.15 mag. One should note that we excluded all of the known young stellar objects (Sato & Fukui 1989; Sato et al.1994; Kun & Prusti 1993) cross-identified in our photometries in order to avoid errors in the following analyses since they are unrelated to the global extinction in L1251.

3.3 Distribution of Extinction

On the basis of the stars detected in the B and V band, we derived extinction (i.e., A_B and A_V) maps of L1251 using a star count method. Given a cumulative stellar density in the extinction-free reference field $N_{\rm ref}$ as a function of the λ-band magnitude m_λ (i.e., the Wolf diagram; Wolf 1923), a logarithmic cumulative stellar density $\log N$ measured at the threshold magnitude $m_{\lambda,0}$ can be converted into the extinction A_λ as

$$A_\lambda\left(l, b, m_{\lambda,0}\right) = m_{\lambda,0} - f^{-1}\left[\log N\left(l, b, m_{\lambda,0}\right)\right] \ , \tag{3.3.1}$$

where l and b are the Galactic coordinates, and f^{-1} is the inverse function of f defined as $\log\ N_{\rm ref} = f(m_\lambda)$. The function f is often assumed to be linear as $f = a + bm_\lambda$, where $b = [d \log N_{\rm ref}/dm_\lambda]_{m_\lambda = m_{\lambda,0}}$ (e.g., Dickman 1978).

To derive $N(l, b, m_{\lambda,0})$ in equation (3.3.1) from the obtained data, we first set circular cells with a $4'$ diameter spaced by $2'$ along the Galactic coordinates, and we counted the number of stars in the cells, setting the threshold magnitude to be $m_{B,0} = 19.5$ mag and $m_{V,0} = 19.2$ mag, which is well above the detection limit in our observations. We then smoothed the stellar density map to a $6'$ resolution with Gaussian filtering for a better signal-to-noise ratio to produce the final stellar density map $N(l, b, m_{\lambda,0})$, which we adopted to derive the A_B and A_V distribution.

After smoothing typical stellar density in the reference field and in the most opaque region was $\sim$20 cell^{-1} and $\sim$1 cell^{-1} for B band and $\sim$30 cell^{-1} and $\sim$2 cell^{-1} for V band, respectively.

We composed the stellar luminosity function $f_{\rm ref}(m_\lambda)$ in the reference field, i.e., the area expected to be free from extinction in the observed region (see Fig. 3.1). We found that the function is actually not linear, but has a curved shape. We also found that stellar densities at the threshold magnitude $m_{\lambda,0}$ systematically decrease along with the Galactic latitudes b. To deal with this problem, we fitted the average luminosity function $f_{\rm ref}(m_\lambda)$ by a 4th-order polynomial and scaled it to the background stellar density $N_{\rm back}$ at m_λ=$m_{\lambda,0}$ as

$$f\left(l,b,m_\lambda\right) = \frac{\log N_{\rm back}\left(l,b,m_{\lambda,0}\right)}{f_{\rm ref}\left(m_{\lambda,0}\right)} \sum_{n=1}^{4} c_n m_\lambda^n \quad , \tag{3.3.2}$$

where c_n represents the best-fitting coefficients. The value $f_{\rm ref}(m_{\lambda,0})$ corresponds to the mean stellar density at $m_{\lambda,0}$ in the reference field. We determined $N_{\rm back}(l,b,m_{\lambda,0})$ by assuming an exponential dependence on b as

$$N_{\rm back}\left(l,b,m_{\lambda,0}\right) = N_0 \exp\left(-\alpha\left|b\right|\right) \quad , \tag{3.3.3}$$

where N_0 and α are constants determined using values of $N(l,b,m_{\lambda,0})$ in the reference field. We obtained the coefficients (N_0, α) to be (61.5, 0.07) for B band and (106.2, 0.09) for V band.

We numerically calculated f^{-1}, the inverse function of f in equation (3.3.2), and used it in equation (3.3.1) to derive A_B and A_V after substituting the actually measured stellar density $N(l,b,m_{\lambda,0})$ into f^{-1}. The resulting A_V map is shown in Figure 3.1. The distribution of A_B (not shown) is very similar to that of A_V. Total uncertainty in A_λ varies from region to region, depending on the number of stars falling in the cells. Typical uncertainties in the reference field ($A_\lambda \sim 0$ mag) and in the most opaque region are estimated to be $\sim$0.5 and $\sim$0.8 mag for the B band, and $\sim$0.35 and $\sim$0.7 mag for the V band, respectively.

The A_V map reveals an interesting dust distribution in L1251 with a cometary head-tail

morphology, which is similar to the molecular distribution traced in ^{13}CO (Sato et al. 1994).

3.4 Distribution of Color Excess

We derived the color excess distribution in L1251 using the near-infrared color excess (NICE) method originally developed by Lada et al. (1994). The method compares the color index of stars in the reference field with those in the dark clouds. If we assume that the population of the stars across the observed field is invariable, the mean stellar color in the reference field can be used to approximate the mean intrinsic color of stars (i.e., $<V-\lambda>_{\rm int}=<V-\lambda>_{\rm ref}$), and the color excess can be derived by subtracting $<V-\lambda>_{\rm ref}$ from the observed color of stars. To obtain the color excess maps, we adopted an "adaptive grid" technique (Cambrésy 1998, 1999) to the ~30,600 stars detected in all of the four bands (B, V, R, and I). This technique consists in fixing the number of counted stars N per variable cell to achieve a uniform noise level in the resulting map. To estimate the mean color excess $<E_{V-\lambda}>$ (λ=B, R, or I) in circular cells spaced by 2′ along the Galactic coordinates with undefined sizes, we calculated the mean color of the closest N stars to the center positions of the cells by setting N to be 10 and derived their shifts from the mean color in the reference field $<V-\lambda>_{\rm ref}$ as

$$\langle E_{V-\lambda}\rangle\,(l,b) = \left[\sum_{i=1}^{N}\frac{(V-\lambda)_i}{N}\right](l,b) - \langle V-\lambda\rangle_{\rm ref}\ , \qquad (3.4.1)$$

where $(V-\lambda)_i$ is the color index of the ith star in a cell. The distance to the Nth star from the cell center gives the radius of the cell, corresponding to one half of the angular resolution. $<V-\lambda>_{\rm ref}$ is the mean color of the ~2000 cells in the reference field, and we determined $<B-V>_{\rm ref}$, $<V-R>_{\rm ref}$, and $<V-I>_{\rm ref}$ to be 1.02, 0.55, and 1.23 mag, respectively.

In the reference field, we found that $<V-\lambda>$ slightly but systematically decreases with increasing Galactic latitudes b. This may be caused by the presence of diffuse dust layer of the Galaxy and/or gradual change in the stellar population toward the Galactic plane. We

calibrated the effect by substituting $<V-\lambda>_{\rm ref}$ in equation (3.4.1) for the following equation assuming an exponential dependence on b as

$$\langle V - \lambda \rangle (l, b) = A \exp(-\alpha |b|) \quad , \tag{3.4.2}$$

where A and α are the fitting coefficients. We determined the coefficients (A, α) to be (1.60, 0.03), (2.60, 0.05), and (0.84, 0.03) for $<B-V>_{\rm ref}$, $<V-{\rm R}>_{\rm ref}$, and $<V-I>_{\rm ref}$, respectively.

We then smoothed the color excess maps with a Gaussian filter (FWHM=4′) to reduce noise. The resulting resolution of the maps is typically ∼5′ in the reference field and ∼10′ in the most opaque region. An example of the obtained color excess maps is shown in Figure 3.2, where we show the spatial distribution of E_{B-V}. The distributions of E_{V-R} and E_{V-I} (not shown) are similar to that of E_{B-V}. L1251 is also traced in the all-sky E_{B-V} map with 6′ resolution (Schlegel, Finkbeiner, & Davis 1998), which is derived from far-infrared emission data (*COBE/DIRBE*, *IRAS/ISSA*). The cloud appears similar in both the all-sky map and our color excess maps, indicating that the optical color excess and the far-infrared thermal emission of dust trace the same region.

Uncertainty in deriving $<E_{V-\lambda}>$ is given by following equation (e.g., Arce & Goodman 1999):

$$\sigma_{\langle E(V-\lambda)\rangle} = \left[\sigma_{\rm cell}^2 + \sum_{i=1}^{N} \left(\frac{\sigma_{(V-\lambda)_i}}{N}\right)^2\right]^{1/2} \tag{3.4.3}$$

where $\sigma_{(V-\lambda)_i}$ is the photometric error in $V-\lambda$ of the ith star in each cell. The value $\sigma_{\rm cell}$ is the standard deviation of the N-sampling distribution of the mean, where the original distribution is the $V-\lambda$ color of the stars in the reference field. It is equivalent to the standard deviation of the $<E_{V-\lambda}>$ distribution in the reference field. We estimated $\sigma_{\rm cell}$ to be 0.04, 0.03, and 0.05 mag for the color of $B-V$, $V-R$, and $V-I$, respectively. In the E_{B-V}, E_{V-R}, and E_{V-I} maps, a typical $\sigma_{<E_{V-\lambda}>}$-value calculated using equation (3.4.3) is 0.05, 0.03, and 0.05 mag,

respectively.

We derived the color excess diagram E_{B-V} versus E_{V-I} to see the global trend of reddening by dusts in L1251, which is shown in Figure 3.3. We investigated the relation separately in the star-forming head (l>114°.2) and in the non-star-forming tail ($l \leq 114°.2$). For comparison, we also show E_{B-V} versus E_{V-I} relations in the cases of R_V=3.1 and 6.5, adopting an empirical extinction law reported by Cardelli et al. (1989).

It is clear that there is a significant difference in the E_{B-V} versus E_{V-I} relations obtained in the two parts of the cloud. In the non-star-forming tail the data are distributed along the line of R_V=3.1, a typical value in the diffuse ISM, and the linear least-squares fit to the data actually yields a slope of E_{V-I}/E_{B-V}=1.21, which corresponds to R_V=3.2. On the other hand, the data in the star-forming head are distributed above the line of R_V=3.1 in the range of $E_{B-V} \geq 0.4$ mag, and they gradually get close to the line of R_V=6.5 for larger E_{B-V}. It is evident that optical properties of dust grains significantly vary even in a single cloud. The different extinction laws are well separated into two groups only when we divide them into star-forming and non-star-forming parts. Since R_V increases with increasing size of dust grains, larger R_V-value in the star-forming head is indicative of the evolution (i.e., growth in size) of dust grains. We note that E_{V-I} increases in the same way (along with $R_V \sim 3.1$) up to $E_{B-V} \sim 0.4$ mag both in the tail and in the head part, which indicates dust optical properties remain normal at the diffuse boundary of the cloud.

3.5 Derivation of R_V Distribution and Evidence for Grain Growth

In order to investigate the local variation of the dust properties in L1251, we derived the R_V distribution using a relationship between R_V and $E_{V-\lambda}/E_{B-V}$ that we produced from the R_V-dependent extinction law derived by Cardelli et al. (1989). They found that observed A_λ/A_V

versus R_V^{-1} relations toward a number of line-of-sight stars are well fitted over the wavelength range from 0.125 μm to 3.5 μm as

$$\langle A_\lambda / A_V \rangle = a(x) + b(x) R_V^{-1} \ , \tag{3.5.1}$$

where x is λ^{-1} μm^{-1}. The wavelength-dependent coefficients $a(x)$ and $b(x)$ are shown in equations (2a-2b) and (3a-3b) of Cardelli et al. (1989). By using equation (3.5.1) we reproduced R_V and $E_{V-\lambda}/E_{B-V}$ relations with the color excess ratios as $E_{V-\lambda}/E_{B-V}$=$(A_V$-$A_\lambda)/(A_B$-$A_V)$.

Color excess ratios of E_{V-R}/E_{B-V} and E_{V-I}/E_{B-V} are used to obtain the R_V-values at the cells that we used to derive the color excess maps. In each cell we numerically calculated the R_V-value, which minimizes the sum of residual variance; i.e., $[(E_{V-R}/E_{B-V})_{\rm obs}-(E_{V-R}/E_{B-V})_{\rm model}\}^2 + \{(E_{V-I}/E_{B-V})_{\rm obs}-(E_{V-I}/E_{B-V})_{\rm model}]^2$. We carried out the R_V fitting only in the region with $E_{B-V}\geq$0.4 mag in order to avoid a large error in R_V arising from too small E_{B-V} values. The resulting R_V map is shown in Figure 3.4. As seen in the figure, R_V in the star-forming head is systematically higher than in the tail with the maximum value of $R_V\sim$6. The mean value of R_V in the head and tail are $\sim$4.6 and $\sim$3.2, respectively. The feature in the R_V distribution is consistent with what we found in the color excess diagrams derived in the previous section (Fig. 3.3).

Uncertainties in the R_V measurement, σ_{R_V}, are estimated using Monte Carlo simulations. We first generated noise that follows a Gaussian distribution with the standard deviation equal to the 1 σ error of $E_{V-\lambda}/E_{B-V}$ measurements, and then we performed the R_V fitting to the noise-added $E_{V-\lambda}/E_{B-V}$ data. We repeated this calculation 1000 times in each cell, and regarded the standard deviation of the resulting R_V-values as σ_{R_V}. The value of σ_{R_V} varies from $\sim$0.5 to $\sim$0.9 (0.69 on the average) and tends to be relatively higher in cells with small E_{B-V}. In addition to the random noise our R_V map may suffer from a systematic error due to a number of unidentified pre-main-sequence (PMS) stars formed in the dense head. A certain fraction of PMS stars are known to have a blue color excess (e.g., Kenyon & Hartmann 1995),

which may result in an overestimate in R_V. However, this possible error should be negligible in our case, as we discuss in the Appendix.

We further checked the validity of the color-excess-based R_V measurements by using A_B and A_V derived with star count method. Though large uncertainties (typically $\sim$0.5 mag in our data) are included in A_B and A_V data, R_V can be directly computed as $R_V=A_V/(A_B - A_V)$ without using an empirical model. We made A_V versus A_B diagram for the same cells used in R_V measurements and separated them into the star-forming head (l>114.°2) and non-star-forming tail ($l\leq$114.°2). The slope of the A_V versus A_B relations yields mean R_V-value of data points as $<R_V>=1/(\alpha-1)$, where $\alpha=A_B/A_V$. The linear least-squares fit to each dataset resulted in $\alpha_{\rm head}$=1.23$\pm$0.09 and $\alpha_{\rm tail}$=1.34$\pm$0.07, which correspond to $<R_V>_{\rm head}\sim$4.3 and $<R_V>_{\rm tail}\sim$3.0, respectively. These values are consistent with the results of color-excess-based R_V measurements.

In Figure 3.4 it is particularly noteworthy that there is a good coincidence between the local peaks of the R_V distribution and the locations of YSOs. There are three strong R_V peaks in the head at (l,b)=(114.°60, 14.°47; R_V=6.1), (114.°50, 14.°67; R_V=5.8), and (114.°27, 14.°77; R_V=5.6). The first two peaks show a good agreement with the locations of the two outflow sources reported by Sato & Fukui (1989) and Sato et al. (1994), though the third peak has no apparent corresponding source. In addition, the three R_V peaks also coincide with the positions of molecular cloud cores found in $C^{18}O$ (named "B", "C", and "E" by Sato et al. 1994; see their Table 1 and Fig. 2), indicating that the region with high R_V-values is rich in molecular gas.

To investigate the dependence of R_V on the dust column density, we derived a diagram of A_V versus R_V. For a direct comparison we remeasured the A_V-values with the same cells used to produce the R_V map. In Figure 3.5 we show the diagram measured both in the dense head and in the diffuse tail. It is clear that the R_V increases along with A_V in the head, while that in the tail remains constant regardless of A_V.

All of the above results obtained from the comparison of the R_V map with the other data,

i.e., the coincidence of the R_V peaks and the outflow sources, as well as the $C^{18}O$ cores, and the difference in the A_V versus R_V relation between the head and the tail, strongly indicate that R_V is higher in the dense star-forming head than those in the diffuse tail without any signs of star formation. Because a higher value of R_V is expected for dusts with a larger size, the dusts in the head of L1251 may actually be larger than in the diffuse tail, indicating the growth of dust grains through coagulation and accretion of smaller dust particles as well as molecules in gas phase onto larger dust grains in the dense molecular cloud cores experiencing star formation. The R_V distribution derived in this study may not be sufficient to probe the densest region of L1251 (A_V>4−5 mag) in detail because of a large optical depth at the observed wavelengths. However, a similar change of dust properties most likely representing a large dust size in molecular clouds was recently reported through submillimeter observations of the dust emission (e.g., MCLD123.5+24.9: Bernard et al. 1999; Taurus: Stepnik et al. 2003). The idea of grain growth is also supported by their study based on the optically much thinner submillimeter observation, implying that dust grains with a larger size than in the diffuse ISM may be common in dense molecular clouds.

Our procedure to derive the R_V distribution on the basis of the average color excess measurements is useful to investigate a large-scale variation of the dust optical properties. It may be applicable also to the near infrared data in the future, with which we should be able to measure the R_V distribution in the densest region of L1251 to confirm the significant change of R_V therein.

3.6 Summary

We have carried out optical observations toward L1251 at multiple bands, B, V, R, and I, using the 105 cm Schmidt telescope equipped with the 2kCCD camera at the Kiso Observatory in Japan. Extinction and color excess maps of the cloud were derived using a star count method and a NICE method. From the observed $E_{V-\lambda}/E_{B-V}$ (λ=R,I), we also derived the

R_V distribution using an empirical R_V versus A_λ/A_V relation (Cardelli et al. 1989).

(1) We investigated the color excess distribution of the cloud on the basis of the ~30,600 stars detected in our observations. Color excess diagram, E_{B-V} versus E_{V-I}, indicates a significant difference in R_V between the star-forming dense head (l>114.°2) and the non-star-forming diffuse tail (l≤114.°2).

(2) We derived the R_V distribution over the cloud on the basis of the color excess measurements and an empirical relation between R_V and A_λ/A_V (Cardelli et al. 1989). From the resulting R_V map we found that R_V is systematically higher in the dense head (R_V=4−6) than in the diffuse tail (R_V~3.2), which is consistent with what we found in the E_{B-V} versus E_{V-I} diagram. We confirmed the validity of color-excess-based R_V measurements by comparing them with independently measured R_V-values; i.e., $A_V/(A_B-A_V)$, which were directly computed using A_B and A_V data from star count analysis.

Local peaks of the R_V distribution in the head of L1251 coincide with the positions of the young stars accompanied by molecular outflows and the molecular cloud cores identified in $C^{18}O$. We also found that R_V increases with increasing A_V in the dense star-forming head, while R_V is likely to be independent of A_V in the diffuse tail. Since R_V is closely related to the size of dusts, we suggest that these results are indicative of the growth of dust grains in the dense head due to coagulation and accretion of smaller dust particles and molecules onto the larger dust grains.

Acknowledgment

We are very grateful to M. Tamura, K. Tatematsu, and T. Mizuno for their helpful comments and suggestions. Thanks are due to the staff at Kiso Observatory including K. Nakada, T. Miyata, T. Soyano, K. Tarusawa, Y. Tanaka, H. Mito, T. Aoki, N. Ito, and S. Nishiura for their kind support during the observations. This work was financially supported by the Grant-in-Aid for Scientific Research by the Japanese Ministry of Education, Science, Sports and Culture

(Nos. 13640233 and 14022214).

Appendix 3.A

A Possible Systematic Uncertainty in R_V

Here we consider the degree of uncertainties caused by the presence of unknown faint PMS stars in the star-forming head of L1251, which escaped detection in the previous H_α survey (Kun & Prusti 1993). It is well known that a certain fraction of PMS stars show the optical blue excess, which is prominent in $U-B$ (e.g., Kenyon & Hartmann 1995) and possibly in $B-V$. Their blue intrinsic color should result in an underestimate of E_{B-V}, for which we may overestimate R_V.

In order to examine the fraction of blue excess PMS stars at $B-V$, we made a $B-V$ versus $V-I$ diagram of 96 PMS stars in the Taurus-Auriga region (see Table A1 of Kenyon & Hartmann 1995). We found 23 ($\sim$25%) sources show a blue excess of greater than 0.2 mag compared with the main-sequence stars, while the rest of the sources have a similar color to the main-sequence stars with some reddening.

If we assume that the ratio of the blue excess PMS stars measured in the Taurus-Auriga region is also valid in L1251, only two to three stars (25% of N=10) in each counting cell are expected to be blue excess PMS stars even in an extreme case that all of the stars detected in our observations are PMS stars. However, at the maximum estimate of the blue excess PMS stars (about two to three stars per cell), there might be an influence on the value of E_{B-V} calculated as the average color of 10 stars (eq. [3.4.1]). We therefore recalculated E_{B-V} taking the median color of 10 stars instead of the average, because it should be much less affected by a few blue excess PMS stars. We compared the two values of E_{B-V}, the median and the average colors of 10 stars, and found that they are quite consistent with each other even in the densest head of L1251 with a typical difference of only $\sim$0.02 mag. This means that the possible error in R_V due to the blue excess PMS stars is negligible, and the high R_V-value derived in the

star-forming dense head is most likely to be real.

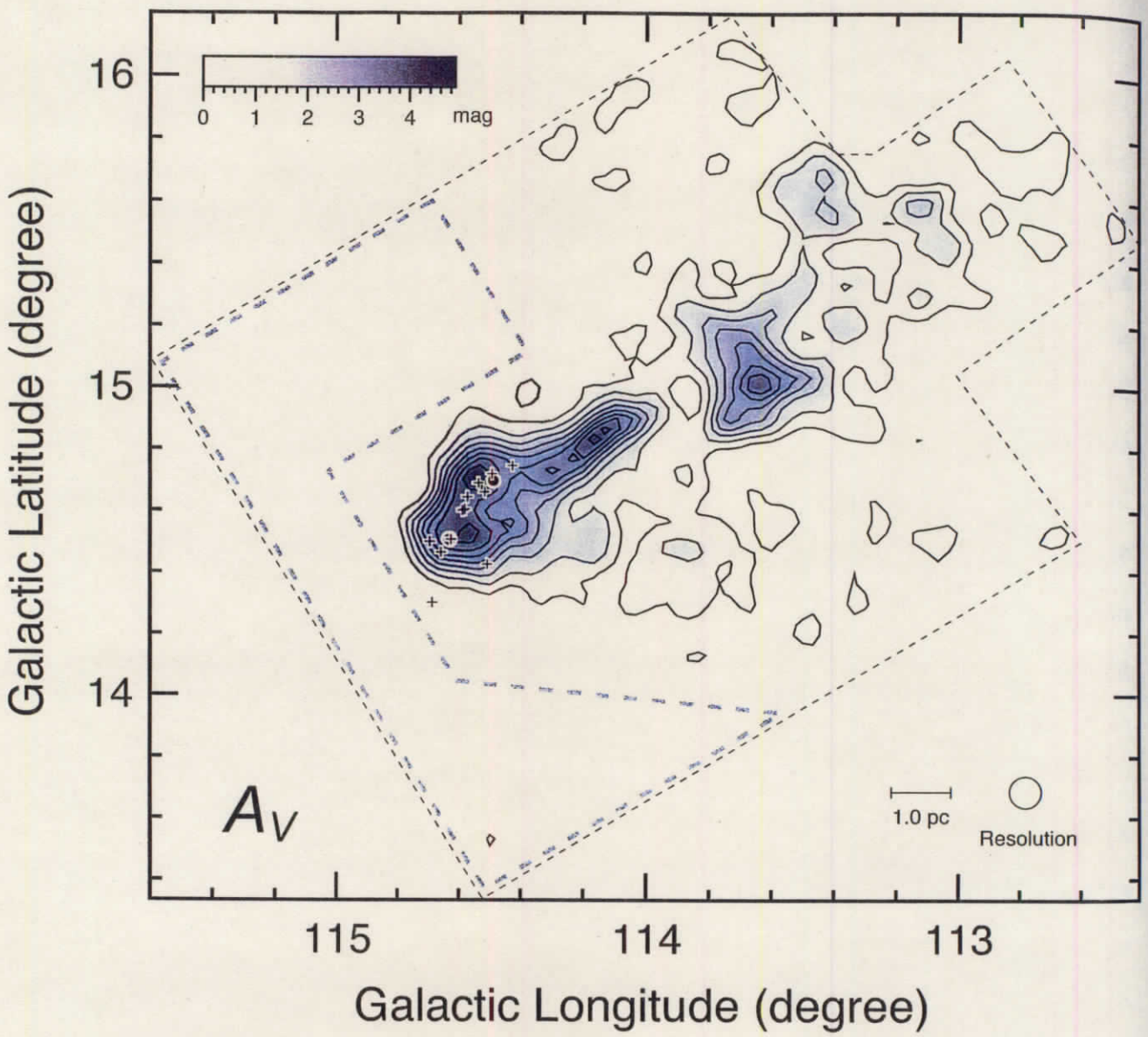

Figure 3.1 A_V distribution in L1251. The angular resolution is 6′. Contours start from 1 mag with a step of 0.5 mag. Filled circles with white outlines represent the positions of the *IRAS* sources associated with molecular outflows (Sato et al. 1994). Plus signs represent the positions of the H_α emission-line stars found by Kun & Prusti (1993). The observed area is delineated by the broken line. The area enclosed by the gray broken line is the reference field expected to be free from extinction. Typical uncertainties in A_V are ~0.35 mag and ~0.7 mag, which are found in the reference field (A_V~0 mag) and in the most opaque region (A_V~5 mag), respectively.

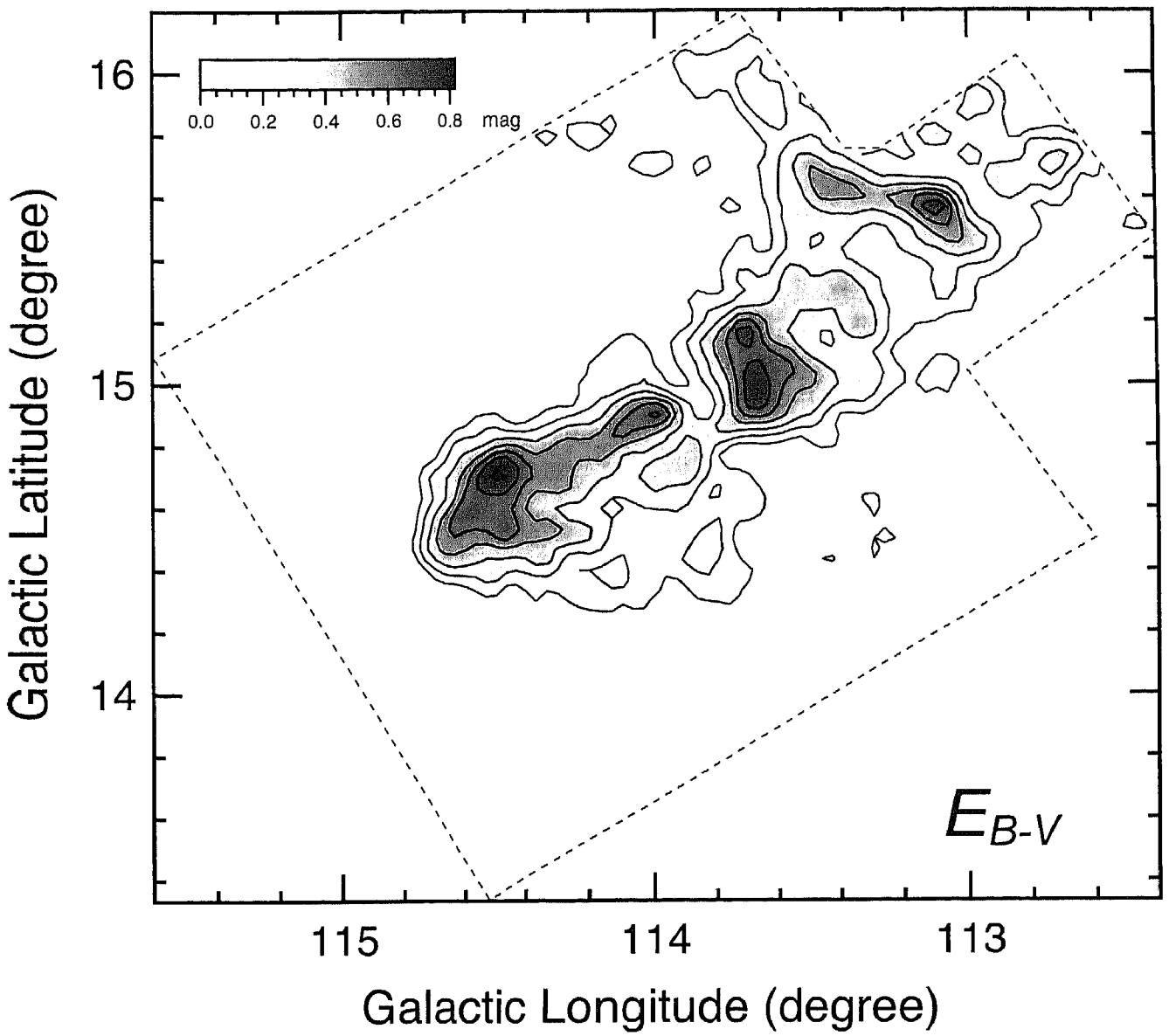

Figure 3.2 E_{B-V} distribution in L1251. Contours start from 0.2 mag with a step of 0.1 mag. The uncertainty in E_{B-V} is $\sim$0.05 mag. The highest and lowest angular resolutions achieved in the map are $\sim 5'$ in the reference field and $\sim 10'$ in the most opaque region, respectively.

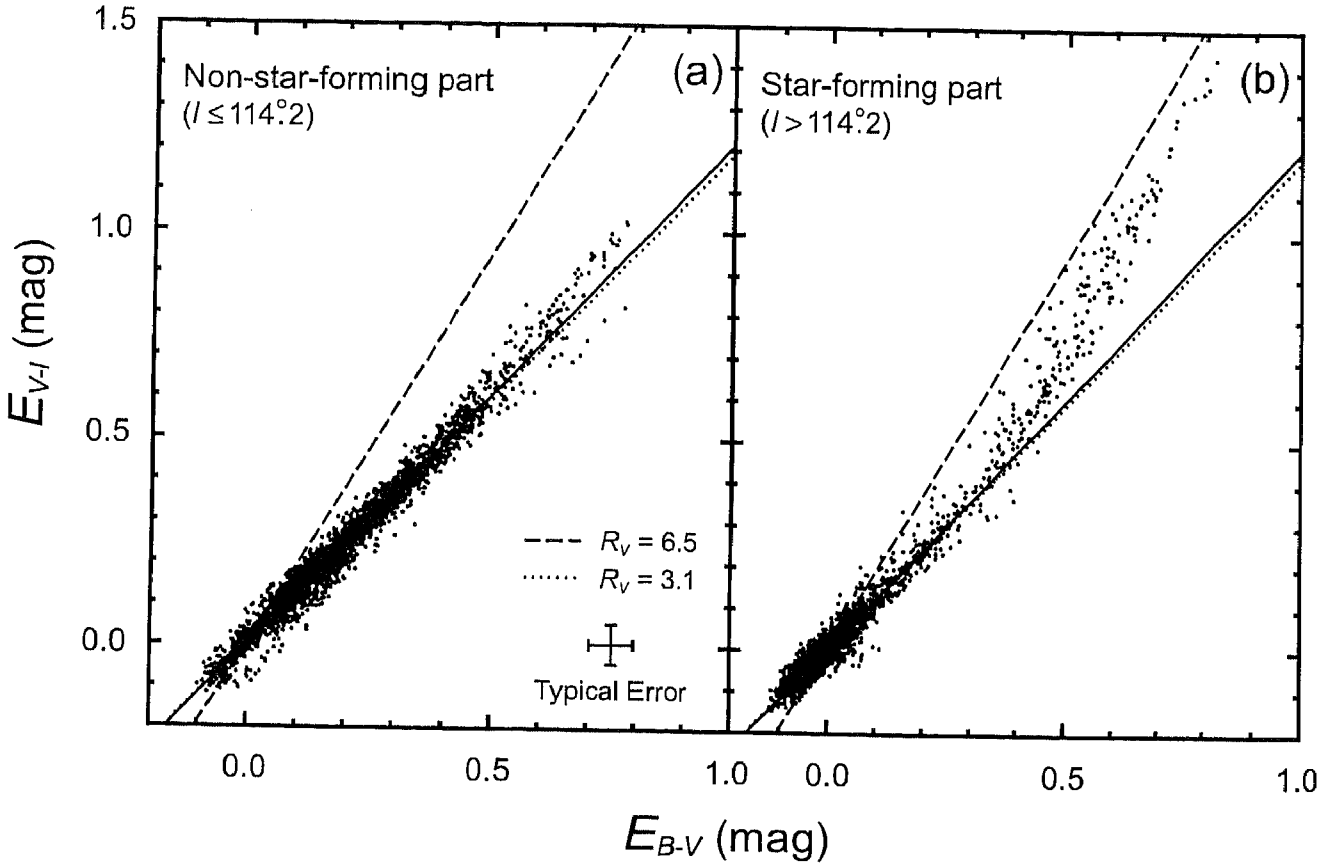

Figure 3.3 (a) E_{B-V} vs. E_{V-I} relation for the non-star-forming tail of L1251 ($l \leq 114.^{\circ}2$). The solid line denotes the linear least-squares fit ($E_{V-I}/E_{B-V}=1.21$ corresponding to $R_V=3.2$) to all of the data points in the tail. The dotted and broken lines are for the cases of $R_V=3.1$ and 6.5, respectively. The typical error in E_{B-V} and E_{V-I} is $\sim$0.05 mag. (b) Same as (a) but for the star-forming head of L1251 ($l > 114.^{\circ}2$).

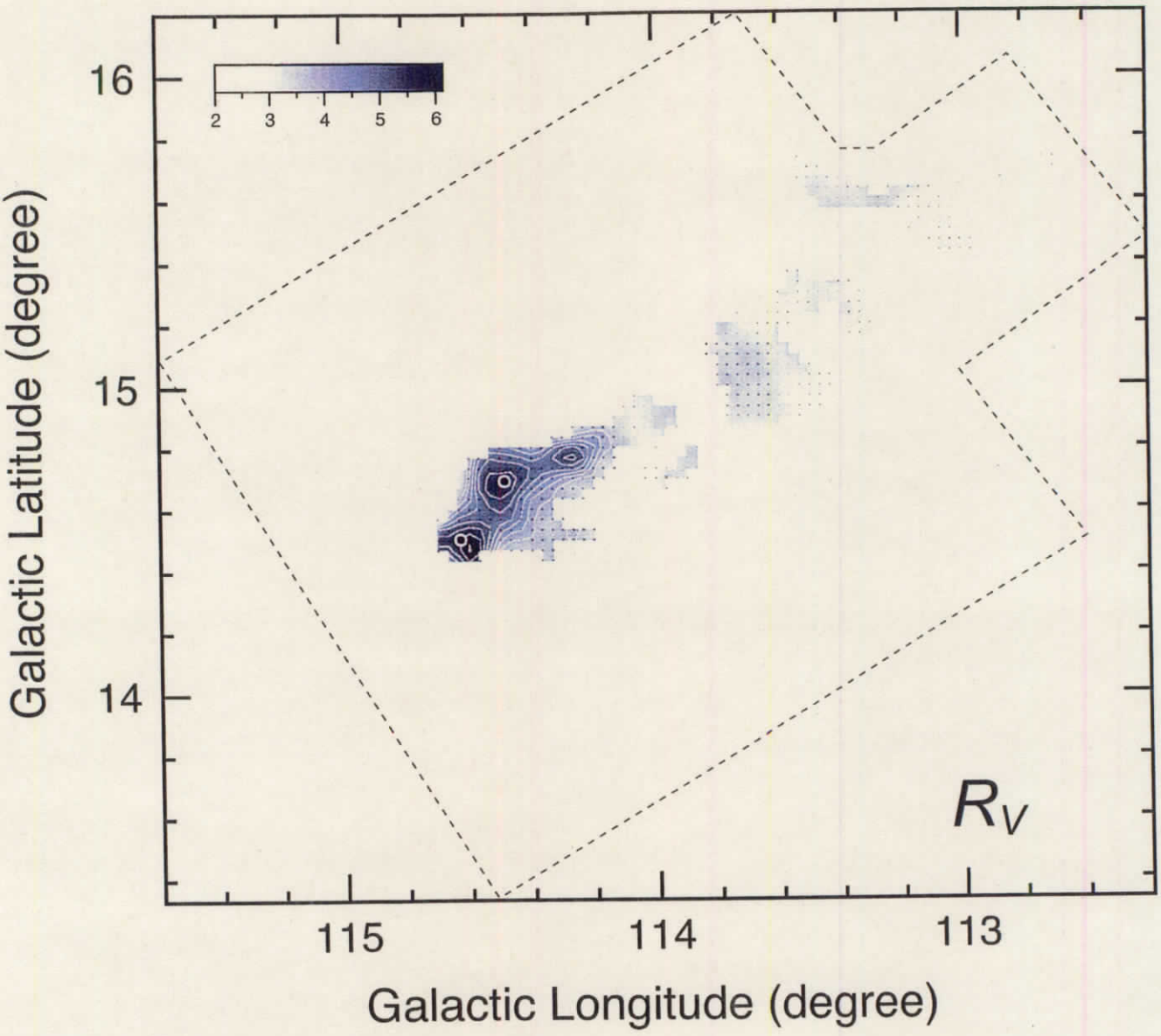

Figure 3.4 R_V distribution in L1251. The small dots represent the positions where we measured the R_V-values. Filled circles with white outlines denote the *IRAS* sources associated with molecular outflows (Sato & Fukui 1989; Sato et al. 1994). Contours start from R_V=4 with a step of 0.3.

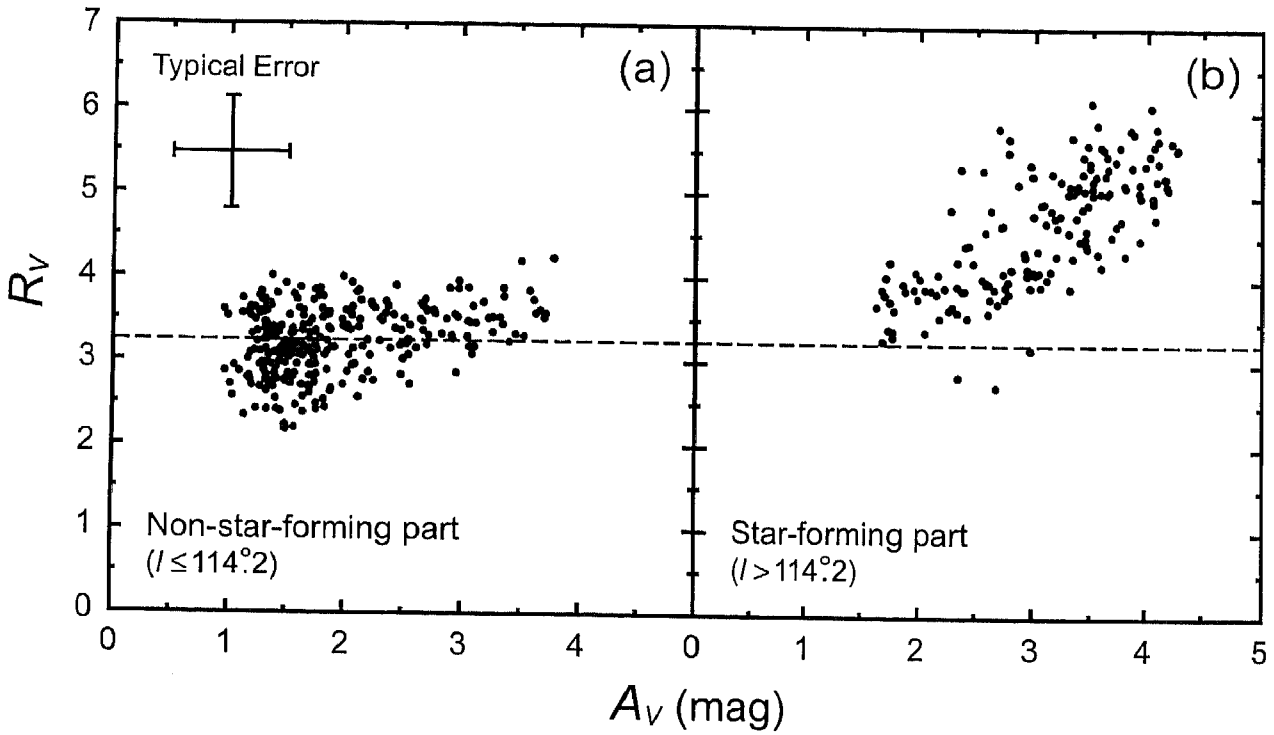

Figure 3.5 (a) A_V vs. R_V relation for the non-star-forming tail of L1251 ($l \leq 114.°2$). The broken line denotes the mean R_V-value 3.2. A typical error in A_V and R_V is 0.5 mag and 0.69, respectively. (b) Same as (a) but for the star-forming head of L1251 ($l > 114.°2$).

Chapter 4

Conclusion

The motivation of this study is to understand the low-mass star formation process through the measurements of density structure of globules (isolated dense cores) with and without YSOs (Chapter 2). Dust extinction at near-infrared wavelengths provides more reliable measure of column density than any other methods. On the basis of near-infrared imaging observations toward ten globules, I investigated their density structure using the Bonnor-Ebert sphere model. The Bonnor-Ebert model describes a pressure-confined self-gravitating isothermal gas sphere in hydrostatic equilibrium. A specific solution, i.e., the shape of density profile, of the Bonnor-Ebert model can be characterized by the non-dimensional radial parameter, $\xi_{\rm max}$, and/or density contrast (the ratio of central-to-surface density). The Bonnor-Ebert spheres with $\xi_{\rm max} > 6.5$ (density contrast > 14) correspond to the unstable equilibrium state, and are expected to be unstable against the gravitational collapse. Thus, the Bonnor-Ebert model fitting of globules provides the information on their stability as well as the shape of density structure. The Bonnor-Ebert model fitting studies of globules based on the near-infrared extinction have been reported for four sources as a case study. With the limited number of globules with well-defined density structure, statistical studies were impossible. By combining my ten globules with four globules in the literature (14 sources: three star-forming and eleven starless globules), I have performed the first systematic study of the density structure of globules on

the basis of near-infrared extinction measurements. Since the Bonnor-Ebert model can only be applicable to describe the "static" equilibrium conditions, I studied the evolution of the density structure of starless globules by comparing observations with a theoretical calculation of a collapsing gas sphere whose initial condition is close to the Bonnor-Ebert sphere. The main results of this study are summarized as follows.

(1) I found that more than half of the starless globules (7 out of 11 sources) are located near the critical state, $\xi_{\rm max} = 6.5 \pm 2$. Thus, I suggest that a nearly critical Bonnor-Ebert sphere characterizes the typical density structure of starless globules, and it approximates the initial condition of gravitational collapse. Most of globules appear to be thermally supported from radio molecular line observations.

(2) I found that four out of eleven starless globules show clearly unstable states ($\xi_{\rm max} > 10$). Since unstable equilibrium states are not long sustainable, I expect that these globules are already collapsing toward higher central condensation or that extra force (e.g., magnetic and/or turbulent pressure) accounting for large $\xi_{\rm max}$ stabilizes the globules. It was also found that all three star-forming globules have unstable solutions of $\xi_{\rm max} > 10$, which is consistent with the fact that they have started gravitational collapse.

(3) I investigated the collapse of the Bonnor-Ebert sphere from a nearly critical state using the model calculation of Aikawa et al. (2004), and found that the column density profiles of the collapsing sphere mimic those of static Bonnor-Ebert spheres (unstable equilibrium solutions). By relating $\xi_{\rm max}$ to the collapsing sphere at a specific time, the evolutionary state of globules can be interpreted, and the detection probability of each $\xi_{\rm max}$ value can be predicted from the model calculation. Since the evolutionary timescale decreases with increasing density, the collapsing sphere resembles a marginally unstable Bonnor-Ebert sphere for a long time. It was found that the frequency distribution of $\xi_{\rm max}$ for the observed starless globules is consistent with that from model calculations of the collapsing sphere.

Dust extinction observations at multiple wavelengths provide important information on dust grain properties in addition to the column density distribution of dark clouds. I studied dust

optical properties, i.e., the reddening/extinction law, in the dark cloud L1251 based on optical imaging observations at multiple wavelengths, B, V, R, and I (Chapter 3). The ratio of total to selective extinction, $R_V = A_V/E_{B-V}$, is a measure of wavelength dependence of dust extinction, representing the shape of the reddening/extinction curve. R_V is an important observational parameter, because it is closely related to the size and composition of dust grains. It is well known that R_V has a uniform value of ~ 3.1 for the diffuse interstelar medium, whereas much higher values, $R_V = 4 - 6$ were found toward some dense molecular clouds. Many theoretical studies attribute the higher R_V in dense clouds to the growth of dust grains through the coagulation of smaller grains and/or accretion of molecular gas onto the grain surface.

In the most of previous studies, R_V was measured toward a limited number of stars of known spectral type lying background to dark clouds. A large scale distribution of R_V over entire surface of the cloud, as well as its local variation inside the cloud, are still poorly known. On the basis of average color excess measurements, E_{B-V}, E_{V-R}, and E_{V-I}, I revealed spatial distributions of R_V in L1251 for the first time. L1251 has a cometary shape with a dense "head" showing star formation activity and a relatively diffuse "tail" without any signs of star formation. I investigated how much R_V can vary in L1251, and found that R_V is systematically higher in the star-forming dense head ($R_V = 4 - 6$) than in the starless diffuse tail ($R_V \sim 3.2$). It was also found that local peaks of the R_V distribution in the head of L1251 coincidate with the positions of YSOs accompanied by molecular outflows and the dense molecular clumps previously identified in $C^{18}O$ ($J = 1 \rightarrow 0$). Since R_V is closely related to the size of dust grains, I suggest that these results are indicative of grain growth in the star forming dense head of L1251. This is the first study to create R_V map of a dark cloud based on average color excess measurements at multiple optical wavelengths.

Appendix A

Development of Software for the Virtual Observatory Prototype in ALMA-Japan

Abstract

A virtual observatory (VO) is being developed in the Japanese group of the Atacama Large Millimeter/submillimeter Array (ALMA-Japan). I briefly introduce science requirements, present status, and future developments of the VO prototype in ALMA-Japan. The VO prototype system provides two kinds of data reduction pipelines that can reduce raw observational data taken with near-infrared and radio telescopes. I have developed a near-infrared data reduction pipeline as a module of the VO prototype. The pipeline engine has been implemented into the prototype.

A.1 Introduction

The Atacama Large Millimeter/submillimeter Array (ALMA) is an international project for a large millimeter and submillimeter aperture-synthesis telescope. ALMA will consist of 80

high-precision antennas, which are 64 antennas of 12 m diameter (64-element array) and the Atacama Compact Array system (ACA; 12 antennas of 7 m diameter and 4 antennas of 12 m diameter). These antennas will be installed in Chajnantor in Chile, at 5,000 meters above sea level. The construction and operation of ALMA are based on a collaboration among North America, Europe, and Japan. The Republic of Chile is the host country. ALMA will be a revolutionary ground-based telescope owing to its very high angular resolution and sensitivity at millimeter and submillimeter wavelengths, and will extend our understandings on wide variety of astronomical objects from the solar system to the distant galaxies.

The Japanese group of the Atacama Large Millimeter/submillimeter Array (ALMA-Japan) is developing a virtual observatory (VO), which can connect huge amount of ALMA data products with the data taken by other instruments at various wavelengths. This will be one of the most important functionalities provided by the ALMA Regional Center (ARC) in Japan as the science support service to the user. We assume that a pipeline processing of raw observational data is necessary to satisfy a variety of user interests. This is in contrast to most of the present astronomical databases that only manage reduced astronomical images and/or catalogs. It is also important that pipeline processed data of multiple wavelengths can be compared with each other (e.g., correlation analysis). We have determined science requirements and science cases for VO as shown in the next section. The VO prototype system in ALMA-Japan provides two kinds of data reduction pipelines developed using the RSI-IDL (Interactive Data Language, by Research Systems, Inc.) that can reduce raw observational data taken by the near-infrared[1] and radio[2] telescopes. The VO prototype was developed in order to evaluate system design and user interface. I have developed a near-infrared data reduction pipeline as a module of the VO prototype system. The pipeline engine has been implemented into the prototype. I note that the ALMA-Japan VO system is being developed in collaboration with Astronomical Data Analysis Center (ADAC), National Astronomical Observatory of Japan (NAOJ).

[1] IRSF 1.4 m infrared telescope in South Africa.
[2] NRO 45 m radio telescope in Japan.

A.2 Science Requirements

Science requirements for the ALMA-Japan VO system are as follows.

(1) Distributed Observational Database

Database of raw observational data should be accessible via the Internet. The distributed data processing is crucial, because the data contents must be supported and maintained by observatory staff who knows them best.

(2) Pipeline Processing of Raw Observational Data

Automated pipeline reduction of raw observational data should be available. The following files are neccessary as default output: reduced data (2D and/or 3D fits), JPEG images of reduced data for quick-look, log of the pipeline process including error messages, list of (default and/or optional) parameters used in the pipeline.

(3) Pipeline Processing with User Specified Parameters

In order to reflect scientific requirements from a user, the pipeline parameter list should be reusable. If a user is not satisfied with the default pipeline parameters, he/she can modify parameters in the list and can submit a request for the next pipeline run.

(4) Data Analysis Tools

In addition to the raw data processing pipelines, data analysis tools, such as source detection, photometry, and correlation between maps, are necessary to achieve specific scientific objectives. The effectiveness of database astronomy based on VO will highly depend on the functionalities of data analysis tools implemented in VO.

A.3 Science Cases

We have studied 16 science cases, and have selected three out of them as references for the current version of VO prototype.

(1) Physical Properties of Galaxies

To investigate relationship between morphology of galaxies (e.g., Hubble type) and molecular gas distribution by using the CO survey data taken by the Nobeyama Millimeter Array (NMA; an interferometer consists of six antennas of 10 m diameter) as well as optical and/or near-infrared images.

(2) Physical Properties of Molecular Clouds in the Inner Galaxy

To investigate relationship between the Galactic structure (e.g., with spiral arms) and physical properties of molecular clouds using the CO survey data taken with the NRO 45 m telescope.

(3) Physical Properties of Globules (Isolated Dense Cores)

To investigate relationship between molecular distribution and dust extinction toward globules using the molecular line data taken with the NRO 45 m telescope and the near-infrared images taken with IRSF 1.4 m telescope in South Africa.

A.4 ALMA-Japan VO Prototype System

A.4.1 Overview of the System Design

A schematic illustration of the ALMA-Japan VO prototype system is shown in Figure A.1. In the figure, each block labeled (a), (b), and (c) corresponds to the VO portal server, near-infrared data server[3] , and radio data server[4] , respectively. The servers (a) and (c) are located in NRO (Nobeyama), and the server (b) is located in the headquaters of NAOJ (Mitaka). The user accesses to the portal server via the Internet, and can submit queries using a Web-browser. The user authentication, query specification, and data transfer among the portal and data servers, are implemented by using the Globus Tool Kit (http://www.globus.org/). The VNC (Virtual Network Computing; http://www.realvnc.com/) is used for the display of pipeline process and results.

[3] IRSF 1.4 m telescope data are not opened to the public. We used our own data to develop the near-infrared pipeline server.

[4] NRO Data Archival System (nrodb; http://nrodb.nro.nao.ac.jp/)

A.4.2 Query and User Interface

When the user accesses to the VO prototype portal server via the Internet, VO main page will appear as shown in Figure A.2. The user are required to type one's login ID and password (Fig. A.2). After the user authentication, a pipeline specification page (Fig. A.3) willl appear, and the user can select either of near-infrared or radio data pipeline. The user can edit the parameter list by clicking the "edit" button in the second menu. The third menu specifies the process name, i.e., pipeline-ID. The pipeline results (reduced data, used parameter list, etc...) will be saved in the subdirectory, whose name is the same as the pipeline-ID, under the user directory in the VO portal server.

Next, a data search page for near-infrared or radio data will appeared. I show the image of data search page for the radio case in Figure A.4. The user can specify observation date, frequency, and object coordinates, and the search result will be returned as shown in Figure A.5. The user can select the check box of raw observational data, and can start pipeline process by clicking the "Run" button. Finally, the pipeline process status will appear (Fig. A.6). If the user click the "Launch Viewer" button, a new window is opened and the pipeline displays image data to be checked by the user.

A.4.3 Radio Data Pipeline

The radio data pipeline was developed by Sawada, T. (NAOJ) using the RSI-IDL, which deals with radio spectroscopy data taken by the NRO 45 m telescope equipped with the 25-element focal-plane array receiver BEARS (Sunada et al. 2000). The pipeline consists of the following procedures: (1) baseline subtraction, (2) flagging bad data, (3) combining the spectra at the same coordinates, (4) making 3D (R.A., Decl., velocity or frequency) data, and (5) creating maps of integrated intensity, peak temperature, and line width. The default parameters for these procedures are automatically determined. For example, a baseline subtraction is performed using the predetermined fitting range of channels in the spectrometers. The user can

change the parameters to be used by the pipeline by editing the default pipeline parameters. If the user sets the interactive baseline fitting option "yes", the user can interactively specify fitting ranges for baseline subtraction. The output data are: (1) 3D FITS, (2) 2D FITS and JPEG image of the integrated intensity, peak temperature, and linewidth map, (3) parameter list used by the pipeline, and (4) pipeline process log and error messages.

A.4.4 Near-infrared Data Pipeline

I have developed the near-infrared data pipeline using the RSI-IDL, which deals with near-infrared imaging data at J, H, and K_s taken with the IRSF 1.4 m telescope equipped with the SIRIUS camera (Nagayama et al. 2003; Nagashima et al. 1999). The pipeline consists of the following procedures: (1) dark subtraction and flat-field correction of object frames, (2) median sky subtraction from object frames, (3) frame registration, and (4) combining dithred object frames. The default parameters for these procedures are predetermined. The output data are: (1) FITS and JPEG images of the finally combined object frames, (2) three-color (Blue:J, Green:H, Red:K_s) composite JPEG image of the object frame, (3) parameter list used by the pipeline, and (4) pipeline process log and error messages. I show the three-color composite image of the dark globule FeSt 1-457 produced by the pipeline (Fig. A.7).

A.4.5 Data Analysis Tools

I have developed data analysis tools to deal with the near-infrared data from the near-infrared pipeline. The data analysis tools consist of the following procedures: (1) stellar detection at J, H, and K_s, (2) aperture photometry of detected stars, (3) making a list of coordinates, magnitudes, colors of stars, (4) generating an extinction (A_V) map of dark clouds based on the stellar color excess , in particular $H - K_s$, measurements. These analysis will be carried out if the user sets the data analysis option to "yes" in the parameter list of the near-infrared pipeline. The parameters for these procedures, e.g., threshold for the stellar detections, are

predetermined as default. The output data are: (1) a list of stellar coordinates, magnitudes, and colors, (2) an A_V map of the object in FITS and JPEG format, (3) a parameter list used by the pipeline, and (4) pipeline process log and error messages. I show the A_V map of the dark cloud FeSt 1-457 obtained by this analysis tool (Fig. A.8).

A.5 Summary

A virtual observatory (VO) prototype has been developed in the Japanese group of the Atacama Large Millimeter/submillimeter Array (ALMA-Japan). The system will be a key functionality to be provided by the ALMA Regional Center (ARC) in Japan as the science support service to the user. The VO prototype system consists of two kinds of data reduction pipelines that can reduce raw observational data of both near-infrared and radio telescopes. I have developed and implemented a near-infrared data reduction pipeline as a module of the VO prototype. In addition to the raw near-infrared data reduction, the pipeline can analyze reduced images to measure the extinction (A_V) distribution through the stellar detection and photometries. The ALMA-Japan VO system is being developed in collaboration with Astronomical Data Analysis Center (ADAC), National Astronomical Observatory of Japan (NAOJ).

Acknowledgements

This work was supported by the JSPS Core-to-Core Program. The IRSF/SIRIUS project was initiated and supported by Nagoya University, National Astronomical Observatory of Japan, and University of Tokyo in collaboration with South African Astronomical Observatory under a financial support of Grant-in-Aid for Scientific Research on Priority Area (A) No. 10147207 and No. 10147214, and Grant-in-Aid No. 13573001 of the Ministry of Education, Culture, Sports, Science, and Technology of Japan.

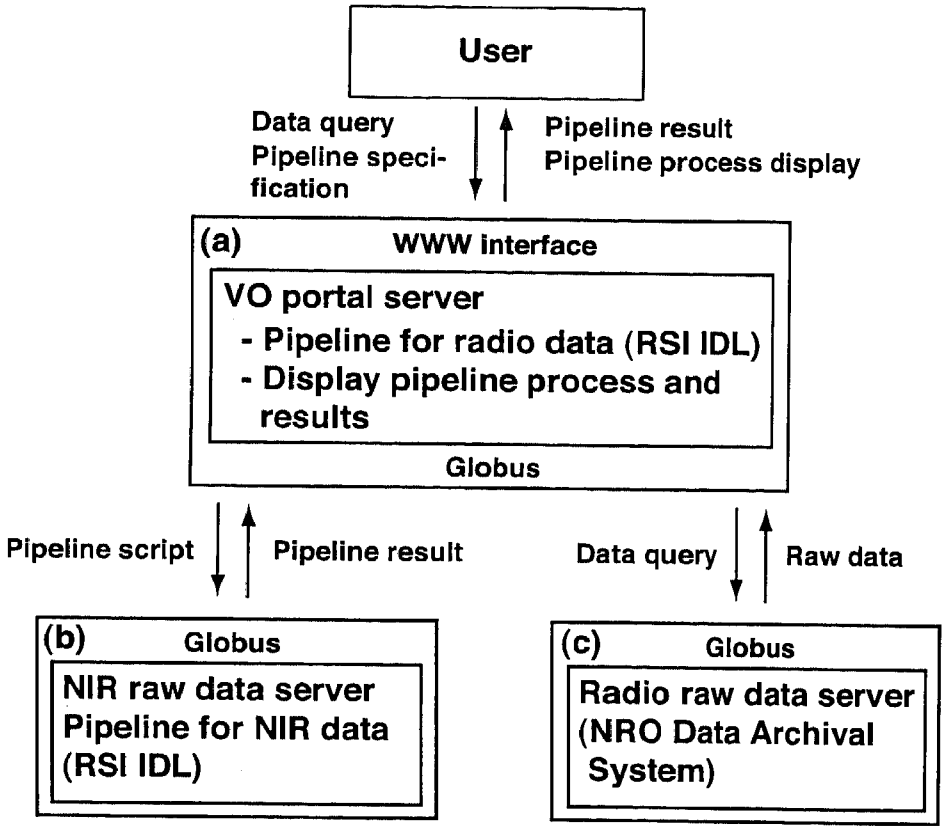

Figure A.1 A shcmatic illustration of the VO prototype system in ALMA-Japan

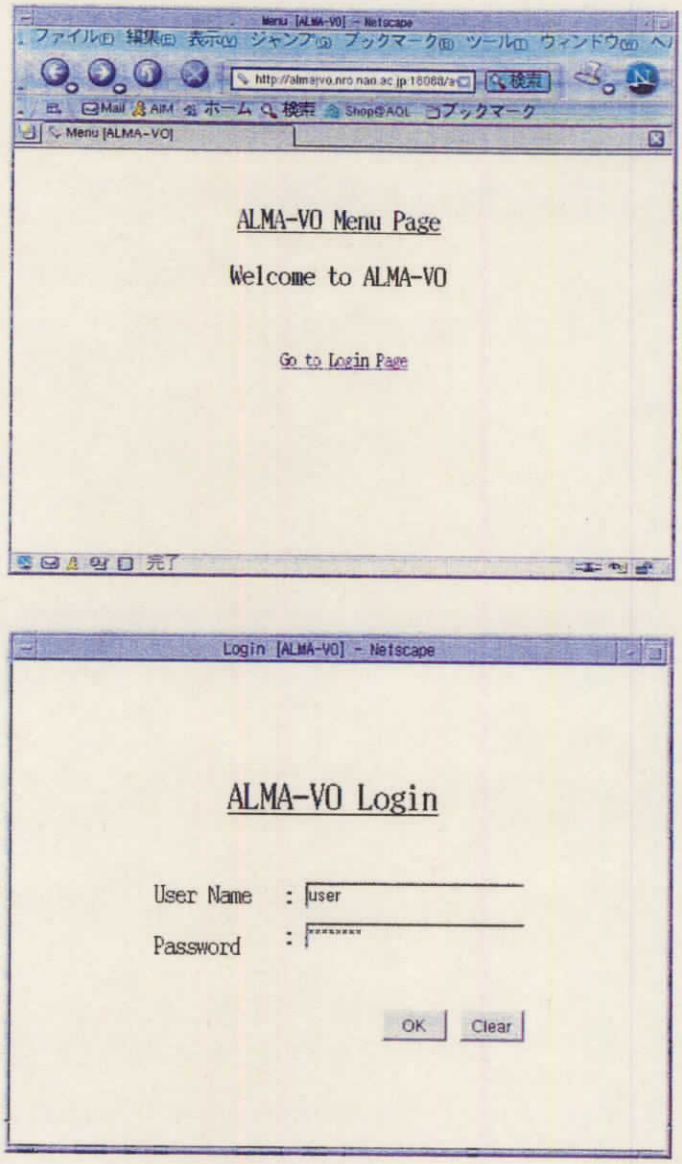

Figure A.2 Screen shots of the VO main page (top) and login page (bottom).

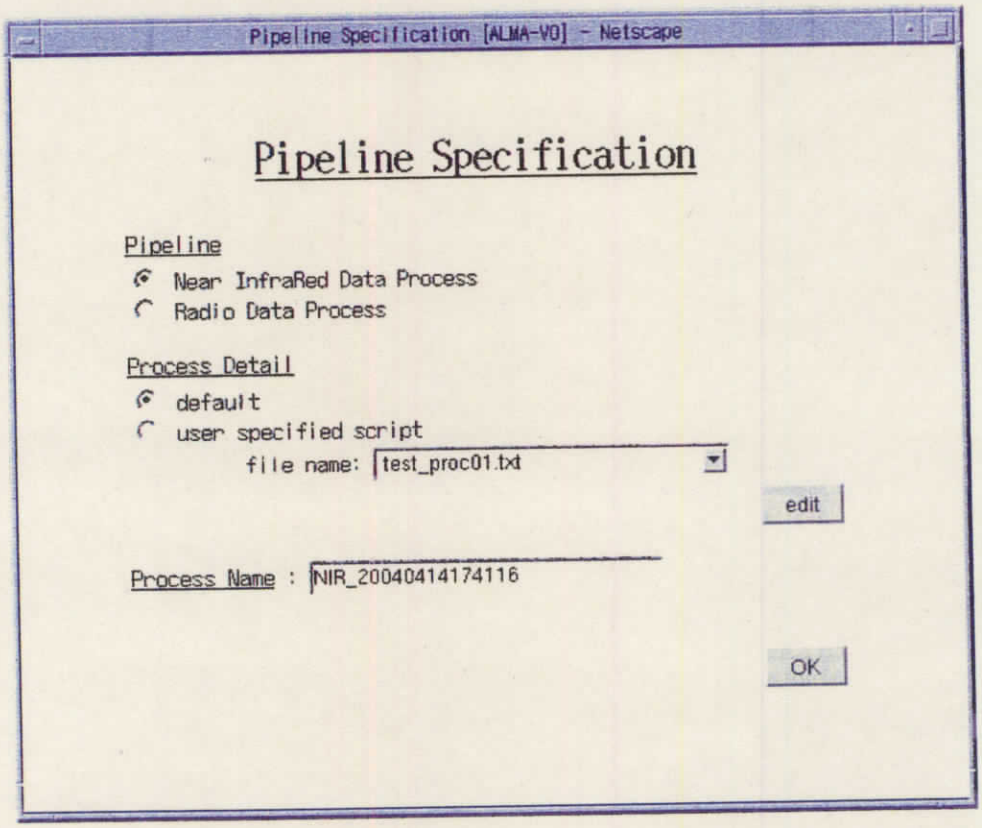

Figure A.3 A screen shot of the pipeline specification (near-infrared or radio) page.

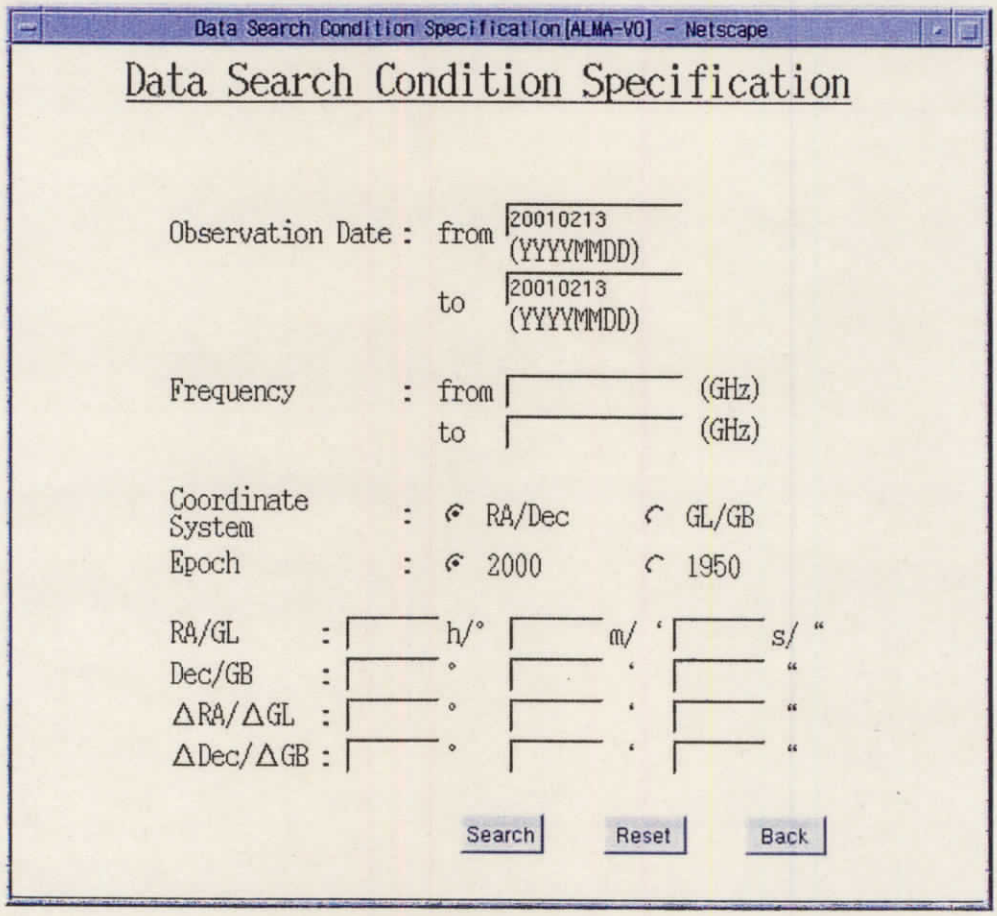

Figure A.4 Data search page for the radio data pipeline.

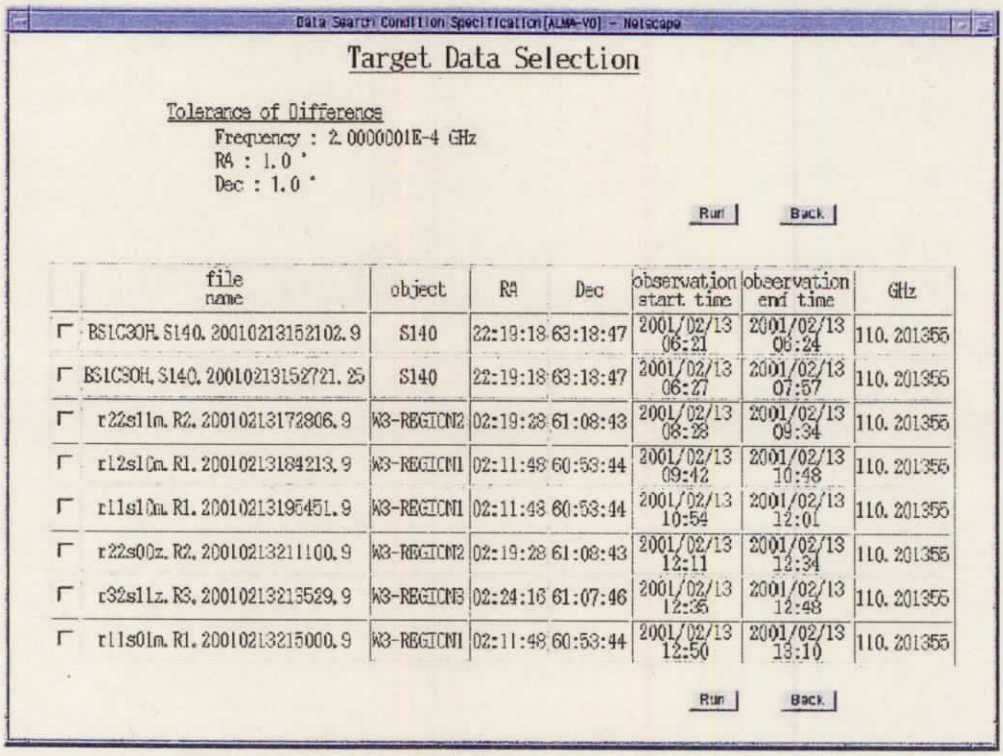

Figure A.5 An example of the result of radio data search.

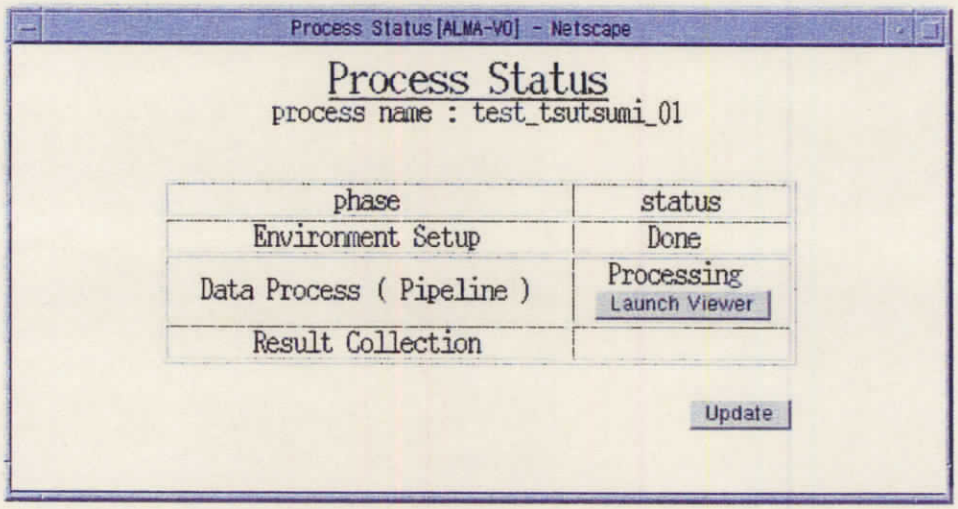

Figure A.6 A screen shot of the window showing the status of pipeline process.

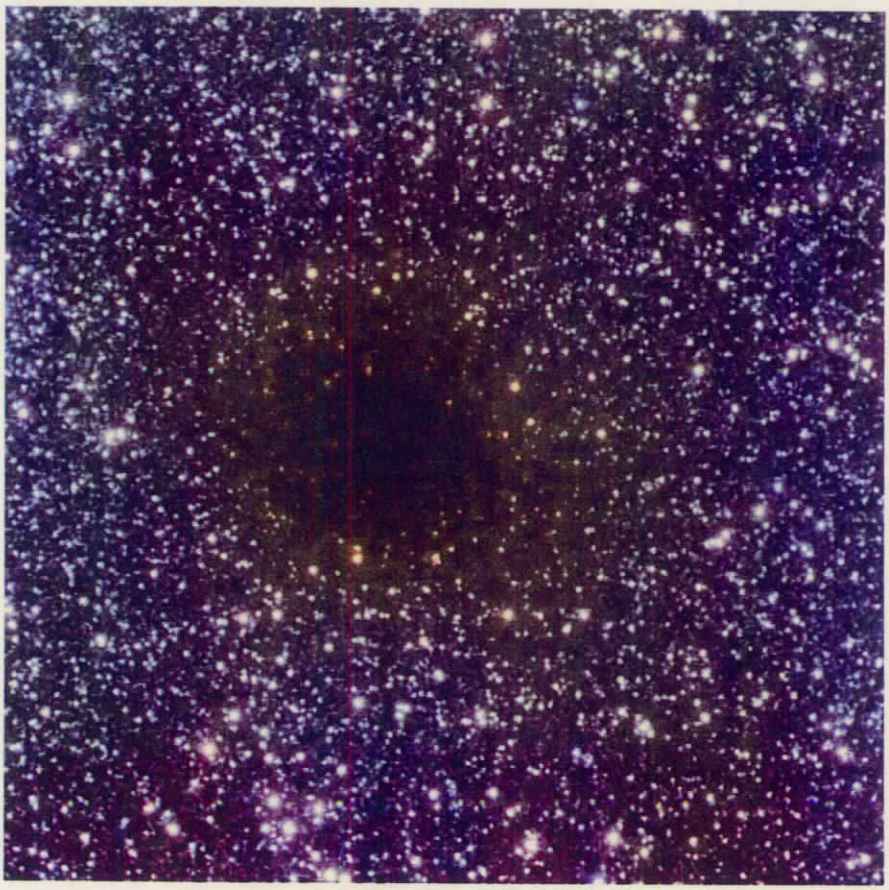

Figure A.7 An example of pipeline processed near-infrared image (J, H, and K_s three-color composite) of the globule FeSt 1-457.

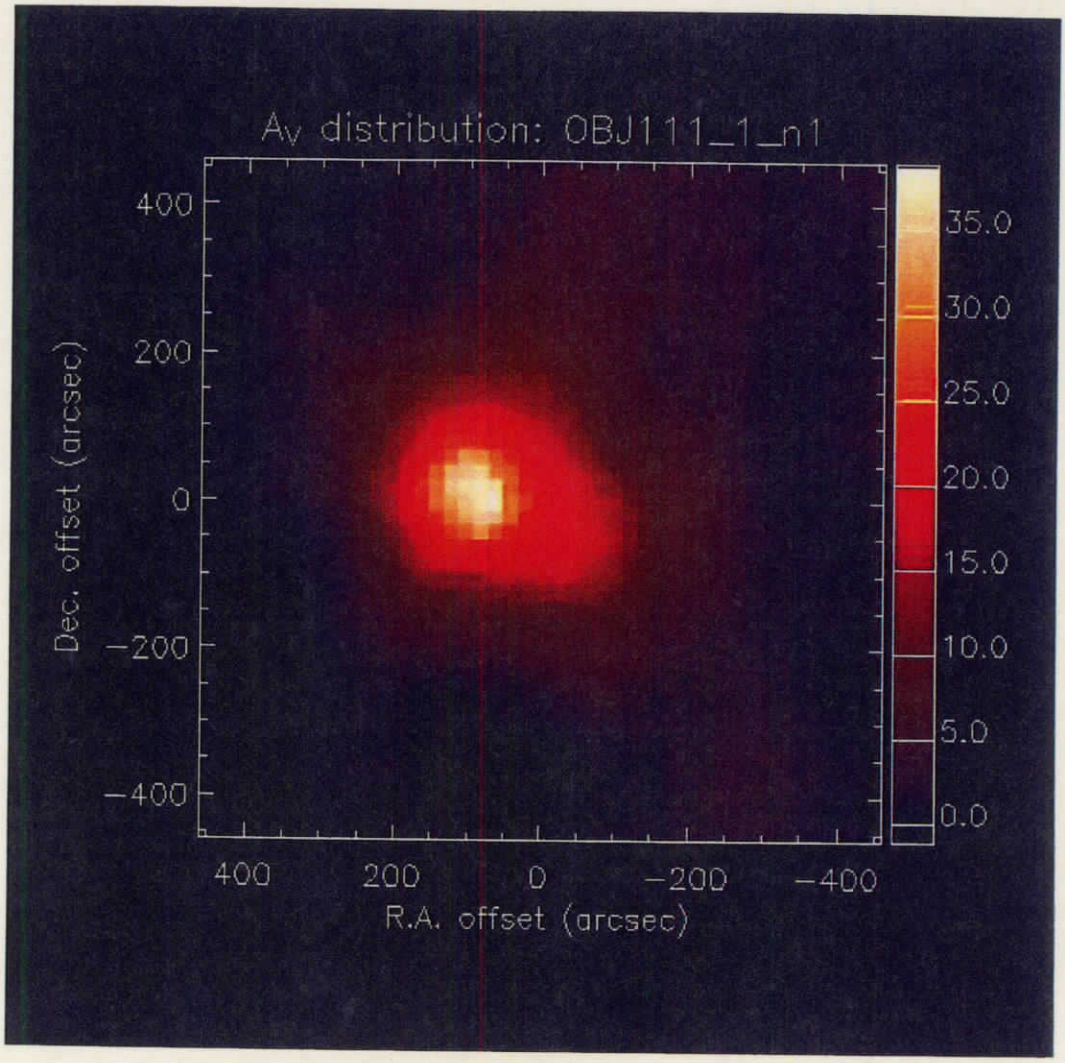

Figure A.8 An example of extinction (A_V) measurements of the globule FeSt 1-457 using the near-infrared pipeline.

Bibliography

[1] Adams, F. C., Lada, C. J., & Lizano, S., 1987, ApJ, 312, 788

[2] Aikawa, Y., Herbst, E., Roberts, H., & Caselli, P., 2004, ApJ, In press

[3] Aikawa, Y., Ohashi, N., Inutsuka, S., Herbst, E., & Takakuwa, S., 2001, ApJ, 552, 639

[4] Alves, J. F., Lada, C. J., & Lada E. A., 2001, Nature, 409, 159

[5] André, P. & Montmerle, T., 1994, ApJ, 420, 837

[6] André, P., Ward-Thompson, D., & Barsony, M., 1993, ApJ, 406, 122

[7] André, P., Ward-Thompson, D., & Motte, F., 1996, A&A, 314, 625

[8] Arce, H. G. & Goodman, A. A., 1999, ApJ, 517, 264

[9] Bachiller, R., 1996, ARA&A, 34, 111

[10] Bacmann, A., André, P., Puget, J. -L., Abergel, A., Bontemps, S., & Ward-Thompson, D., 2000, A&A, 361, 555

[11] Barnard, E. E., 1919, ApJ, 49, 1

[12] Barnard, E. E., 1927, Catalogue of 349 Dark Objects in the Sky (Chicago: Univ. Chicago Press)

[13] Beichman, C. A., Myers, P. C., Emerson, J. P., Harris, S., Mathieu, R., Benson, P. J., & Jennings, R. E., 1986, ApJ, 307, 337

[14] Belloche, A., André, P., Despois, D., & Blinder, S., 2002, A&A, 393, 927

[15] Benson, P. J. & Myers, P. C., 1989, ApJS, 71, 89

[16] Bergin, E. A., Alves, J., Huard, T., & Lada, C. J., 2002, ApJL, 570, L101

[17] Bernard, J. P., Abergel, A., Ristorcelli, I., Pajot, F., Torre, J. P., Boulanger, F., Giard, M., Lagache, G., Serra, G., Lamarre, J. M., Puget, J. L., Lepeintre, F., & Cambrésy, L. 1999, A&A, 347, 640

[18] Bevington, P. R., & Robinson, D. K., 1992, Data Reduction and Error Analysis for the Physical Sciences (McGraw-Hill, New York)

[19] Blitz L., 1980, in Giant Molecular Clouds in the Galaxy, ed. P. M. Solomon & M. G. Edmunds, Pergammon, Oxford, 1

[20] Bohlin, R. C., Savage, B. D., & Drake, J. F., 1978, ApJ, 224, 132

[21] Bok, B. J., 1956, AJ, 61, 309

[22] Bok, B. J. & Reilly, E. F., 1947, ApJ, 105, 255

[23] Bonnor, W. B., 1956, MNRAS, 116, 351

[24] Cambrésy, L., 1998, in The Impact of Near Infrared Sky Surveys on Galactic and Extragalactic Astronomy, ed. N. Epchtein (Dordrecht: Kluwer), 157

[25] Cambrésy, L. 1999, A&A, 345, 965

[26] Cardelli, J. A., Clayton, G. C., & Mathis, J. S. 1989, ApJ, 345, 245

[27] Caselli, P., Myers, P. C., & Thaddeus, P., 1995, ApJL, 455, 77

[28] Caselli, P., Benson, P. J., Myers, P. C., & Tafalla, M., 2002, ApJ, 572, 238

[29] Caselli, P., Walmsley, C. M., Tafalla, M., Dore, L., & Myers, P. C., 1999, ApJ, 523, 165

[30] Cernicharo, J., 1991, in The Physics of Star Formation and Early Stellar Evolution, ed. C. J. Lada & N. D. Kylafis (Kluwer, Dordrecht), 287

[31] Clemens, D. P. & Barvainis, R., 1988, ApJS, 68, 257

[32] Cousins, A. W. J. 1976, MNRAS, 81, 25

[33] Curry, C. L., 2000, ApJ, 541, 831

[34] Curry, C. L., 2002, ApJ, 576, 849

[35] Cutri, R. M., Skrutskie, M. F., van Dyk, S., Beichman, C. A., Carpenter, J. M., Chester, T., Cambrésy, L., Evans, T., Fowler, J., Gizis, J., Howard, E., Huchra, J., Jarrett, T., Kopan, E. L., Kirkpatrick, J. D., Light, R. M., Marsh, K. A., McCallon, H., Schneider, S., Stiening, R., Sykes, M., Weinberg, M., Wheaton, W. A., Wheelock, S., & Zacarias, N., 2003, CDS/ADC Collection of Electronic Catalogues, 2246

[36] Dame, T. M., Ungerechts, H., Cohen, R. S., De Geus, E. J., Grenier I. A., May, J., Murphy, D. C., Nyman, L. -Å, & Thaddeus, P., 1987, ApJ, 322, 706

[37] Di Francesco, J., Hogerheijde, M. R., Welch, W. J., & Bergin, E. A., 2002, AJ, 124, 2749

[38] Dickman, R. L. 1978, AJ, 83, 363

[39] Dobashi, K., Uehara, H., Kandori, R., Umemoto, T. & Sato, F., PASJ, In press

[40] Dutra, C. M. & Bica, E., 2002, A&A, 383, 631

[41] Ebert, R., 1955, Zs. Ap., 37, 217

[42] Evans, N. J., II, 1999, ARA&A, 37, 311

[43] Evans, N. J., II, Rawlings, J. M. C., Shirley, Y. L., & Mundy, L. G., 2001, ApJ, 557, 193

[44] Falgarone, E., Puget, J. -L., & Perault, M., 1992, A&A, 257, 715

[45] Feitzinger, J. V. & Stuewe, J. A., 1984, A&AS, 58, 365

[46] Foster, P. N. & Chevalier, R. A., 1993, ApJ, 416, 303

[47] Fuller, G. A. & Myers, P. C., 1992, ApJ, 384, 523

[48] Galli, D., Walmsley, M., & Gonçalves, J., 2002, A&A, 394, 275

[49] Goodman, A. A., Benson, P. J., Fuller, G. A., & Myers, P. C., 1993, 406, 528

[50] Gorenstein, P., 1975, ApJ, 198, 95

[51] Harvey, D. W. A., Wilner, D. J., Lada, C. J., Myers, P. C., Alves, J. F., & Chen, H., 2001, ApJ, 563, 903

[52] Harvey, D. W. A., Wilner, D. J., Lada, C. J., Myers, P. C., & Alves, J. F., 2003, ApJ, 598, 1112

[53] Hennebelle, P., Whitworth, A. P., Gladwin, P. P., & André, P., 2003, MNRAS, 340, 870

[54] Hennebelle, P., Whitworth, A. P., Cha, S. -H., & Goodwin, S. P., 2004, 348, 687

[55] Hong, S. S. & Greenberg, J. M. 1978, A&A, 70, 695

[56] Hotzel, S., Harju, J., & Juvela, M., 2002a, A&A, 395, 5

[57] Hotzel, S., Harju, J., Juvela, M., Mattila, K., & Haikala, L. K., 2002b, A&A, 391, 275

[58] Hotzel, S., Harju, J., Lemke, D., Mattila, K., & Walmsley, C. M., 2001, A&A, 372, 302

[59] Huard, T. L., Sandell, G., & Weintraub, D. A., 1999, ApJ, 526, 833

[60] Jijina, J., Myers, P. C., & Adams, F. C., 1999, ApJS, 125, 161

[61] Johnson, H. L., & Morgan, W. W. 1953, ApJ, 117, 313

[62] Johnstone, D., Wilson, C. D., Moriarty-Schieven, G., Joncas, G., Smith, G., Gregersen, E., & Fich, M., 2000, ApJ, 545, 327

[63] Johnstone, D., Fich, M., Mitchell, G. F., & Moriarty-Schieven, G., 2001, ApJ, 559, 307

[64] Jones, C. E., Basu, S., & Dubinski, J., 2001, ApJ, 551, 387

[65] Kandori, R., Dobashi, K., Uehara, H., Sato, F., & Yanagisawa, K., 2003, AJ, 126, 1888

[66] Kandori, R., Nakajima, Y., Tamura, M., Tatematsu, K., Aikawa, Y., Naoi, T., Sugitani, K., Nakaya, H., Nagayama, T., Nagata, T., Kurita, M., Kato, D., Nagashima, C., and Sato, S., AJ, Submitted

[67] Kenyon, S. J., & Hartmann, L. 1995, ApJS, 101, 117

[68] Kenyon, S. & Starrfield, S., 1979, PASP, 91, 271

[69] Kim, S. H., Martin, P. G., & Hendry, P. D. 1994, ApJ, 422, 164

[70] Kun, M. & Prusti, T. 1993, A&A, 272, 235

[71] Lada, C. J., 1991, in The Physics of Star Formation and Early Stellar Evolution, ed. C. J. Lada & N. D. Kylafis (Dordrecht: Kluwer Academic Publishers), 329

[72] Lada, C. J., Alves, J., & Lada, E. A., 1999, ApJ, 512, 250

[73] Lada, C. J., Huard, T. L., Crews, L. J., & Alves, J. F., 2004, ApJ, 610, 303

[74] Lada, C. J., Lada, E. A., Clemens, D. P., & Bally, J. 1994, ApJ, 429, 694

[75] Lada C. J. & Wilking, B. A., 1984, ApJ, 287, 610

[76] Lada, E. A., 1999, in The Origin of Stars and Planetary Systems, ed. C. J. Lada & N. D. Kylafis (Kluwer, NATO Sci. Ser. 540), 441

[77] Lai, S., Velusamy, T., Langer, W. D., & Kuiper, T. B. H., 2003, AJ, 126, 311

[78] Landolt, A. U. 1992, AJ, 104,340

[79] Larson, K. A., Wolff, M. J., Roberge, W. G., Whittet, D. C. B., & He, L. 2000, ApJ, 532, 1021

[80] Larson, R. B., 1969, MNRAS, 145, 271

[81] Larson, R. B., 1981, MNRAS, 194, 809

[82] Larson, R. B., 2003, Reports on Progress in Physics, 66, 1651

[83] Launhardt, R., 1996, Ph.D. Thesis,

[84] Launhardt, R. & Henning, T., 1997, A&A, 326, 329

[85] Launhardt, R., Evans, N. J., II, Wang, Y., Clemens, D. P., Henning, T., & Yun, J. L., 1998, 119, 59

[86] Lee, C. W. & Myers, P. C., 1999, APJS, 123, 233

[87] Lee, C. W., Myers, P. C., & Plume, R., 2004, ApJS, 153, 523

[88] Lee, C. W., Myers, P. C., & Tafalla, M., 1999, ApJ, 526, 788

[89] Lee, C. W., Myers, P. C., & Tafalla, M., 2001, ApJS, 136, 703

[90] Leung, C. M., Kutner, M. L., & Mead, K. N., 1982, ApJ, 262, 583

[91] Lombardi, M. & Bertin, G., 2001, A&A, 375, 1091

[92] Lynds, B. T., 1962, ApJS, 7, 1

[93] Mac Low M. & Klessen, R. S., 2004, Rev. Mod. Phys., 76, 125

[94] Mathis, J. S. 1990, ARA&A, 28, 37

[95] Mathis, J. S., Rumpl, W., & Nordsieck, K. H. 1977, ApJ, 217, 425

[96] McKee, C. F., 1999, in The Origin of Stars and Planetary Systems, ed. C. J. Lada & N. D. Kylafis (Kluwer, NATO Sci. Ser. 540), 29

[97] McKee, C. F., & Holliman, J. H., II., 1999, ApJ, 522, 313

[98] McLaughlin, D. E. & Pudritz, R. E., 1997, ApJ, 476, 750

[99] Motoyama, K., & Yoshida, T., 2003, MNRAS, 344, 461

[100] Myers, P. C., 1983, ApJ, 266, 309

[101] Myers, P. C., Fuller, G. A., Goodman, A. A., & Benson, P. J., 1991, ApJ, 376, 561

[102] Nagashima, C., Nagayama, T., Nakajima, Y., Tamura, M., Sugitani, K., Nagata, T., Hirao, T., Nakaya, H., Yanagisawa, K., & Sato, S., 1999, in Proc. Star Formation 1999, ed. T. Nakamoto & Nobeyama Radio Observatory, 397

[103] Nakajima, Y., Nagata, T., Sato, S., Nagayama, T., Nagashima, C., Kato, D., Kurita, M., Kawai, T., Tamura, M., Nakaya, H., & Sugitani, K., 2003, AJ, 125, 1407

[104] Nakano, T., 1998, ApJ, 494, 587

[105] Nagayama, T., Nagashima, C., Nakajima, Y., Nagata, T., Sato, S., Nakaya, H., Yamamuro, T., Sugitani, K., & Tamura, M., 2003, Proc. SPIE, 4841, 459

[106] Ogino, S., Tomisaka, K., & Nakamura, F., 1999, PASJ, 51, 637

[107] Onishi, T., Mizuno, A., Kawamura, A., Tachihara, K., & Fukui, Y., 2002, ApJ, 575, 950

[108] Ossenkopf, V. & Henning, T. 1994, A&A, 291, 943

[109] Penston, M. V., 1969, MNRAS, 144, 425

[110] Persson, S. E., Murphy, D. C., Krzeminski, W., Roth, M., & Rieke, M. J., 1998, AJ, 116, 2475

[111] Plummer, H. C., 1911, MNRAS, 71, 460

[112] Predehl, P. & Schmitt, J. H. M. M., 1995, A&A, 293, 889

[113] Pudritz, R. E., 2002, Science, 295, 68

[114] Racca, G., Gómez, M., & Kenyon, S. J., 2002, AJ, 124, 2178

[115] Rieke, G. H. & Lebofsky, M. J., 1985, ApJ, 288, 618

[116] Ryter, C., Cesarsky, C. J., & Audouze, J., 1975, ApJ, 198, 103

[117] Ryter, C. E., 1996, Ap&SS, 236, 285

[118] Sato, F., & Fukui, Y. 1989, ApJ, 343, 773

[119] Sato, F., Mizuno, A., Nagahama, T., Onishi, T., Yonekura, Y., & Fukui, Y. 1994, ApJ, 435, 279

[120] Schlegel, D. J., Finkbeiner, D. P., & Davis, M. 1998, ApJ, 500, 525

[121] Schneider, S. & Elmegreen, B. G., 1979, ApJS, 41, 87

[122] Scoville, N. Z. & Solomon, P. M., 1975, ApJ, 199, 105

[123] Shirley, Y. L., Evans, N. J., II, Rawlings, J. M. C., 2002, ApJ, 575, 337

[124] Shu, F. H., 1977, ApJ, 214, 488

[125] Stepnik, B., Abergel, A., Bernard, J. P., Boulanger, F., Cambrésy, L., Giard, M., Jones, A. P., Lagache, G., Lamarre, J. M., Meny, C., Pajot, F., Le Peintre, F., Ristorcelli, I., Serra, G., & Torre, J. P. 2003, A&A, 398, 551

[126] Stetson, P. B. 1987, PASP, 99, 191

[127] Strafella, F., Campeggio, L., Aiello, S., Cecchi-Pestellini, C. & Pezzuto, S. 2001, ApJ, 558, 717

[128] Straizys, V., Cernis, K., & Bartasiute, S., 1996, Baltic Astronomy, 5, 125

[129] Sunada, K., Yamaguchi, C., Nakai, N., Sorai, K., Okumura, S., & Ukita, N., 2000, Proc. SPIE, 4015, 237

[130] Tafalla, M., Myers, P. C., Caselli, P., Walmsley, C. M., & Comito, C. 2002, ApJ, 569, 815

[131] Tatematsu, K., Umemoto, T., Kandori, R., & Sekimoto, Y., 2004, ApJ, 606, 333

[132] Tielens, A. G. G. M. 1989, in IAU Symp. 135, Interstellar Dust, ed. L. J. Allamandola & A. G. G. M. Tielens (Dordrecht: Kluwer), 239

[133] Tiné, S., Roueff, E., Falgarone, E., Gerin, M., & Pineau des Forêts, G., 2000, A&A, 356, 1039

[134] Tomita, Y., Saito, T., & Ohtani, H., 1979, PASJ, 31, 407

[135] van Dishoek, E. F., Blake, G. A., Draine, B. T., & Lunine, J. I., 1993, in Protostars and Planets III, ed. E. Levy & J. Lunine (Tucson: Univ. Arizona Press), 163

[136] Vrba, F. J., Coyne, G. V., & Tapia, S. 1993, AJ, 105, 1010

[137] Visser, A. E., Richer, J. S., & Chandler, C. J., 2001, MNRAS, 323, 257

[138] Visser, A. E., Richer, J. S., & Chandler, C. J., 2002, AJ, 124, 2756

[139] Vuong, M. H., Montmerle, T., Grosso, N., Feigelson, E. D., Verstraete, L., & Ozawa, H., 2003, A&A, 408, 581

[140] Walker, C. K., Lada, C. J., Young, E. T., Maloney, P. R., & Wilking, B, A., 1986, ApJ, 309, 47

[141] Ward-Thompson, D., 2002, Science, 295, 76

[142] Ward-Thompson, D., André, P., & Kirk, J. M., 2002, MNRAS, 329, 257

[143] Ward-Thompson, D., Motte, F., & André, P., 1999, MNRAS, 305, 143

[144] Ward-Thompson, D., Scott, P. F., Hills, R. E., & André, P., 1994, MNRAS, 268, 276

[145] Weinreb, S., Barrett ,A. H., Meeks, M. L., & Henry, J. C., 1963, Nature, 200, 829

[146] Whittet, D. C. B. 1992, in Dust in the Galactic Environment (NY: Inst. Phys.)

[147] Whittet, D. C. B., Gerakines, P. A., Hough, J. H., & Shenoy, S. S. 2001, ApJ, 547, 872

[148] Whitworth, A. P., & Ward-Thompson, D., 2001, ApJ, 547, 317

[149] Wilking, B. A., Lada, C. J., & Young, E. T., 1989, ApJ, 340, 823

[150] Williams, J. P., Blitz, L., & McKee, C. F., 2000, in Protostars and Planets IV, ed. V. Mannings, A. P. Boss, & S. S. Russel (Univ. Arizona Press), 97

[151] Wolf, M. 1923, Astron. Nachr., 219, 109

[152] Yun, J. L. & Clemens, D. P., 1992, ApJL, 385, 21

[153] Young, C. H. et al., 2004, ApJS, 154, 396

[154] Young, C. H., Shirley, Y. L., Evans, N. J., II, & Rawlings, J. M. C., 2003, ApJS, 145, 111

[155] Zhou, S., Evans, N. J., II, Koempe, C., & Walmsley, C. M., 1993, ApJ, 404, 232